2017

DISCONNECTED-SEA QUARKS CONTRIBUTION TO NUCLEON ELECTROMAGNETIC FORM FACTORS

Raza Sabbir Sufian
University of Kentucky, sabbir.sufian@uky.edu
Author ORCID Identifier:
https://orcid.org/0000-0002-3263-4767
Digital Object Identifier: https://doi.org/10.13023/ETD.2017.407

STUDENT AGREEMENT:

I represent that my thesis or dissertation and abstract are my original work. Proper attribution has been given to all outside sources. I understand that I am solely responsible for obtaining any needed copyright permissions. I have obtained needed written permission statement(s) from the owner(s) of each third-party copyrighted matter to be included in my work, allowing electronic distribution (if such use is not permitted by the fair use doctrine) which will be submitted to UKnowledge as Additional File.

I hereby grant to The University of Kentucky and its agents the irrevocable, non-exclusive, and royalty-free license to archive and make accessible my work in whole or in part in all forms of media, now or hereafter known. I agree that the document mentioned above may be made available immediately for worldwide access unless an embargo applies.

I retain all other ownership rights to the copyright of my work. I also retain the right to use in future works (such as articles or books) all or part of my work. I understand that I am free to register the copyright to my work.

REVIEW, APPROVAL AND ACCEPTANCE

The document mentioned above has been reviewed and accepted by the student's advisor, on behalf of the advisory committee, and by the Director of Graduate Studies (DGS), on behalf of the program; we verify that this is the final, approved version of the student's thesis including all changes required by the advisory committee. The undersigned agree to abide by the statements above.

<div align="right">

Raza Sabbir Sufian, Student

Dr. Keh-Fei Liu, Major Professor

Dr. Christopher Crawford, Director of Graduate Studies

</div>

DISCONNECTED-SEA QUARKS CONTRIBUTION TO NUCLEON
ELECTROMAGNETIC FORM FACTORS

DISSERTATION

A dissertation submitted in partial
fulfillment of the requirements for
the degree of Doctor of Philosophy
in the College of Arts and Sciences
at the University of Kentucky

By
Raza Sabbir Sufian
Lexington, Kentucky

Director: Dr. Keh-Fei Liu, Professor of Physics
Lexington, Kentucky 2017

ABSTRACT OF DISSERTATION

DISCONNECTED-SEA QUARKS CONTRIBUTION TO NUCLEON ELECTROMAGNETIC FORM FACTORS

We present comprehensive analysis of the light and strange disconnected-sea quarks contribution to the nucleon electric and magnetic form factors. The lattice QCD estimates of strange quark magnetic moment $G_M^s(0) = -0.064(14)(09)\,\mu_N$ and the mean squared charge radius $\langle r_s^2 \rangle_E = -0.0043(16)(14)\,\mathrm{fm}^2$ are more precise than any existing experimental measurements and other lattice calculations. The lattice QCD calculation includes ensembles across several lattice volumes and lattice spacings with one of the ensembles at the physical pion mass. We have performed a simultaneous chiral, infinite volume, and continuum extrapolation in a global fit to calculate results in the continuum limit. We find that the combined light-sea and strange quarks contribution to the nucleon magnetic moment is $-0.022(11)(09)\,\mu_N$ and to the nucleon mean square charge radius is $-0.019(05)(05)\,\mathrm{fm}^2$. The most important outcome of this lattice QCD calculation is that while the combined light-sea and strange quarks contribution to the nucleon magnetic moment is small at about 1%, a negative $2.5(9)\%$ contribution to the proton charge radius and a relatively larger positive $16.3(6.1)\%$ contribution to the neutron charge radius come from the sea quarks in the nucleon. For the first time, by performing global fits, we also give predictions of the light-sea and strange quarks contributions to the nucleon electric and magnetic form factors at the physical point and in the continuum and infinite volume limits in the momentum transfer range of $0 \leq Q^2 \leq 0.5\,\mathrm{GeV}^2$.

KEYWORDS: Lattice QCD, Electromagnetic Form Factors, Quarks, Gluons.

Author's signature: Raza Sabbir Sufian

Date: September 28, 2017

DISCONNECTED-SEA QUARKS CONTRIBUTION TO NUCLEON
ELECTROMAGNETIC FORM FACTORS

By
Raza Sabbir Sufian

Director of Dissertation: Keh-Fei Liu

Director of Graduate Studies: Christopher Crawford

Date: September 28, 2017

To
my mother, my father and Chaity
for their constant support and unconditional love.

ACKNOWLEDGMENTS

LIST OF FIGURES

Chapter 1 Introduction

One of the main goals of the Standard Model of particle physics is to provide an explanation of nucleon properties, *i.e.* an explanation in terms quarks and gluons and their dynamics. Quantum chromodynamics (QCD) theory, in which quarks with color charge interact through gluon exchange with gluons interacting amongst themselves as well since they too carry color charge, is expected to give a correct description of the strong force. The theory of strong interaction (QCD) is a non-Abelian gauge theory. The quarks occurring in six different flavors carry electric and weak charge and also an additional charge called color charge. The strong force is mediated by massless gluons which carry color and anti-color charges and they can also interact with themselves resulting in the non-Abelian structure of QCD. There are two parameters in QCD, namely the fermion mass m_f and the bare coupling constant g_0. The running coupling constant, which results in asymptotic freedom, leads to QCD phenomenon which is different in the low and high energy regions. Before the discovery of lattice gauge theory, perturbative quantum field theory had been used in which the integration measure of fields in a path integral is expanded in powers of the coupling constant and the corresponding Feynman diagrams are then regularized order by order in the coupling constant. Although this perturbative approach leads to impressive results for weakly interacting theories, for strongly coupled theories such as QCD at low energies, this perturbative approach of field theory breaks down and is not applicable.

Lattice QCD, a first-principles approach, is believed to be the correct theory to describe nucleon properties in the nonperturbative region when systematic uncertainties are included in the calculation. Using lattice QCD, one can calculate hadronic properties where perturbative QCD fails. Lattice QCD is a local gauge theory and it satisfies local gauge symmetries. Although spacetime symmetry is broken on the

lattice, this symmetry is expected to be automatically restored in the continuum limit. In the classical level QCD Lagrangian, QCD does not have any dimensionful scale parameter in the massless quark limit. But when the theory is quantized, a scale, called Λ_{QCD} emerges through the dimensional transmutation process. Therefore, with massless quarks, a non-zero nucleon mass emerges due to the confinement process and color-neutral hadrons can be produced. This is purely a nonperturbative phenomenon and cannot be realized using perturbation theory. Lattice QCD emerges as the best tool to study the nonperturbative phenomena in QCD. This is the only reliable first-principles nonperturbative technique to study QCD. The fundamental reason why lattice QCD is believed and has been tested as a reliable theory is because in the numerical simulations, uncertainties related to systematics such as finite lattice spacing, finite volume effects, etc. can be measured and thus artifacts can be removed from the final results.

The consistent way of describing QCD on the lattice is the following:

1. discretization of spacetime (Euclidean) by a hypercubic lattice with cutoff, Λ called lattice regularization,

2. discretization of continuum QCD action,

3. quantization of QCD using path integral formalism,

4. application of Monte-Carlo simulation to calculate expectation values of different operators.

As the first step of lattice QCD calculation, one first converts QCD theory to Euclidean spacetime using Wick rotation by replacing $g_{\mu\nu}$ with Euclidean metric $\delta_{\mu\nu}$. This Euclidean metric is obtained by performing the Wick rotation to imaginary time $t \to -i\tau$. This operation removes the distinction between covariant and contravariant vectors on the lattice. The Euclidean spacetime is discretized by introducing a four-dimensional grid points on the hypercubic lattice which are separated by the lattice

spacing a,

$$\Lambda = \left\{ n \in \mathbb{R}^4 \,|\, \frac{n_0}{a} = 0, \, ..., \, N_T; \, \frac{n_i}{a} = 0, \, ..., \, N_L \right\} \tag{1.1}$$

Then the size extent of the hypercubic box is determined by the finite extent in the time and space direction

$$T = aN_T$$

and

$$L = aN_L \tag{1.2}$$

One then obtains the dual lattice which leads to a discrete set of momenta by performing a discrete Fourier transform

$$\Lambda^* = \left\{ p \in \mathbb{R}^4 \,|\, p_0 = \frac{2\pi n_0}{T}; \, p_i = \frac{2\pi n_i}{T} \right\} \tag{1.3}$$

The gauge fields $A_\mu(z)$ are written in terms of parallel transporters called link variables, each of which connects two spacetime points x and y as

$$U(x, y) = \mathcal{P} \, \exp\left(-\int_y^x dz A_\mu(z) \right) \tag{1.4}$$

The $SU(3)$ link variable connecting two neighboring lattice sites n and $n + \hat{\mu}$ along a straight line is written as

$$\begin{aligned} U_\mu(n) &\equiv U(n, n + \hat{\mu}) \\ &= \exp\left(ia A_\mu(n) \right) \end{aligned} \tag{1.5}$$

As a part of discretization of the QCD action, the gauge or gluonic part of the QCD action is constructed from the gauge links

$$P_{\mu\nu}(n) = U_\mu(n) U_\nu(n + \hat{\mu}) U_\mu^\dagger(n + \hat{\mu}) U_\nu^\dagger(n) \tag{1.6}$$

to obtain the smallest gauge-invariant closed loop $P_{\mu\nu}(n)$, called a plaquette. The
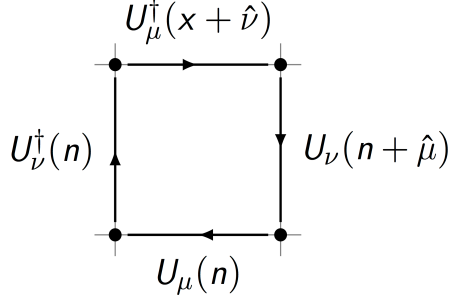
Figure 1.1: Gauge-invariant plaquette

fermionic part of the QCD action is discretized by replacing the covariant derivative

$$D_\mu \psi(n) \to \frac{1}{2a}\left(\gamma_\mu U_\mu(n)\psi(n+\hat{\mu}) - \gamma_\mu U_\mu^\dagger(n-\hat{\mu})\psi(n-\hat{\mu})\right) \tag{1.7}$$

where the quark fields are covariant under $SU(3)$ color gauge transformation. The quantization of the lattice formulation is then performed by using a Euclidean path integral. The expectation value of an operator is obtained by integrating over all possible field configurations and is expressed by

$$\langle\mathcal{O}\rangle = \frac{1}{Z}\int \mathcal{D}U\,\mathcal{D}\psi\,\mathcal{D}\bar{\psi}\mathcal{O}(\bar{\psi},\psi,U)\exp\left(-S_G[U] - S_F[\bar{\psi},\psi,U]\right) \tag{1.8}$$

where S_G and S_F are discretized gluonic and fermionic parts of the QCD action, respectively and Z is the partition function. The anti-commuting fermion fields ψ, $\bar{\psi}$ are described by Grassmann variables and can be integrated out since the action is bilinear in ψ and $\bar{\psi}$:

$$\langle\mathcal{O}\rangle = \frac{1}{Z}\int \mathcal{D}U \prod_f (\det(D[U]))^{N_f}\mathcal{O}(S_F,U)\exp(-S_G[U])) \tag{1.9}$$

where $S_F(x,y) = D^{-1}(x,y)$ is a quark propagator which describes how the particles associated with ψ and $\bar{\psi}$ propagate through the QCD vacuum. $\det(D[U])$ is real and describes the roles of quark loops in the vacuum. From Eq. (1.9), it is seen that a physical observable $\langle\mathcal{O}\rangle$ can be evaluated by the integration over a set of gauge configurations $\{U\}$ with the weight factor of $\det(D[U])e^{-S_G}$. The gluonic

integration is then performed over the $SU(3)$ group using the Haar measure. When the gauge configurations are generated with the probability $\det(D[U])e^{-S_G}$, one can stochastically approximate the physical quantity as

$$\langle \mathcal{O} \rangle \approx \frac{1}{N_{\text{configs}}} \sum_i^{N_{\text{configs}}} \mathcal{O}(U_i) \tag{1.10}$$

where N_{configs} is the number of gauge configurations used in the numerical simulation.

The lattice discretization provides a regularization of the theory. The lattice spacing is taken to $a \to 0$ to obtain the result in the continuum limit. In this limit, the correlation length in the lattice unit diverges, $i.e.$ the continuum limit is a second order phase transition and there is no phase transition during the taking of the continuum limit. Because of asymptotic freedom, the limit of the QCD coupling $g \to 0$ corresponds to the $a \to 0$ limit.

Chapter 2 Nucleon Electromagnetic Form Factors

The space-like electromagnetic form factors of the proton and neutron obtained in electron-nucleon elastic scattering are key measures of the fundamental structure of hadrons. The quest for a detailed quantitative understanding of the nucleon form factors is an active field in hadronic physics. A wide variety of models has been proposed to describe the nucleon form factors. However, in most of these approaches, there has been no attempt to understand the observed hadron spectroscopy. Furthermore, a consensus among different phenomenological models and parameterizations which describe the nucleon form factors has not yet been achieved, especially for the neutron Dirac and Pauli electromagnetic form factors, nor the nucleon time-like form factors. The momentum transfer to the nucleon can be selected to probe different scales of the nucleon, from integral properties such as the charge radius to scaling properties of its internal constituents. At large internal distances or at small momenta, these form factors probe the size of the nucleon, while at short internal distances or at large momenta, they describe quark and gluon structures. It is convenient to define a frame, called the Breit frame, in which there is no energy transferred to the proton, the nucleon form factors can be written as Fourier transforms of their charge and magnetization distributions. But when the momentum transfer in an electron-nucleon scattering is much larger than the nucleon mass, *i.e.* $Q \gg M_N$, the form factors are not solely determined by the internal structure of the nucleon and contain dynamical effects due to relativistic boosts. In this situation, the physical interpretation of the form factors becomes complicated and cannot be simply thought of as the electric and magnetic charge distributions of the nucleon.

Nucleon electromagnetic form factors are studied through the exchange of virtual photon in elastic electron-nucleon scattering. Detailed reviews of the experimental

results and models can be found in Refs. [1,2]. It should be noted that inconsistencies in the extraction of the data appear in the proton electric to magnetic Sachs form factor (FF) ratio $R_p(Q^2) = \mu_p G_E^p(Q^2)/G_M^p(Q^2)$, when one compares double polarization experiments [3–6], in which the ratio R_p decreases almost linearly for momentum transfer $Q^2 > 0.5\,\text{GeV}^2$, with the results obtained from the Rosenbluth separation method [7–18] in which R_p remains constant in the space-like (SL) region. Predictions for different combinations of the neutron FFs are even more puzzling to explain using phenomenological models. A further limitation is that experimental data for the neutron FFs are not available in the large $Q^2 = -q^2$ regime. Another challenge is to describe the modulus of the electric to magnetic Sachs FF ratio $|G_E^p/G_M^p|$ measured by the PS170 experiment at LEAR [19] and by the BABAR Collaboration in the time-like (TL) domain [20] above the physical threshold $q_{\text{phys}}^2 = 4\,m_p^2$, where m_p is the proton mass, at which proton-antiproton pairs are produced at rest in their center of mass system, and where strong threshold effects are also important.

The most recent surprising discrepancy of the proton charge radius measured from the Lamb shift in muonic hydrogen [21,22] differs by more than 5σ from the radius extracted with 1% precision using the electron-proton scattering measurements and hydrogen spectroscopy. While the current Committee on Data for Science and Technology (CODATA) value of proton charge radius is $r_E^p = 0.8751(61)$ fm [23], the most recent muonic hydrogen Lamb shift experiment measures $r_E^p = 0.84087(39)$ fm [24] which is 4% smaller or differs by 7σ than the CODATA value. Other than the possibility that one of the proton charge radius extractions is wrong or involves considerable systematic uncertainties, the consequence of the "proton charge radius puzzle" can have serious consequences such as a new physics signature, anomalous QCD corrections, a 5σ adjustment of the Rydberg constant (in the absence of new physics explanations) which is measured with an accuracy of about 5 parts per trillion, and/or revision of sources of systematic uncertainties in the measurements of

neutrino-nucleus scattering observables. Recent results and reviews of the proton charge radius puzzle can be found in the Refs. [25–27].

The main goal of this dissertation is to calculate the disconnected-sea quarks contribution to the nucleon electromagnetic form factors. The light disconnected-sea quarks contribution to the nucleon electromagnetic form factors either has been ignored in previous lattice QCD calculations, or performed at heavier quark masses, or the uncertainties are too large compared to the signal. Experimentally, one cannot disentangle the light disconnected-sea quarks contribution from the valence quark contribution to the nucleon electromagnetic form factors. Therefore, the calculation [28] presented in this dissertation gives the first and most precise estimate of the light-disconnected-sea quarks contribution to the nucleon electromagnetic form factors at the physical point and in the continuum limit with controlled systematics. Similarly, we also calculate the strange quark contribution to the nucleon electromagnetic form factors and obtain the most precise estimates of the strange quark magnetic moment and charge radius [29] compared to any existing experimental results and lattice QCD calculations.

Chapter 3 Lattice Formalism: Two-Point Nucleon Correlation Function

3.1   Nucleon Two Point Correlation Function

The majority of the visible matter in the universe is made of nucleon, so the nucleon is the most interesting baryon amongst plenty of baryons. There are two nucleons: the proton and the neutron. The valence quark contents, quantum numbers, and masses on proton and nucleon are listed in the following table: On the lattice we calculate

Table 3.1: Nucleon quantum numbers and their physical masses.

Baryon	Quarks	$I(J^P)$	Mass (MeV)
Proton	uud	$\frac{1}{2}(\frac{1}{2}^+)$	938.272081(6) MeV
Neutron	udd	$\frac{1}{2}(\frac{1}{2}^+)$	939.565413(6) MeV

with mass degenerate up u quark and down d so that the nucleons also become mass degenerate. There are a number of nucleon operators listed in the Appendix 8.1 that have some overlap with the full nucleon. In the following lattice QCD calculation we have used the following annihilation and creation nucleon interpolation fields in Eqs. (8.16) and (8.17), respectively.

The nucleon two-point correlation function is defined as:

$$G_{\alpha\beta}(t, \vec{p}, \vec{x}_0) = \sum_{x} e^{-i\vec{p}.(\vec{x}-\vec{x}_0)} \langle 0|T\left(\chi_\alpha(x)\bar{\chi}_\beta(x_0)\right)|0\rangle \tag{3.1}$$

where t is the sink time, $\vec{p}$ is the momentum of the particle, $\chi(\bar{\chi})$ is the annihilation(creation) interpolation field, and α, β are Dirac indices. The interpolation fields with explicit color indices are written in the Appendix 8.1. Inserting a complete set of

normalized energy eigenstates of the QCD Hamiltonian and using the completeness property consistent with the normalization of Dirac spinors in Appendix 8.1,

$$\sum_{n,\vec{q},s} |n,\vec{q},s\rangle \langle n,\vec{q},s| = 1, \tag{3.2}$$

with t_0 and x_0 being the nucleon source temporal and spatial positions, respectively, we can rewrite Eq. (3.1) as

$$
\begin{aligned}
G_{\alpha\beta}(t,\vec{p}) &= \sum_x e^{-i\vec{p}\cdot(\vec{x}-\vec{x}_0)} \sum_{n,\vec{q},s} \langle 0|T\Big(\chi_\alpha(x)\,|n,\vec{q},s\rangle \langle n,\vec{q},s|\,\bar{\chi}_\beta(x_0)\Big)|0\rangle \\
&= \sum_x e^{-i\vec{p}\cdot(\vec{x}-\vec{x}_0)} \sum_{n,\vec{q},s} \langle 0|\,e^{H(t-t_0)-i\vec{q}\cdot(\vec{x}-\vec{x}_0)}\chi_\alpha(x_0)e^{-H(t-t_0)+i\vec{q}\cdot(\vec{x}-\vec{x}_0)} \\
&\quad |n,\vec{q},s\rangle \langle n,\vec{q},s|\,\bar{\chi}_\beta(x_0)\,|0\rangle \\
&= \sum_x e^{-i\vec{p}\cdot(\vec{x}-\vec{x}_0)} \sum_{n,\vec{q},s} e^{-E_{n,\vec{q}}(t-t_0)+i\vec{q}\cdot(\vec{x}-\vec{x}_0)} \\
&\quad \langle 0|\,\chi_\alpha(x_0)\,|n,\vec{q},s\rangle \langle n,\vec{q},s|\,\bar{\chi}_\beta(x_0)\,|0\rangle \\
&= \sum_{x,n,\vec{q},s} e^{-i(\vec{p}-\vec{q})\cdot\vec{x}}e^{-i(\vec{p}-\vec{q})\cdot\vec{x}_0}e^{-E_{n,\vec{q}}(t-t_0)} \langle 0|\,\chi_\alpha(x_0)\,|n,\vec{q},s\rangle \langle n,\vec{q},s|\,\bar{\chi}_\beta(x_0)\,|0\rangle
\end{aligned}
\tag{3.3}
$$

Using Fourier transform $\sum_x e^{-i(\vec{p}-\vec{q})\cdot\vec{x}} = N\delta_{\vec{p},\vec{q}}$,

$$
\begin{aligned}
G_{\alpha\beta}(t,\vec{p}) &= N\sum_{n,\vec{q},s} \delta(\vec{p}-\vec{q})e^{-i(\vec{p}-\vec{q})\cdot\vec{x}_0}e^{-E_{n,\vec{q}}(t-t_0)} \\
&\quad \langle 0|\,\chi_\alpha(x_0)\,|n,\vec{q},s\rangle \langle n,\vec{q},s|\,\bar{\chi}_\beta(x_0)\,|0\rangle \\
&= N\sum_{n,s} e^{-E_{n,\vec{p}}(t-t_0)} \langle 0|\,\chi_\alpha(x_0)\,|n,\vec{p},s\rangle \langle n,\vec{p},s|\,\bar{\chi}_\beta(x_0)\,|0\rangle \tag{3.4}
\end{aligned}
$$

where N is the number of total lattice sites, and the sum $\sum_n$ contains contributions from positive and negative parity excited states. Retaining only positive and negative parity ground state terms in the limit $(t-t_0) \gg 1$, one can rewrite the above equation as

$$
\begin{aligned}
G_{\alpha\beta}(t,\vec{p}) &= N\sum_s \Big(e^{-E_p^{0,+}(t-t_0)} \langle 0|\,\chi_\alpha(x_0)\,|0,\vec{p},s,+\rangle \langle 0,\vec{p},s,+|\,\bar{\chi}_\beta(x_0)\,|0\rangle \\
&\quad + e^{-E_p^{0,-}(t-t_0)} \langle 0|\,\chi_\alpha(x_0)\,|0,\vec{p},s,-\rangle \langle 0,\vec{p},s,-|\,\bar{\chi}_\beta(x_0)\,|0\rangle \Big) \tag{3.5}
\end{aligned}
$$

where $|0, \vec{p}, s, +\rangle$ is the positive-parity nucleon ground-state with energy $e^{-E_p^{(0,+)}}$ and $J^P = \frac{1}{2}^+$ and similarly for negative-parity ground-state with minus signs. Using Eqs. (8.31)-(8.35) in the Appendix 8.1.6, Eq. (3.5) can be written as

$$
\begin{aligned}
G_{\alpha\beta}(t, \vec{p}) &= N \sum_s e^{-E_p^{0,+}(t-t_0)} a^3 \phi^+ \sqrt{\frac{m^+}{N E_p^{0,+}}} u_\alpha(\vec{p}, s, +) a^3 \phi^+ \sqrt{\frac{m^+}{N E_p^{0,+}}} \bar{u}_\beta(\vec{p}, s, +) \\
&+ N \sum_s e^{-E_p^{0,-}(t-t_0)} a^3 \phi^- \sqrt{\frac{m^-}{N E_p^{0,-}}} \gamma_5 u_\alpha(\vec{p}, s, -) a^3 \phi^- \sqrt{\frac{m^-}{N E_p^{0,-}}} \bar{u}(\vec{p}, s, -) \gamma_5 \\
&= a^6 \frac{m^+}{E_p^{0,+}} |\phi^+|^2 e^{-E_p^{0,+}(t-t_0)} \sum_s u_\alpha(\vec{p}, s, +) \bar{u}_\beta(\vec{p}, s, +) \\
&\quad + a^6 \frac{m^-}{E_p^{0,-}} |\phi^-|^2 e^{-E_p^{0,-}(t-t_0)} \sum_s (\gamma_5 u(\vec{p}, s, -))_\alpha (\bar{u}(\vec{p}, s, -) \gamma_5))_\beta \\
&= a^6 \left[\frac{m^+}{E_p^{0,+}} |\phi^+|^2 e^{-E_p^{0,+}(t-t_0)} \left(\frac{-i\gamma \cdot p^+ + m^+}{2m^+} \right)_{\alpha\beta} \right. \\
&\quad \left. + \frac{m^-}{E_p^{0,-}} |\phi^-|^2 e^{-E_p^{0,-}(t-t_0)} \left[\gamma_5 \left(\frac{-i\gamma \cdot p^- + m^-}{2m^-} \right) \gamma_5 \right]_{\alpha\beta} \right]
\end{aligned}
$$

$$(3.6)$$

We want to obtain nucleon properties associated only with $J^p = \frac{1}{2}^+$. Various nucleon properties from the nucleon correlation function can be obtained by projecting out the negative-parity states and by taking the trace of positive-parity projection operator

$$
\Gamma_+ = \frac{1}{2} \left(1 + \frac{m^-}{E_p^{0,-}} \gamma_4 \right)
$$

$$(3.7)$$

with $G_{\alpha\beta}$.

Therefore,

$$
\begin{aligned}
\Gamma_{\beta\alpha} G_{\alpha\beta}(t,\vec{p}) \;=\;& a^6 \frac{m^+}{E_p^{0,+}} |\phi^+|^2 e^{-E_p^{0,+}(t-t_0)} \\
& \sum_s \bar{u}_\beta(\vec{p},s,+)\frac{1}{2}\Big(1+\frac{m^-}{E_p^{0,-}}\gamma_4\Big)_{\beta\alpha} u_\alpha(\vec{p},s,+) \\
& +a^6 \frac{m^-}{E_p^{0,-}} |\phi^-|^2 e^{-E_p^{0,-}(t-t_0)} \\
& \sum_s (\bar{u}(\vec{p},s,-)\gamma_5)_\beta \frac{1}{2}\Big(1+\frac{m^-}{E_p^{0,-}}\gamma_4\Big)_{\beta\alpha} (\gamma_5 u(\vec{p},s,-))_\alpha \\
=\;& a^6 \frac{m^+}{E_p^{0,+}} |\phi^+|^2 e^{-E_p^{0,+}(t-t_0)} \\
& \frac{1}{2}\Big(\sum_s \bar{u}_\beta(\vec{p},s,+)\Big(1+\frac{m^-}{E_p^{0,-}}\gamma_4\Big)_{\beta\alpha} u_\alpha(\vec{p},s,+)\Big) \\
& +a^6 \frac{m^-}{E_p^{0,-}} |\phi^-|^2 e^{-E_p^{0,-}(t-t_0)} \\
& \frac{1}{2}\Big(\sum_s \bar{u}_\beta(\vec{p},s,-)\Big(1-\frac{m^-}{E_p^{0,-}}\gamma_4\Big)_{\beta\alpha} u_\alpha(p,s,-)\Big) \\
=\;& a^6 \frac{m^+}{E_p^{0,+}} |\phi^+|^2 e^{-E_p^{0,+}(t-t_0)}\frac{1}{2}\sum_s \Big(\bar{u}_\beta(\vec{p},s,+)(\mathbb{1})_{\beta\alpha} u_\alpha(\vec{p},s,+) \\
& +\frac{m^-}{E_p^{0,-}}\bar{u}_\beta(\vec{p},s,+)(\gamma_4)_{\beta\alpha} u_\alpha(\vec{p},s,+)\Big) \\
& +a^6 \frac{m^-}{E_p^{0,-}} |\phi^-|^2 e^{-E_p^{0,-}(t-t_0)}\frac{1}{2}\sum_s \Big(\bar{u}_\beta(\vec{p},s,-)(\mathbb{1})_{\beta\alpha} u_\alpha(\vec{p},s,-) \\
& -\frac{m^-}{E_p^{0,-}}\bar{u}_\beta(\vec{p},s,-)(\gamma_4)_{\beta\alpha} u_\alpha(\vec{p},s,-)\Big)
\end{aligned}
\tag{3.8}
$$

To simply Eq. (3.8), we can use the Gordon identity which is derived in the following.

3.1.1 Gordon Identity

With $\sigma_{\mu\nu} = \frac{1}{2i}[\gamma_\mu,\gamma_\nu]$ and $q_\nu = p_\nu - p'_\nu$,

$$
\begin{aligned}
i\sigma_{\mu\nu}q_\nu \;&=\; \frac{1}{2}[\gamma_\mu,\gamma_\nu](p_\nu - p'_\mu) \\
&=\; \frac{1}{2}[\gamma_\mu\gamma_\nu p_\nu - \gamma_\mu\gamma_\nu p'_\nu - \gamma_\nu\gamma_\mu p_\nu + \gamma_\nu\gamma_\mu p'_\nu]
\end{aligned}
$$

Since $\gamma_\mu\gamma_\nu = -\gamma_\nu\gamma_\mu + 2\delta_{\mu\nu}$,

$$
\begin{aligned}
i\sigma_{\mu\nu}q_\nu &= \frac{1}{2}\Big((-\gamma_\nu\gamma_\mu + 2\delta_{\mu\nu})p_\nu - \gamma_\mu\gamma_\nu p'_\nu \\
&\quad -\gamma_\nu\gamma_\mu p_\nu + (-\gamma_\mu\gamma_\nu + 2\delta_{\mu\nu})p'_\nu\Big) \\
&= \frac{1}{2}\Big(-\slashed{p}\gamma_\mu - \gamma_\mu\slashed{p}' - \gamma_\nu\gamma_\mu p_\nu + 2\delta_{\mu\nu}p_\nu - \gamma_\mu\gamma_\nu p'_\nu + 2\delta_{\mu\nu}p'_\nu\Big) \\
&= \frac{1}{2}\Big(-2\slashed{p}\gamma_\mu - 2\gamma_\mu\slashed{p}' + 2p_\mu + 2p'_\mu\Big) \\
&= -\slashed{p}\gamma_\mu - \gamma_\mu\slashed{p}' + p_\mu + p'_\mu
\end{aligned}
\tag{3.9}
$$

Using the Dirac Eq. from Appendix 8.1,

$$
\begin{aligned}
\bar{u}(p',s')(i\sigma_{\mu\nu}q_\nu)u(p,s) &= \bar{u}(p',s')(-\slashed{p}\gamma_\mu - \gamma_\mu\slashed{p}' + p_\mu + p'_\mu)u(p,s) \\
&= \bar{u}(p',s')(-2im\gamma_\mu + p_\mu + p'_\mu)u(p,s) \\
\Rightarrow \bar{u}(p',s')(2im)\gamma_\mu u(p,s) &= \bar{u}(p',s')\big((p_\mu + p'_\mu) - i\sigma_{\mu\nu}q_\nu\big)u(p,s) \\
\Rightarrow \bar{u}(p',s')\gamma_\mu u(p,s) &= \bar{u}(p',s')\left(-i\frac{(p_\mu + p'_\mu)}{2m} - \frac{\sigma_{\mu\nu}q_\nu}{2m}\right)u(p,s)
\end{aligned}
\tag{3.10}
$$

Using Eq. (8.35) and (3.10), we can write Eq. (3.8) as

$$
\begin{aligned}
\Gamma_{\beta\alpha}G_{\alpha\beta}(t,\vec{p}) &= a^6\frac{m^+}{E_p^{0,+}}|\phi^+|^2 e^{-E_p^{0,+}(t-t_0)}\frac{1}{2}\sum_s\left(1 + \frac{m^-}{E_p^{0,-}}\frac{2(-ip_4^+)}{2m^+}\right) \\
&\quad + a^6\frac{m^-}{E_p^{0,-}}|\phi^-|^2 e^{-E_p^{0,-}(t-t_0)}\frac{1}{2}\sum_s\left(1 - \frac{m^-}{E_p^{0,-}}\frac{2(-ip_4^+)}{2m^-}\right) \\
&= a^6\frac{m^+}{E_p^{0,+}}|\phi^+|^2 e^{-E_p^{0,+}(t-t_0)}\frac{1}{2}\sum_s\left(1 + \frac{m^-}{E_p^{0,-}}\frac{E_p^{0,+}}{m^+}\right) \\
&\quad + a^6\frac{m^-}{E_p^{0,-}}|\phi^-|^2 e^{-E_p^{0,-}(t-t_0)}\frac{1}{2}\sum_s\left(1 - \frac{m^-}{E_p^{0,-}}\frac{E_p^{0,-}}{m^-}\right) \\
&= a^6\frac{m^+}{E_p^{0,+}}|\phi^+|^2 e^{-E_p^{0,+}(t-t_0)}\left(1 + \frac{m^-}{E_p^{0,-}}\frac{E_p^{0,+}}{m^+}\right)
\end{aligned}
\tag{3.11}
$$

In our numerical simulation, we use $\Gamma_4 \equiv \Gamma_e \equiv \frac{1 \pm \gamma_4}{2}$. Then, from Eq. (3.10),

$$
\begin{aligned}
\Gamma_{\beta\alpha} G_{\alpha\beta}(t, \vec{p}) &= a^6 \frac{m^+}{E_p^{0,+}} |\phi^+|^2 e^{-E_p^{0,+}(t-t_0)} \frac{1}{2} \sum_s \left(1 + \frac{2(-ip_4^+)}{2m^+} \right) \\
&\quad + a^6 \frac{m^-}{E_p^{0,-}} |\phi^-|^2 e^{-E_p^{0,-}(t-t_0)} \frac{1}{2} \sum_s \left(1 - \frac{2(-ip_4^-)}{2m^-} \right) \\
&= a^6 \frac{m^+}{E_p^{0,+}} |\phi^+|^2 e^{-E_p^{0,+}(t-t_0)} \frac{1}{2} \sum_s \frac{2m^+ + 2E_p^{0,+}}{2m^+} \\
&\quad + a^6 \frac{m^-}{E_p^{0,-}} |\phi^-|^2 e^{-E_p^{0,-}(t-t_0)} \frac{1}{2} \sum_s \frac{2m^- - 2E_p^{0,-}}{2m^-} \\
&= a^6 |\phi^+|^2 e^{-E_p^{0,+}(t-t_0)} \frac{E_p^{0,+} + m^+}{E_p^{0,+}} \\
&\quad + a^6 |\phi^-|^2 e^{-E_p^{0,-}(t-t_0)} \frac{m^- - E_p^{0,-}}{E_p^{0,-}} \\
&= a^6 |\phi^+|^2 e^{-E_p^{0,+}(t-t_0)} \frac{E_p^{0,+} + m^+}{E_p^{0,+}} \\
&\quad + a^6 |\phi^-|^2 e^{-E_p^{0,-}(t-t_0)} \frac{(m^- - \sqrt{(m^-)^2 + \vec{p}^2})}{E_p^{0,-}} \quad (3.12)
\end{aligned}
$$

If one has $\frac{\vec{p}^2}{m^-} \ll 1$,

$$
\begin{aligned}
\mathrm{Tr}\left[\Gamma_e G(t, \vec{p}) \right] &= a^6 |\phi^+|^2 e^{-E_p^{0,+}(t-t_0)} \frac{E_p^{0,+} + m^+}{E_p^{0,+}} \\
&\quad - a^6 |\phi^-|^2 \frac{e^{-E_p^{0,-}(t-t_0)}}{E_p^{0,-}} \frac{1}{2} \frac{\vec{p}^2}{(m^-)^2} \quad (3.13)
\end{aligned}
$$

For a final nucleon state at rest ($\vec{p} = 0$),

$$
\begin{aligned}
G_{NN}(t, \vec{p}, \Gamma_e) &\equiv \mathrm{Tr}[\Gamma_e G(t, \vec{p})] \\
&= a^6 |\phi_0^+|^2 e^{-m^+(t-t_0)} \quad (3.14)
\end{aligned}
$$

Therefore, it is seen from Eq. (3.13) that the negative parity states are not completely suppressed unless for zero nucleon momentum and so the nucleon with non-zero momentum has contamination from the negative-parity states in the correlation function. However, this contamination is exponentially suppressed in the long time limit as the negative-parity ground-state has higher mass and energy than the positive-parity ground state.

For simplicity in the notation of subsequent calculations, we will re-write Eq. (3.11) with the choice of positive-parity projection operator $\Gamma_e = \frac{1+\gamma_4}{2}$ as,

$$
\begin{aligned}
\Gamma_{\beta\alpha}G_{\alpha\beta}(t,\vec{p}) \quad &\equiv \quad \mathrm{Tr}[\Gamma_e G(t,\vec{p})] \equiv G_{NN}(t,\vec{p},\Gamma_e) \\
&\xrightarrow{(t-t_0)\gg 1} \quad a^6 \frac{m}{E_p}|\phi(p)|^2 e^{-E_p(t-t_0)}\left(1 + \frac{E_p}{m}\right) \\
&= \quad a^6 \frac{E_p + m}{E_p}|\phi(p)|^2 e^{-E_p(t-t_0)},
\end{aligned}
\tag{3.15}
$$

where we have used simple notations as $m \equiv m^+$, $E_p \equiv E_p^{0,+}$, and $\phi \equiv \phi^+$.

Chapter 4 Lattice Formalism: Three-Point Nucleon Correlation Function

4.1   Schematic Representation of Connected and Disconnected Insertions

In this section of the chapter, we present simple schematic representation of connected and disconnected insertions in terms of quarks and quark propagators. We shall present a formal derivation of nucleon three-point correlation function to calculate electromagnetic form factors in section (4.2). Nucleon three-point functions are classified according to two different topologies of the quark lines connected between the source and the sink of the proton−called connected and disconnected insertions. When the current is connected to the nucleon through the quark lines, we refer to it as connected insertion (CI). When the quark fields of the current contract between themselves, we refer it to as disconnected insertion (DI). These disconnected quark loops are connected to the quark lines in the nucleon propagator through fluctuating gauge background fields.

Let us consider three-point correlator with source momentum $\vec{p}'$ and sink momentum $\vec{p}$:

$$\mathcal{C}_{\alpha\beta}^{\mathcal{O}_q}(t, \tau; \vec{p}, \vec{p}') = \langle \chi_\alpha(t, \vec{p}) \mathcal{O}_q(\tau) \bar{\chi}_\beta(0, \vec{p}') \rangle \tag{4.1}$$

where the operator insertion with quark q-flavored current is written as

$$\mathcal{O}_q(\tau) = \sum_{\vec{y}, v, w} \bar{q}_\alpha^a(v) \mathbb{O}_{\alpha\beta}^{ab}(v, w; \vec{y}, \tau) q_\beta^b(w) \tag{4.2}$$

Then the positive-parity contracted correlator is

$$
\begin{aligned}
\mathcal{C}^{\mathcal{O}_q}(t,\tau;\vec{p},\vec{p}') &= \Gamma_{\beta\alpha}\langle\chi_\alpha(t,\vec{p})\mathcal{O}_q(\tau)\bar{\chi}_\beta(0,\vec{p}')\rangle \\
&= \sum_{\vec{y},v,w}\sum_{\vec{x},\vec{z}'}e^{-i\vec{p}\cdot\vec{x}}e^{i\vec{p}'\cdot\vec{z}'}\epsilon_{abc}\epsilon_{a',b',c'}(C\gamma_5)_{\gamma\delta}(\gamma_5 C^{-1})_{\rho\sigma}\Gamma_{\beta\alpha} \\
&\quad \langle u_\alpha^a(\vec{x},t)u_\gamma^b(\vec{x},t)d_\delta^c(\vec{x},t)\bar{q}_\lambda^d(v)\mathbb{O}_{\lambda\kappa}^{de}(v,w,\vec{y},\tau)q_\kappa^e(w) \\
&\quad \bar{u}_\beta^{a'}(\vec{z}',0)\bar{d}_\rho^{b'}(\vec{z}',0)\bar{u}_\sigma^{c'}(\vec{z}',0)\rangle
\end{aligned}
$$

$$(4.3)$$

4.1.1 $q = u$-quarks

If $q = u$, we obtain four connected contractions and two disconnected contractions as shown in FIGS. 4.1a - 4.1f. We can use translational invariance to shift all $\vec{z}'$ to zero and obtain a factor N_s from the sum over $\vec{z}'$ sum. Denoting a quark propagator by S, from FIG. 4.1a,

$$
\begin{aligned}
\text{CI-FIG(4.1a)} \Rightarrow\ & S_{\delta\rho}^{cb'}[d](\vec{x},\vec{0},0)\cdot S_{\kappa\beta}^{ea'}[u](w,\vec{0},0)\cdot S_{\alpha\lambda}^{ad}[u](\vec{x},t,v) \\
& S_{\gamma\sigma}^{bc'}[u](\vec{x},t,\vec{0},0)
\end{aligned}
$$

$$(4.4)$$

$$
\begin{aligned}
\text{CI-FIG(4.1b)} \Rightarrow\ & S_{\delta\rho}^{cb'}[d](\vec{x},t,\vec{0},0)\cdot S_{\gamma\lambda}^{bd}[u](\vec{x},t,v)\cdot S_{\alpha\beta}^{aa'}[u](\vec{x},t,\vec{0},0)\cdot \\
& S_{\kappa\sigma}^{ec'}[u](w,\vec{0},0)
\end{aligned}
$$

$$(4.5)$$

$$
\begin{aligned}
\text{CI-FIG(4.1c)} \Rightarrow\ & -S_{\gamma\lambda}^{bd}[u](\vec{x},t,v)\cdot S_{\kappa\beta}^{ea'}[u](w,\vec{0},0)\cdot S_{\delta\rho}^{cb'}[d](\vec{x},t,\vec{0},0)\cdot \\
& S_{\alpha\sigma}^{ac'}[u](\vec{x},t,\vec{0},0)
\end{aligned}
$$

$$(4.6)$$

$$
\begin{aligned}
\text{CI-FIG(4.1d)} \Rightarrow\ & -S_{\delta\rho}^{cb'}[d](\vec{x},t,\vec{0},0)\cdot S_{\alpha\lambda}^{ad}[u](\vec{x},t,v)\cdot S_{\gamma\beta}^{ba'}[u](\vec{x},t,\vec{0},0)\cdot \\
& S_{\kappa\sigma}^{ec'}[u](w,\vec{0},0)
\end{aligned}
$$

$$(4.7)$$
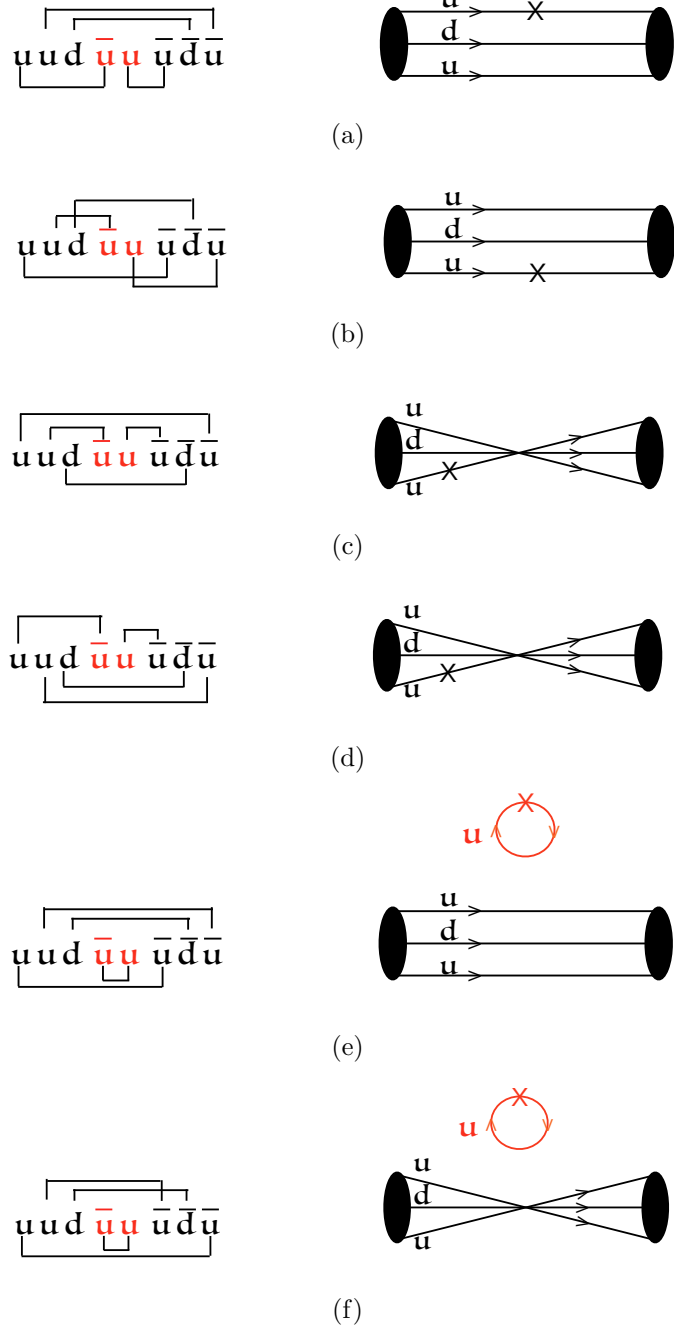
Figure 4.1: Schematic diagrams of connected and disconnected insertions when $q = u$.

$$\text{DI-FIG(4.1e)} \quad \Rightarrow \quad -S^{cb'}_{\delta\rho}[d](\vec{x},t,\vec{0},0) \cdot S^{ed}_{\kappa\lambda}[u](w,v) \cdot S^{aa'}_{\alpha\beta}[u](\vec{x},t,\vec{0},0) \cdot$$
$$S^{bc'}_{\gamma\sigma}[u](\vec{x},t,\vec{0},0) \tag{4.8}$$

$$\text{DI-FIG(4.1f)} \quad \Rightarrow \quad S^{cb'}_{\delta\rho}[d](\vec{x},t,\vec{0},0) \cdot S^{ed}_{\kappa\lambda}[u](w,v) \cdot S^{ba'}_{\gamma\beta}[u](\vec{x},t,\vec{0},0) \cdot$$
$$S^{ac'}_{\alpha\sigma}[u](\vec{x},t,\vec{0},0) \tag{4.9}$$

Therefore,

$$
\begin{aligned}
\mathcal{C}^{\mathcal{O}_u}(t,\tau;\vec{p}) \;=\; & N_s \sum_{\vec{x},\vec{y},v,w} e^{-i\vec{p}\cdot\vec{x}} \epsilon_{abc}\epsilon_{a'b'c'}\Gamma_{\beta\alpha}\Bigg[\\
& S^{ad}_{\alpha\lambda}[u](\vec{x},t,v) \cdot \mathbb{O}^{de}_{\lambda\kappa}(v,w,\vec{y},\tau)S^{ea'}_{\kappa\beta}[u](w,\vec{0},0) \\
& \text{Tr}\Bigg(S^{cb'}_{\delta\rho}[d](\vec{x},\vec{0},0)(\gamma_5 C^{-1})_{\rho\sigma}S^{bc'}_{\sigma\gamma}[u](\vec{x},t,\vec{0},0)(C\gamma_5)_{\gamma\delta} \Bigg) \\
& + S^{aa'}_{\alpha\beta}[u](\vec{x},t,\vec{0},0) \\
& \text{Tr}\Bigg(S^{cb'}_{\delta\rho}[d](\vec{x},t,\vec{0},0)(\gamma_5 C^{-1})_{\rho\sigma}S^{ec'}_{\sigma\kappa}[u](w,\vec{0},0) \\
& \mathbb{O}^{de}_{\lambda\kappa}(v,w,\vec{y},\tau)S^{bd}_{\lambda\gamma}[u](\vec{x},t,v)(C\gamma_5)_{\gamma\delta} \Bigg) \\
& - S^{ac'}_{\alpha\sigma}[u](\vec{x},t,\vec{0},0)(\gamma_5 C^{-1})_{\sigma\rho}S^{cb'}_{\rho\delta}[d](\vec{x},t,\vec{0},0)(C\gamma_5)_{\delta\gamma} \\
& S^{bd}_{\gamma\lambda}[u](\vec{x},t,v)\mathbb{O}^{de}_{\lambda\kappa}(v,w,\vec{y},\tau)S^{ea'}_{\kappa\beta}[u](w,\vec{0},0) \\
& - S^{ad}_{\alpha\lambda}[u](\vec{x},t,v)\mathbb{O}^{de}_{\lambda\kappa}(v,w,\vec{y},\tau)S^{ec'}_{\kappa\sigma}[u](w,\vec{0},0)(\gamma_5 C^{-1})_{\sigma\rho} \\
& S^{cb'}_{\rho\delta}[d](\vec{x},t,\vec{0},0)(C\gamma_5)_{\delta\gamma}S^{ba'}_{\gamma\beta}[u](\vec{x},t,\vec{0},0) \\
& - S^{aa'}_{\alpha\beta}[u](\vec{x},t,\vec{0},0)\text{Tr}\Bigg(S^{ed}_{\kappa\lambda}[u](w,v)\mathbb{O}^{de}_{\lambda\kappa}(v,w,\vec{y},\tau) \Bigg) \\
& \text{Tr}\Bigg(S^{cb'}_{\delta\rho}[d](\vec{x},t,\vec{0},0)(\gamma_5 C^{-1})_{\rho\sigma}S^{bc'}_{\sigma\gamma}[u](\vec{x},t,\vec{0},0)(C\gamma_5)_{\gamma\delta} \Bigg) \\
& + S^{ac'}_{\alpha\sigma}[u](\vec{x},t,\vec{0},0)(\gamma_5 C^{-1})_{\sigma\rho}S^{cb'}_{\rho\delta}[d](\vec{x},t,\vec{0},0)(C\gamma_5)_{\delta\gamma} \\
& S^{ba'}_{\gamma\beta}[u](\vec{x},t,\vec{0},0)\text{Tr}\Bigg(S^{ed}_{\kappa\lambda}[u](w,v)\mathbb{O}^{de}_{\lambda\kappa}(v,w,\vec{y},\tau) \Bigg) \Bigg]
\end{aligned}
\tag{4.10}
$$

$$\Rightarrow \mathcal{C}^{\mathcal{O}_u}(t,\tau;\vec{p}) = N_s \sum_{\vec{x},\vec{y},v,w} e^{-i\vec{p}\cdot\vec{x}} \epsilon_{abc}\epsilon_{a'b'c'} \Bigg[$$

$$-\mathrm{Tr}\left(\Gamma S^{ad}[u](x,v)\mathbb{O}^{de}(v,w,y)S^{ea'}[u](w,0)\right)\mathrm{Tr}\left(S^{bb'}[u](x,0)\underline{S}^{cc'}[d](x,0)\right)$$

$$-\mathrm{Tr}\left(\Gamma S^{aa'}[u](x,0)\right)\mathrm{Tr}\left(\underline{S}^{cc'}[d](x,0)S^{bd}[u](x,v)\mathbb{O}^{de}(v,w,y)S^{eb'}[u](w,0)\right)$$

$$-\mathrm{Tr}\left(\Gamma S^{aa'}[u](x,0)\underline{S}^{cc'}[d](x,0)S^{bd}[u](x,v)\mathbb{O}^{de}(v,w,y)S^{eb'}[u](w,0)\right)$$

$$-\mathrm{Tr}\left(\Gamma S^{ad}[u](x,v)\mathbb{O}^{de}(v,w,y)S^{ea'}[u](w,0)\underline{S}^{cc'}[d](x,0)S^{bb'}[u](x,0)\right)$$

$$+\mathrm{Tr}\left(\Gamma S^{aa'}[u](x,0)\right)$$

$$\mathrm{Tr}\left(S^{ed}[u](w,v)\mathbb{O}^{de}(v,w,y)\right)\mathrm{Tr}\left(S^{bb'}[u](x,0)\underline{S}^{cc'}[d](x,0)\right)$$

$$+\mathrm{Tr}\left(\Gamma S^{aa'}[u](x,0)\underline{S}^{cc'}[d](x,0)S^{bb'}[u](x,0)\right)$$

$$\mathrm{Tr}\left(S^{ed}[u](w,v)\mathbb{O}^{de}(v,w,y)\right)\Bigg] \tag{4.11}$$

The $5th$ and $6th$ terms correspond to disconnected insertions. The notation Tr denotes trace over both color and Dirac indices. For simplicity, we also have used the following shorthand notation

$$\begin{aligned} \underline{S} &= \left((\gamma_5 C^{-1})S(C\gamma_5)\right)^T \\ &= \gamma_5 C^{-1} S^T C \gamma_5 \end{aligned} \tag{4.12}$$

where, T denotes transpose over Dirac indices.

4.1.2 $q = d$-quarks

If $q = d$, we obtain four connected contractions and two disconnected contractions as shown in FIGS. 4.2a - 4.2d.

$$\text{CI-FIG(4.2a)} \quad \Rightarrow \quad S_{\delta\lambda}^{cd}[d](\vec{x}, t, v) \cdot S_{\kappa\rho}^{eb'}[d](w, \vec{0}, 0) \cdot S_{\alpha\beta}^{aa'}[u](\vec{x}, t, \vec{0}, 0) \cdot$$
$$S_{\gamma\sigma}^{bc'}[u](\vec{x}, t, \vec{0}, 0) \tag{4.13}$$

$$\text{CI-FIG(4.2b)} \quad \Rightarrow \quad -S_{\delta\lambda}^{cd}[d](\vec{x}, t, v) \cdot S_{\kappa\rho}^{eb'}[d](w, \vec{0}, 0) \cdot S_{\gamma\beta}^{ba'}[u](\vec{x}, t, \vec{0}, 0) \cdot$$
$$S_{\alpha\sigma}^{ac'}[u](\vec{x}, t, \vec{0}, 0)$$

$$\tag{4.14}$$

$$\text{DI-FIG(4.2c)} \quad \Rightarrow \quad -S_{\delta\lambda}^{ed}[d](w, v) \cdot S_{\delta\rho}^{cb'}[d](\vec{x}, t, \vec{0}, 0) \cdot S_{\alpha\beta}^{aa'}[u](\vec{x}, t, \vec{0}, 0) \cdot$$
$$S_{\gamma\sigma}^{bc'}[u](\vec{x}, t, \vec{0}, 0) \tag{4.15}$$

$$\text{DI-FIG(4.2d)} \quad \Rightarrow \quad S_{\kappa\lambda}^{ed}[d](w, v) \cdot S_{\delta\rho}^{cb'}[d](\vec{x}, t, \vec{0}, 0) \cdot S_{\gamma\beta}^{ba'}[u](\vec{x}, t, \vec{0}, 0) \cdot$$
$$S_{\alpha\sigma}^{ac'}[u](\vec{x}, t, \vec{0}, 0) \tag{4.16}$$

(a)

(b)

(c)

(d)
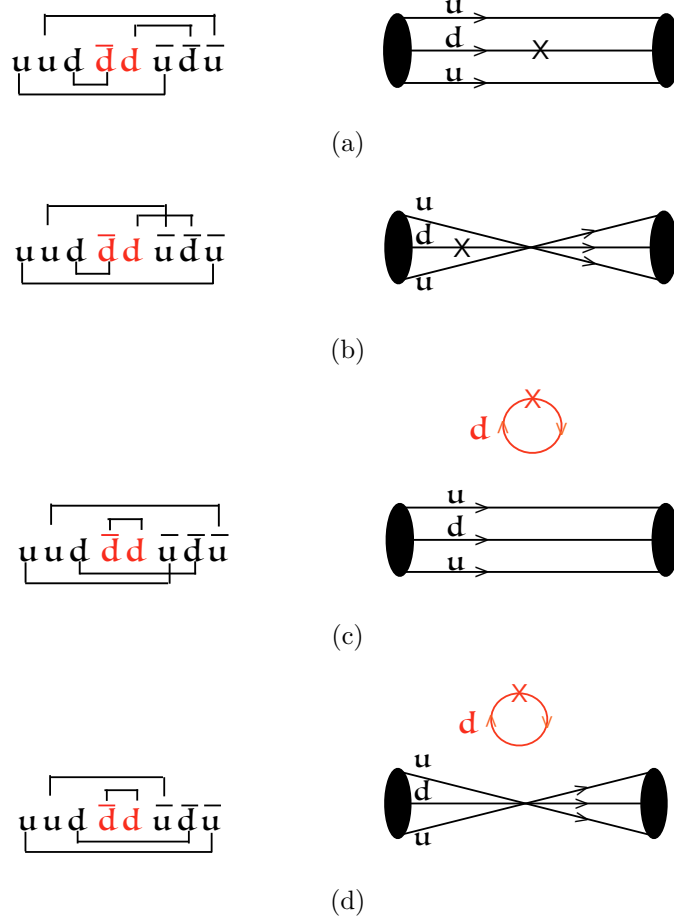
Figure 4.2: Schematic diagrams of connected and disconnected insertions when $q = d$.

Down quark insertion:

$$
\mathcal{C}^{\mathcal{O}_d}(t, \tau; \vec{p}) = N_s \sum_{\vec{x}, \vec{y}, v, w} e^{-i\vec{p} \cdot \vec{x}} \epsilon_{abc} \epsilon_{a'b'c'} \Gamma_{\beta\alpha} \Bigg[S^{aa'}_{\alpha\beta}[u](\vec{x}, t, \vec{0}, 0)
$$

$$
\mathrm{Tr}\Bigg(S^{bc'}_{\gamma\sigma}[u](\vec{x}, t, \vec{0}, 0)(\gamma_5 C^{-1})_{\sigma\rho} S^{eb'}_{\rho\kappa}[d](w, \vec{0}, 0) \mathbb{O}^{de}_{\kappa\lambda}(v, w, \vec{y}, \tau) S^{cd}_{\lambda\delta}[d](\vec{x}, t, v)(C\gamma_5)_{\delta\gamma} \Bigg)
$$

$$
- S^{ac'}_{\alpha\sigma}[u](\vec{x}, t, \vec{0}, 0)(\gamma_5 C^{-1})_{\sigma\rho} S^{eb'}_{\rho\kappa}[d](w, \vec{0}, 0) \mathbb{O}^{de}_{\kappa\lambda}(v, w, \vec{y}, \tau)
$$

$$
S^{cd}_{\lambda\delta}[d](\vec{x}, t, v)(C\gamma_5)_{\delta\gamma} \cdot S^{ba'}_{\gamma\beta}[u](\vec{x}, t, \vec{0}, 0)
$$

$$
- S^{aa'}_{\alpha\beta}[u](\vec{x}, t, \vec{0}, 0) \, \mathrm{Tr}\Bigg(S^{ed}_{\delta\lambda}[d](w, v) \mathbb{O}^{de}_{\lambda\kappa}(v, w, \vec{y}, \tau) \Bigg)
$$

$$
\mathrm{Tr}\Bigg(S^{cb'}_{\delta\rho}[d](\vec{x}, t, \vec{0}, 0)(\gamma_5 C^{-1})_{\rho\sigma} S^{bc'}_{\sigma\gamma}[u](\vec{x}, t, \vec{0}, 0)(C\gamma_5)_{\gamma\delta} \Bigg)
$$

$$
+ S^{ac'}_{\alpha\sigma}[u](\vec{x}, t, \vec{0}, 0)(\gamma_5 C^{-1})_{\sigma\rho} S^{cb'}_{\rho\delta}[d](\vec{x}, t, \vec{0}, 0) S^{ba'}_{\gamma\beta}[u](\vec{x}, t, \vec{0}, 0)
$$

$$
\mathrm{Tr}\Bigg(S^{ed}_{\kappa\lambda}[d](w, v) \mathbb{O}^{de}_{\lambda\kappa}(v, w, \vec{y}, \tau) \Bigg) \Bigg]
$$

22

(4.17)

$$\Rightarrow \mathcal{C}^{\mathcal{O}_d}(t, \tau; \vec{p}) = N_s \sum_{\vec{x}, \vec{y}, v, w} e^{-i\vec{p}\cdot\vec{x}} \epsilon_{abc} \epsilon_{a'b'c'} \Bigg[$$

$$-\text{Tr}\Bigg(\Gamma S^{aa'}[u](x,0)\Bigg)\text{Tr}\Bigg(\underline{S}^{cc'}[u](x,0)S^{bd}[d](x,v)\mathbb{O}^{de}(v,w,y)S^{eb'}[d](w,0)\Bigg)$$

$$-\text{Tr}\Bigg(\underline{S}^{aa'}[u](x,0)\Gamma\underline{S}^{bb'}[u](x,0)S^{cd}[d](x,v)\mathbb{O}^{de}(v,w,y)S^{ec'}[d,LS](w,0)\Bigg)$$

$$+\text{Tr}\Bigg(\Gamma S^{aa'}[u](x,0)\Bigg)\text{Tr}\Bigg(S^{ed}[d](w,v)\mathbb{O}^{de}(w,v,y)\Bigg)\text{Tr}\Bigg(S^{bc'}[u](x,0)\underline{S}^{cb'}[d](x,0)\Bigg)$$

$$+\text{Tr}\Bigg(\Gamma S^{aa'}[u](x,0)\underline{S}^{cc'}[d](x,0)S^{bb'}[u](x,0)\Bigg)\text{Tr}\Bigg(S^{ed}[d](w,v)\mathbb{O}^{de}(v,w,y)\Bigg)\Bigg]$$

$$(4.18)$$

In the above expression $3rd$ and $4th$ terms correspond to disconnected insertions.

4.2 Lattice Formalism: Three-Point Correlation Functions

Based on the calculation in Chapter 3, we shall now derive a generalized expression for a nucleon three-point correlation function. The generic nucleon three-point correlation function for an electromagnetic current $\mathcal{J}_\mu$ is defined as

$$G_{\alpha\beta;N\mathcal{J}_\mu N}(t_2, t_1, \vec{p}, \vec{p}') = \sum_{\vec{x}_1, \vec{x}_2} e^{-i\vec{p}\cdot(\vec{x}_2 - \vec{x}_1)} e^{-i\vec{p}'\cdot(\vec{x}_1 - \vec{x}_0)} \langle 0| \chi_\alpha(x_2)\mathcal{J}_\mu(x_1)\bar{\chi}_\beta(x_0) |0\rangle$$

$$(4.19)$$

where

$$
\begin{aligned}
t_2 &: \text{nucleon sink time,} \\
t_1 &: \text{current insertion time,} \\
t_0 &: \text{nucleon source time,} \\
\vec{x}_2 &: \text{nucleon sink spatial position,} \\
\vec{x}_1 &: \text{current insertion spatial position,} \\
\vec{x}_0 &: \text{nucleon source spatial position,} \\
\vec{p}\,' &: \text{nucleon source momentum,} \\
\vec{p} &: \text{nucleon sink momentum.}
\end{aligned}
$$

The convention we follow for momentum transfer q is the difference between sink and source momentum:

$$
q = p - p' \tag{4.20}
$$

We now insert a complete set of energy eigenstates with principle quantum number n, momentum q, spin s and assume $t_2 > t_1 > t_0$. Then

$$
G_{\alpha\beta;N\mathcal{J}_\mu N}\ (t_2,t_1,\vec{p},\vec{p}\,') = \sum_{\vec{x}_1,\vec{x}_2} e^{-i\vec{p}\cdot(\vec{x}_2-\vec{x}_1)} e^{-i\vec{p}\,'\cdot(\vec{x}_1-\vec{x}_0)} \sum_{\vec{q}_2,s}\sum_{\vec{q}_1,s'} \langle 0|\,\chi_\alpha(x_2)\,|\vec{q}_2,s\rangle
$$

$$
\langle \vec{q}_2,s|\,\mathcal{J}_\mu(x_1)\,|\vec{q}_1,s'\rangle \langle \vec{q}_1,s'|\,\bar{\chi}_\beta(x_0)\,|0\rangle
$$

$$
= \sum_{\vec{x}_1,\vec{x}_2} e^{-i\vec{p}\cdot(\vec{x}_2-\vec{x}_1)} e^{-i\vec{p}\,'\cdot(\vec{x}_1-\vec{x}_0)} \sum_{\vec{q}_2,s}\sum_{\vec{q}_1,s'} \langle 0|\, e^{H(t_2-t_0)-i\vec{q}_2'\cdot(\vec{x}_2-\vec{x}_0)}
$$

$$
\chi_\alpha(x_0) e^{-H(t_2-t_0)+i\vec{q}_2'\cdot(\vec{x}_2-\vec{x}_0)}\,|\vec{q}_2,s\rangle \langle \vec{q}_2,s|
$$

$$
e^{H(t_1-t_0)-i\vec{q}_1'\cdot(\vec{x}_1-\vec{x}_0)} \mathcal{J}_\mu(x_0) e^{-H(t_1-t_0)+i\vec{q}_1'\cdot(\vec{x}_1-\vec{x}_0)}\,|\vec{q}_1,s'\rangle
$$

$$
\langle \vec{q}_1,s'|\bar{\chi}_\beta(x_0)\rangle
$$

$$
= \sum_{\vec{x}_1,\vec{x}_2} e^{-i\vec{p}\cdot(\vec{x}_2-\vec{x}_1)} e^{-i\vec{p}\,'\cdot(\vec{x}_1-\vec{x}_0)} \sum_{\vec{q}_2,s}\sum_{\vec{q}_1,s'} e^{-E_{q_2}(t_2-t_0)+i\vec{q}_2\cdot(\vec{x}_2-\vec{x}_0)}
$$

$$
e^{-E_{q_2}(t_1-t_0)-i\vec{q}_2\cdot(\vec{x}_1-\vec{x}_0)} e^{-E_{q_1}(t_1-t_0)+i\vec{q}_1\cdot(\vec{x}_1-\vec{x}_0)}
$$

$$
\langle 0|\,\chi_\alpha(x_0)\,|\vec{q}_2,s\rangle \langle \vec{q}_2,s|\,\mathcal{J}_\mu(x_0)\,|\vec{q}_1,s'\rangle \langle \vec{q}_1,s'|\,\bar{\chi}_\beta(x_0)\,|0\rangle
$$

$$
= \sum_{\vec{x}_1,\vec{x}_2}\sum_{\vec{q}_2,s}\sum_{\vec{q}_1,s'} e^{-i\vec{p}\cdot\vec{x}_2+i\vec{p}\cdot\vec{x}_1-i\vec{p}\,'\cdot\vec{x}_1+i\vec{p}\,'\cdot\vec{x}_1+i\vec{p}\,'\cdot\vec{x}_0+i\vec{q}_2\cdot\vec{x}_2}
$$

$$
e^{-i\vec{q}_2\cdot\vec{x}_0-i\vec{q}_2\cdot\vec{x}_1+i\vec{q}_2\cdot\vec{x}_0+i\vec{q}_1\cdot\vec{x}_1-i\vec{q}_1\cdot\vec{x}_0} e^{-E_{q_2}(t_2-t_0-t_1+t_0)} e^{-E_{q_1}(t_1-t_0)}
$$

$$
\langle 0|\,\chi_\alpha(x_0)\,|\vec{q}_2,s\rangle \langle \vec{q}_2,s|\,\mathcal{J}_\mu(x_0)\,|\vec{q}_1,s'\rangle \langle \vec{q}_1,s'|\,\bar{\chi}_\beta(x_0)\,|0\rangle
$$

$$
= \sum_{\vec{x}_1,\vec{x}_2}\sum_{\vec{q}_2,s}\sum_{\vec{q}_1,s'} e^{-i(\vec{p}-\vec{q}_2)\cdot\vec{x}_2} e^{-i(\vec{p}\,'-\vec{p}+\vec{q}_2-\vec{q}_1)\cdot\vec{x}_1} e^{i(\vec{p}\,'-\vec{q}_1)\cdot x_0}
$$

$$
e^{-E_{q_2}(t_2-t_1)} e^{-E_{q_1}(t_1-t_1)} \langle 0|\,\chi_\alpha(x_0)\,|\vec{q}_2,s\rangle \langle \vec{q}_2,s|\,\mathcal{J}_\mu(x_0)\,|\vec{q}_1,s'\rangle
$$

$$
\langle \vec{q}_1,s'|\,\bar{\chi}_\beta(x_0)\,|0\rangle
$$

$$
= N^2\sum_{\vec{q}_2,s}\sum_{\vec{q}_1,s'} \delta(\vec{p}-\vec{q}_2)\delta(\vec{p}\,'-\vec{p}+\vec{q}_2-\vec{q}_1) e^{i(\vec{p}\,'-\vec{q}_1)\cdot x_0} e^{-E_{q_2}(t_2-t_1)} e^{-E_{q_1}(t_1-t_0)}
$$

$$
\langle 0|\,\chi_\alpha(x_0)\,|n_2,\vec{q}_2,s\rangle \langle \vec{q}_2,s|\,\mathcal{J}_\mu(x_0)\,|\vec{q}_1,s'\rangle \langle \vec{q}_1,s'|\,\bar{\chi}_\beta(x_0)\,|0\rangle
$$

$$
= N^2\sum_{s,s'} e^{-E_{\vec{p}}(t_2-t_1)} e^{-E_{\vec{p}\,'}(t_1-t_0)}
$$

$$
\langle 0|\,\chi_\alpha(x_0)\,|\vec{p},s\rangle \langle \vec{p},s|\,\mathcal{J}_\mu(x_0)\,|n_1,\vec{p}\,',s'\rangle \langle \vec{p}\,',s'|\,\bar{\chi}_\beta(x_0)\,|0\rangle
$$

$$
(4.21)
$$

Inserting parity explicitly,

$$
\begin{aligned}
G_{\alpha\beta;N\mathcal{J}_\mu N}\ (t_2,t_1,\vec{p},\vec{p}') = {} & N^2 \sum_{s,s'} e^{-E^+_{p'}(t_1-t_0)} e^{-E^+_p(t_2-t_1)} \langle 0|\,\chi_\alpha(x_0)\,|p,s,+\rangle \\
& \langle p,s,+|\,\mathcal{J}_\mu(x_0)\,|p',s',+\rangle\,\langle p',s',+|\,\bar{\chi}_\beta(x_0)\,|0\rangle \\
& +N^2 \sum_{s,s'} e^{-E^-_{p'}(t_1-t_0)} e^{-E^+_p(t_2-t_1)} \langle 0|\,\chi_\alpha(x_0)\,|p,s,+\rangle \\
& \langle p,s,+|\,\mathcal{J}_\mu(x_0)\,|p',s',-\rangle\,\langle p',s',-|\,\bar{\chi}_\beta(x_0)\,|0\rangle \\
& +N^2 \sum_{s,s'} e^{-E^+_{p'}(t_1-t_0)} e^{-E^-_p(t_2-t_1)} \langle 0|\,\chi_\alpha(x_0)\,|p,s,-\rangle \\
& \langle p,s,-|\,\mathcal{J}_\mu(x_0)\,|p',s',+\rangle\,\langle p',s',+|\,\bar{\chi}_\beta(x_0)\,|0\rangle \\
& +N^2 \sum_{s,s'} e^{-E^-_{p'}(t_1-t_0)} e^{-E^-_p(t_2-t_1)} \langle 0|\,\chi_\alpha(x_0)\,|p,s,-\rangle \\
& \langle p,s,-|\,\mathcal{J}_\mu(x_0)\,|p',s',-\rangle\,\langle p',s',-|\,\bar{\chi}_\beta(x_0)\,|0\rangle
\end{aligned}
$$

$$(4.22)$$

Using, Eqs. (8.37) - (8.43),

$$
\begin{aligned}
G_{\alpha\beta;N\mathcal{J}_\mu N}\ (t_2,t_1,\vec{p},\vec{p}') = {} & a^6 \sum_{s,s'} e^{-E^+_{p'}(t_1-t_0)} e^{-E^+_p(t_2-t_1)} \phi^+(p)\bar{\phi}^+(p')\frac{m^+ m^+}{E^+_p E^+_{p'}} \\
& u_\alpha(p,s,+)\bar{u}_\eta(p,s,+)\big(\mathcal{O}^{+,+}_\mu\big)_{\eta\rho} u_\rho(p',s',-)\bar{u}_\beta(p',s',+) \\
& +a^6 \sum_{s,s'} e^{-E^-_{p'}(t_1-t_0)} e^{-E^+_p(t_2-t_1)} \phi^+(p)\bar{\phi}^-(p')\frac{m^+ m^-}{E^+_p E^-_{p'}} \\
& u_\alpha(p,s,+)\bar{u}_\eta(p,s,+)\big(\mathcal{O}^{+,-}_\mu\big)_{\eta\rho} u_\rho(p',s',-)(\bar{u}\gamma_5)_\beta(p',s',-) \\
& +a^6 \sum_{s,s'} e^{-E^+_{p'}(t_1-t_0)} e^{-E^-_p(t_2-t_1)} \phi^-(p')\bar{\phi}^+(p')\frac{m^- m^+}{E^-_p E^+_{p'}} \\
& (\gamma_5 u)_\alpha(p,s,-)\bar{u}_\eta(p,s,-)\big(\mathcal{O}^{+,-}_\mu\big)_{\eta\rho} u_\rho(p',s',+)\bar{u}_\beta(p',s',+) \\
& +a^6 \sum_{s,s'} e^{-E^-_{p'}(t_1-t_0)} e^{-E^-_p(t_2-t_1)} \phi^-(p)\bar{\phi}^-(p')\frac{m^- m^-}{E^-_p E^-_{p'}} \\
& (\gamma_5 u)_\alpha(p,s,-)\bar{u}_\eta(p,s,-)\big(\mathcal{O}^{-,-}_\mu\big)_{\eta\rho} u_\rho(p',s',-)(\bar{u}\gamma_5)_\beta(p',s',-)
\end{aligned}
$$

$$(4.23)$$

Using techniques to eliminate negative parity states shown in Eqs. (8.44), and

using simplified notation in Eq. (4.26), we obtain a simpler version of Eq. (4.23):

$$G_{\alpha\beta;NJ_\mu N}\ (t_2,t_1,\vec{p},\vec{p}',\Gamma) = \left(\frac{1+\gamma_4}{2}\right)_{\alpha\rho}\left(\frac{-i\not{p}+m}{2m}\right)_{\rho\eta}$$

$$G_{\eta\omega;NJ_\mu N}(t_2,t_1,\vec{p},\vec{p}',\mu)\left(\frac{-i\not{p}+m}{2m}\right)_{\omega\kappa}\left(\frac{1+\gamma_4}{2}\right)_{\kappa\beta}$$

$$(4.24)$$

Only the positive-parity combination will survive:

$$G_{\alpha\beta;NJ_\mu N}\quad (t_2,t_1,\vec{p},\vec{p}',\Gamma) = a^6\sum_{s,s'}e^{-E_{p'}(t_1-t_0)}e^{-E_p(t_2-t_1)}\phi(p')\bar{\phi}(p)$$

$$\frac{m^2}{E_p E_{p'}}\left[\left(\frac{1+\gamma_4}{2}\right)u(p,s)\bar{u}(p,s)\mathcal{O}_\mu u(p',s')\bar{u}(p',s')\left(\frac{1+\gamma_4}{2}\right)\right]_{\alpha\beta}$$

$$= \ a^6 e^{-E_{p'}(t_1-t_0)}e^{-E_p(t_2-t_1)}\phi(p')\bar{\phi}(p)\frac{m^2}{E_p E_{p'}}\left(\frac{1+\gamma_4}{2}\right)_{\alpha\rho}$$

$$\left(\frac{-i\gamma\cdot p+m}{2m}\right)_{\rho\eta}(\mathcal{O}_{\eta\omega})_\mu\left(\frac{-i\gamma\cdot p'+m}{2m}\right)_{\omega\kappa}\left(\frac{1+\gamma_4}{2}\right)_{\kappa\beta}$$

$$(4.25)$$

Taking the trace,

$$G_{\alpha\beta;NJ_\mu N}(t_2,t_1,\vec{p},\vec{p}',\Gamma) \ = \ \Gamma_{\alpha\beta}G_{\alpha\beta;NJ_\mu N}(t_2,t_1,\vec{p},\vec{p}',\mu)$$

$$= \ a^6\phi(p)\bar{\phi}(p')\frac{m^2}{E_p E_{p'}}\text{Tr}\left[\Gamma\begin{pmatrix}\mathbb{1} & 0 \\ 0 & 0\end{pmatrix}\right.$$

$$\left.\left(\frac{-i\gamma\cdot p+m}{2m}\right)\mathcal{O}_\mu\left(\frac{-i\gamma\cdot p'+m}{2m}\right)\begin{pmatrix}\mathbb{1} & 0 \\ 0 & 0\end{pmatrix}\right]$$

$$= \ a^6\frac{\phi(p)\bar{\phi}(p')}{4E_p E_{p'}}e^{-E_{p'}(t_1-t_0)}e^{-E_p(t_2-t_1)}$$

$$\text{Tr}\left[(-i\gamma\cdot p+m)\mathcal{O}_\mu(-i\gamma\cdot p'+m)\right]$$

$$(4.26)$$

Eq. (4.26) is the general expression for a nucleon three-point correlation function. One can now choose proper projection operators Γ and currents $\mathcal{O}_\mu$ to calculate nucleon electric and magnetic form factors.

4.3 Electromagnetic Form Factors Calculation on the Lattice

Nucleon electromagnetic form factors are functions of only one kinematical variable which represents the internal structure of the nucleon. From Lorentz symmetry and gauge invariance, $\mathcal{O}_\mu$ can be written as,

$$\mathcal{O}_\mu = \left[\gamma_\mu F_1(-q^2) + \frac{\sigma_{\mu\nu} q_\nu}{2m} F_2(-q^2) \right]. \tag{4.27}$$

where F_1 and F_2 are Dirac (spin-conserving) and Pauli (spin-flip) form factors, respectively and m is the nucleon mass. The normalization of F_1 and F_2 are determined by the charge and magnetic moment of the nucleon and these static properties can be measured in a low-energy electron-nucleon scattering experiment. $F_1(0) = 1$ for proton and 0 for neutron from current conservation, and $F_2(0)$ is a measure of nucleon anomalous magnetic moments. These are related to the electric and magnetic Sachs form factors by

$$
\begin{aligned}
G_E(Q^2) &= F_1(Q^2) - \frac{Q^2}{4m^2} F_2(Q^2) \\
G_M(Q^2) &= F_1(Q^2) + F_2(Q^2)
\end{aligned}
\tag{4.28}
$$

where in the spacelike region $Q^2 = -q^2$. Form factors enter in the expression of electromagnetic current. Lattice QCD successfully reproduces the static properties such as hadron masses and magnetic moments, etc. Therefore, one expects Lattice QCD would also describe the dynamics of the charge and magnetic distributions of the nucleon, i.e. electromagnetic form factors.

4.4 Electric Form Factor Calculation

To calculate electric form factor, one has to take $\mu = 4$ and $\Gamma = \Gamma_4$ in Eq. (4.26).

$$\Gamma_4 = \frac{1 + \gamma_4}{2} = \begin{pmatrix} \mathbb{1} & 0 \\ 0 & 0 \end{pmatrix} \tag{4.29}$$

Now, we simply the terms and perform matrix matrix multiplications step-by-step in the generalized three-point function expression (4.26) with proper choice of current operator to obtain nucleon electric form factor. We start with writing matrix form of the term $(-i\gamma \cdot p + m)$:

$$
\begin{aligned}
-i\gamma \cdot p + m &= -i(\gamma_4 p_4 + \vec{\gamma} \cdot \vec{p}) + m \\
&= -i\left[\begin{pmatrix} \mathbb{1} & 0 \\ 0 & -\mathbb{1} \end{pmatrix}(iE_p) + \begin{pmatrix} 0 & -i\vec{\sigma} \\ i\vec{\sigma} & 0 \end{pmatrix} \cdot \vec{p}\right] + \begin{pmatrix} m & 0 \\ 0 & m \end{pmatrix} \\
&= E_p\begin{pmatrix} \mathbb{1} & 0 \\ 0 & -\mathbb{1} \end{pmatrix} + \begin{pmatrix} 0 & -\vec{\sigma} \\ \vec{\sigma} & 0 \end{pmatrix} \cdot \vec{p} + \begin{pmatrix} m & 0 \\ 0 & m \end{pmatrix} \\
&= \begin{pmatrix} E_p & -\vec{\sigma} \cdot \vec{p} \\ \vec{\sigma} \cdot \vec{p} & -E_p \end{pmatrix} + \begin{pmatrix} m & 0 \\ 0 & m \end{pmatrix} = \begin{pmatrix} E_p + m & -\vec{\sigma} \cdot \vec{p} \\ \vec{\sigma} \cdot \vec{p} & -E_p + m \end{pmatrix}
\end{aligned}
$$

$$(4.30)$$

Therefore,

$$
\frac{-i\gamma \cdot p + m}{2m} = \frac{1}{2m}\begin{pmatrix} E_p + m & -\vec{\sigma} \cdot \vec{p} \\ \vec{\sigma} \cdot \vec{p} & -E_p + m \end{pmatrix}
$$

$$(4.31)$$

and similarly,

$$
\frac{-i\gamma \cdot p' + m}{2m} = \frac{1}{2m}\begin{pmatrix} E'_p + m & -\vec{\sigma} \cdot \vec{p}' \\ \vec{\sigma} \cdot \vec{p}' & -E'_p + m \end{pmatrix}
$$

$$(4.32)$$

Now multiplying with unpolarized projection operator Γ_4

$$
\begin{aligned}
\Gamma_4(-i\gamma \cdot p + m) &= \begin{pmatrix} \mathbb{1} & 0 \\ 0 & 0 \end{pmatrix}\begin{pmatrix} E_p + m & -\vec{\sigma} \cdot \vec{p} \\ \vec{\sigma} \cdot \vec{p} & -E_p + m \end{pmatrix} \\
&= \begin{pmatrix} E_p + m & -\vec{\sigma} \cdot \vec{p} \\ 0 & 0 \end{pmatrix}
\end{aligned}
$$

$$(4.33)$$

and

$$
\begin{pmatrix} E'_p + m & -\vec{\sigma} \cdot \vec{p}' \\ \vec{\sigma} \cdot \vec{p}' & -E'_p + m \end{pmatrix}\begin{pmatrix} \mathbb{1} & 0 \\ 0 & 0 \end{pmatrix} = \begin{pmatrix} E'_p + m & 0 \\ \vec{\sigma} \cdot \vec{p}' & 0 \end{pmatrix}
$$

$$(4.34)$$

29

From Eq. (4.27),

$$\mathcal{O}_4 = F_1(-q^2)\gamma_4 + \frac{\sigma_{4\nu}q_\nu}{2m}F_2(-q^2) \tag{4.35}$$

The second term in Eq. (4.27) for $\mu = 4$ is

$$\frac{\sigma_{\mu\nu}q_\nu}{2m}F_2(-q^2) \xrightarrow{\mu=4} \frac{\sigma_{44}q_4 + \sigma_{4i}q_i}{2m}F_2(-q^2)$$
$$= \frac{\sigma_{4i}q_i}{2m}F_2(-q^2) \tag{4.36}$$

where we have used (see Appendinx 8.1.9):

$$\sigma_{4i} = \begin{pmatrix} 0 & -\sigma_i \\ -\sigma_i & 0 \end{pmatrix}$$

$$\sigma_{i4} = \begin{pmatrix} 0 & \sigma_i \\ \sigma_i & 0 \end{pmatrix}$$

$$\sigma_{ij} = \epsilon_{ijk}\begin{pmatrix} \sigma_k & 0 \\ 0 & \sigma_k \end{pmatrix}$$

$$\tag{4.37}$$

Therefore,

$$\mathcal{O}_4 = \begin{pmatrix} F_1(-q^2) & -\frac{\sigma_i q_i}{2m}F_2(-q^2) \\ -\frac{\sigma_i q_i}{2m}F_2(-q^2) & -F_1(-q^2) \end{pmatrix}$$

$$\equiv \begin{pmatrix} a_{00} & a_{01} \\ a_{10} & a_{11} \end{pmatrix} \tag{4.38}$$

Now,

$$
\begin{pmatrix} E_p + m & -\vec{\sigma} \cdot \vec{p} \\ 0 & 0 \end{pmatrix} \begin{pmatrix} a_{00} & a_{01} \\ a_{10} & a_{11} \end{pmatrix}
$$

$$
= \begin{pmatrix} (E_p + m)a_{00} - a_{10}(\vec{\sigma} \cdot \vec{p}) & a_{01}(E_p + m) - a_{11}\vec{\sigma} \cdot \vec{p} \\ 0 & 0 \end{pmatrix}
$$

$$
\equiv \begin{pmatrix} b_{00} & b_{01} \\ b_{10} & b_{11} \end{pmatrix} \tag{4.39}
$$

Then

$$
\begin{pmatrix} b_{00} & b_{01} \\ b_{10} & b_{11} \end{pmatrix} \begin{pmatrix} E_{p'} + m & 0 \\ \vec{\sigma} \cdot \vec{p}' & 0 \end{pmatrix}
$$

$$
= \begin{pmatrix} b_{00}(E_{p'} + m) + b_{01}(\vec{\sigma} \cdot \vec{p}') & 0 \\ b_{10}(E_{p'} + m) + b_{11}(\vec{\sigma} \cdot \vec{p}') & 0 \end{pmatrix} \tag{4.40}
$$

Therefore, for $\mu = 4$,

$$
\begin{aligned}
G_{N\mathcal{J}_4N}(t_2, t_1, \vec{p}, \vec{p}', \Gamma) &= a^6 \frac{\phi(p)\bar{\phi}(p')}{4E_p E_{p'}} e^{-E_{p'}(t_1 - t_0)} e^{-E_p(t_2 - t_1)} \\
&\quad \mathrm{Tr} \begin{pmatrix} b_{00}(E_{p'} + m) + b_{01}(\vec{\sigma} \cdot \vec{p}') & 0 \\ b_{10}(E_{p'} + m) + b_{11}(\vec{\sigma} \cdot \vec{p}') & 0 \end{pmatrix} \\
&\equiv a^6 \frac{\phi(p)\bar{\phi}(p')}{4E_p E_{p'}} e^{-E_{p'}(t_1 - t_0)} e^{-E_p(t_2 - t_1)} \mathrm{Tr}(\mathbb{B}) \tag{4.41}
\end{aligned}
$$

Now,

$$
\begin{aligned}
\mathrm{Tr}(\mathbb{B}) &= \mathrm{Tr}[b_{00}(E_{p'}+m)+b_{01}(\vec{\sigma}\cdot\vec{p}')]\\
&= \mathrm{Tr}\Big[\big((E_p+m)a_{00}-a_{10}(\vec{\sigma}\cdot\vec{p})\big)(E_{p'}+m)\\
&\quad +\big(a_{01}(E_p+m)-a_{11}(\vec{\sigma}\cdot\vec{p})\big)(\vec{\sigma}\cdot\vec{p}')\Big]\\
&= \mathrm{Tr}\Big[\big((E_p+m)F_1+\frac{\sigma_i q_i}{2m}F_2(\vec{\sigma}\cdot\vec{p})\big)(E_{p'}+m)\\
&\quad +\big(\frac{-\sigma_i q_i}{2m}F_2(E_p+m)+F_1(\vec{\sigma}\cdot\vec{p})\big)(\vec{\sigma}\cdot\vec{p}')\Big]\\
&= \mathrm{Tr}\Big[(E_p+m)F_1(E_{p'}+m)+\frac{\sigma_i q_i}{2m}F_2(\vec{\sigma}\cdot\vec{p})(E_{p'}+m)\\
&\quad -\frac{\sigma_i q_i}{2m}F_2(E_p+m)(\vec{\sigma}\cdot\vec{p}')+F_1(\vec{\sigma}\cdot\vec{p})(\vec{\sigma}\cdot\vec{p}')\Big] \qquad (4.42)
\end{aligned}
$$

For final particle at rest, i.e. $\vec{p}=0$, from Eq. (4.42),

$$
\begin{aligned}
\mathrm{Tr}(\mathbb{B}) &= \mathrm{Tr}\Big[2mF_1(E_{p'}+m)-\frac{\sigma_i q_i}{2m}F_2(2m)(\vec{\sigma}\vec{p}')\Big]\\
&= 4mF_1(E_{p'}+m)-F_2 q_i\,\mathrm{Tr}[\sigma_i\sigma_j p'_j]\\
&= 4mF_1(E_{p'}+m)+F_2 p'_i p'_j\,\mathrm{Tr}[\sigma_i\sigma_j]\\
&= 4mF_1(E_{p'}+m)+F_2 p'_i p'_j\,\mathrm{Tr}[\delta_{ij}+i\epsilon_{ijk}\sigma_k]\\
&= 4mF_1(E_{p'}+m)+2F_2 p'_j p'_j\\
&= 4mF_1(E_{p'}+m)+2F_2(E_{p'}^2-m^2)\\
&= 4mF_1(E_{p'}+m)+2F_2(E_{p'}+m)(E_{p'}-m)\\
&= (E_{p'}+m)4m(F_1+\frac{F_2}{2m}\frac{q^2}{2m}) \quad \text{(using Eq. (8.48))}\\
&= 4m(E_{p'}+m)(F_1+\frac{q^2}{4m^2}F_2)\\
&\equiv 4m(E_{p'}+m)G_E \qquad (4.43)
\end{aligned}
$$

where, the Sachs electric form factor is defined as

$$
G_E(-q^2)\equiv F_1(-q^2)+\frac{q^2}{4m^2}F_2(-q^2) \qquad (4.44)
$$

32

Therefore,

$$
\begin{aligned}
G_{N\mathcal{J}_4 N}(t_2, t_1, \vec{p}, \vec{p}', \Gamma) &= a^6 \frac{\phi(p)\bar{\phi}(p')}{4E_p E_{p'}} e^{-E_{p'}(t_1 - t_0)} e^{-E_p(t_2 - t_1)} \\
&\quad 4m(E_{p'} + m)(F_1 + \frac{q^2}{4m^2}F_2) \\
&\equiv a^6 \frac{\phi(p)\bar{\phi}(p')}{4E_p E_{p'}} e^{-E_{p'}(t_1 - t_0)} e^{-E_p(t_2 - t_1)} 4m(E_{p'} + m)G_E
\end{aligned}
$$

(4.45)

One can derive similar expression for the special case, when the source momentum $\vec{p}' = 0$.

4.5 Magnetic Form Factor Calculation

Magnetic form factor can be obtained with $\mu = i$, and $\Gamma = \Gamma_k$ where $i, k = 1, 2, 3$. Γ_k is the polarized projection operator defined in Appendix Eq. (8.4). Then from Eq. (4.26),

$$
\mathcal{O}_i = F_1(-q^2)\gamma_i + \sigma_{i4}q_\nu \frac{F_2(-q^2)}{2m}
$$

(4.46)

Now, the first term in Eq. (4.46)

$$
F_1(-q^2)\gamma_i = \begin{pmatrix} 0 & -iF_1\sigma_i \\ iF_1\sigma_i & 0 \end{pmatrix}
$$

(4.47)

and the second term in Eq. (4.46) is

$$
\begin{aligned}
\frac{F_2(-q^2)\sigma_{i\nu}q_\nu}{2m} &= \frac{F_2}{2m}(\sigma_{i4}q_4 + \sigma_{ij}q_j) \\
&= \frac{F_2}{2m}\left[\begin{pmatrix} 0 & \sigma_i q_4 \\ \sigma_i q_4 & 0 \end{pmatrix} + \begin{pmatrix} \epsilon_{ijk}\sigma_k q_j & 0 \\ 0 & \epsilon_{ijk}\sigma_k q_j \end{pmatrix} \right] \\
&= \frac{F_2}{2m}\begin{pmatrix} \epsilon_{ijk}\sigma_k q_j & i\sigma_i E_q \\ i\sigma_i E_q & \epsilon_{ijk}\sigma_k q_j \end{pmatrix}
\end{aligned}
$$

(4.48)

33

Therefore,

$$F_1\gamma_i \;+\; \sigma_{i\nu}q_\nu\frac{F_2}{2m}$$

$$= \begin{pmatrix} \frac{F_2}{2m}\epsilon_{ijk}\sigma_k q_j & -iF_1\sigma_i + i\frac{F_2}{2m}\sigma_i E_q \\[2mm] iF_1\sigma_i + i\frac{F_2}{2m}\sigma_i E_q & \frac{F_2}{2m}\epsilon_{ijk}\sigma_k q_j \end{pmatrix}$$

$$\equiv \begin{pmatrix} c_{00} & c_{01} \\[2mm] c_{10} & c_{11} \end{pmatrix} \tag{4.49}$$

The polarized projection operator,

$$\Gamma_k = \frac{1+\gamma_4}{2}\gamma_k\gamma_5 = \begin{pmatrix} \sigma_k & 0 \\[2mm] 0 & 0 \end{pmatrix} \tag{4.50}$$

Then

$$\begin{pmatrix} \sigma_k & 0 \\[2mm] 0 & 0 \end{pmatrix} \begin{pmatrix} E_p + m & -\vec{\sigma}\cdot\vec{p} \\[2mm] \vec{\sigma}\cdot\vec{p} & -E_p + m \end{pmatrix} = \begin{pmatrix} \sigma_k(E_p+m) & \sigma_k(-\vec{\sigma}\cdot\vec{p}) \\[2mm] 0 & 0 \end{pmatrix} \tag{4.51}$$

and

$$\begin{pmatrix} E_{p'} + m & -\vec{\sigma}\cdot\vec{p}\,' \\[2mm] \vec{\sigma}\cdot\vec{p}\,' & -E_{p'} + m \end{pmatrix} \begin{pmatrix} \mathbb{1} & 0 \\[2mm] 0 & 0 \end{pmatrix} = \begin{pmatrix} E_{p'} + m & 0 \\[2mm] \vec{\sigma}\cdot\vec{p}\,' & 0 \end{pmatrix} \tag{4.52}$$

Therefore,

$$\begin{pmatrix} \sigma_k(E_p+m) & \sigma_k(-\vec{\sigma}\cdot\vec{p}) \\[2mm] 0 & 0 \end{pmatrix} \begin{pmatrix} c_{00} & c_{01} \\[2mm] c_{10} & c_{11} \end{pmatrix}$$

$$= \begin{pmatrix} \sigma_k(E_p+m)c_{00} + \sigma_k(-\vec{\sigma}\cdot\vec{p})c_{10} & \sigma_k(E_p+m)c_{01} + \sigma_k(-\vec{\sigma}\cdot\vec{p})c_{11} \\[2mm] 0 & 0 \end{pmatrix}$$

$$\equiv \begin{pmatrix} d_{00} & d_{01} \\[2mm] d_{10} & d_{11} \end{pmatrix} \tag{4.53}$$

Thus

$$
\begin{pmatrix} d_{00} & d_{01} \\ d_{10} & d_{11} \end{pmatrix} \begin{pmatrix} E_{p'} + m & 0 \\ \vec{\sigma} \cdot \vec{p}' & 0 \end{pmatrix} = \begin{pmatrix} (E_{p'} + m)d_{00} + (\vec{\sigma} \cdot \vec{p}')d_{01} & 0 \\ 0 & 0 \end{pmatrix}
$$

$$
\equiv \ \mathbb{D} \tag{4.54}
$$

Now,

$$
\begin{aligned}
\mathrm{Tr}(\mathbb{D}) \ &= \ \mathrm{Tr}[(E_{p'} + m)d_{00} + (\vec{\sigma} \cdot \vec{p}')d_{01}] \\
&= \ \mathrm{Tr}[(E_{p'} + m)\big(\sigma_k(E_p + m)c_{00} + \sigma_k(-\vec{\sigma} \cdot \vec{p})c_{10}\big) \\
&\quad + (\vec{\sigma} \cdot \vec{p}')\big(\sigma_k(E_p + m)c_{01} + \sigma_k(-\vec{\sigma} \cdot \vec{p})c_{11}\big)] \\
&= \ \mathrm{Tr}[(E_{p'} + m)\sigma_k(E_p + m)c_{00} + (E_{p'} + m)\sigma_k(-\vec{\sigma} \cdot \vec{p})c_{10} \\
&\quad + (\vec{\sigma} \cdot \vec{p}')\sigma_k(E_p + m)c_{01} + (\vec{\sigma} \cdot \vec{p}')\sigma_k(-\vec{\sigma} \cdot \vec{p})c_{11}] \\
&= \ \mathrm{Tr}\Big[(E_{p'} + m)\sigma_k(E_p + m)\frac{F_2}{2m}\epsilon_{ijl}\sigma_l q_j - (E_{p'} + m)\sigma_k(\vec{\sigma} \cdot \vec{p}) \\
&\quad \big(iF_1\sigma_i + i\frac{F_2}{2m}\sigma_i E_q\big) + (\vec{\sigma} \cdot \vec{p}')\sigma_k(E_p + m)\big(-iF_1\sigma_i \\
&\quad + i\frac{F_2}{2m}\sigma_i E_q\big) - (\vec{\sigma} \cdot \vec{p}')\sigma_k(\vec{\sigma} \cdot \vec{p})\frac{F_2}{2m}\epsilon_{ijl}\sigma_l q_j\Big] \tag{4.55}
\end{aligned}
$$

As a special case, for the final state at rest,

$$
\begin{aligned}
\mathrm{Tr}(\mathbb{D}) \;=\;& \mathrm{Tr}\Big[(E_{p'}+m)\sigma_k(2m)\frac{F_2}{2m}\epsilon_{ijl}\sigma_l q_j + (\vec{\sigma}\cdot\vec{p}')\vec{\sigma}_k(2m) \\
& \Big(-iF_1\sigma_i + \frac{iF_2}{2m}\sigma_i(m-E_{p'})\Big)\Big] \\
\;=\;& \mathrm{Tr}\Big[(E_{p'}+m)\sigma_k 2m\frac{F_2}{2m}\epsilon_{ijl}\sigma_l q_j - i(\vec{\sigma}\cdot\vec{p}')\sigma_k 2mF_1\sigma_i \\
& + (\vec{\sigma}\cdot\vec{p}')\sigma_k 2m\frac{iF_2}{2m}\sigma_i(m-E_{p'})\Big] \\
\;=\;& -iF_1 p'_l 2m\mathrm{Tr}[\sigma_k\sigma_i\sigma_l] + (E_{p'}+m)F_2\epsilon_{ijl}q_j\mathrm{Tr}[\sigma_k\sigma_l] \\
& + iF_2(m-E_{p'})p'_l\mathrm{Tr}[\sigma_k\sigma_i\sigma_l] \\
\;=\;& -iF_1 p'_l 2m\mathrm{Tr}[(\delta_{ki}+i\epsilon_{kim}\sigma_m)\sigma_l] + (E_{p'}+m)F_2\epsilon_{ijl}q_j\mathrm{Tr}[\delta_{kl}+i\epsilon_{klm}\sigma_m] \\
& + iF_2(m-E_{p'})p'_l\mathrm{Tr}[(\delta_{ki}+i\epsilon_{kim}\sigma_m)\sigma_l] \\
\;=\;& -i^2\epsilon_{kim}F_1 p'_l 2m\mathrm{Tr}[\sigma_m\sigma_l] + 2(E_{p'}+m)F_2\epsilon_{ijl}q_j + i^2 F_2(m-E_{p'})p'_l\epsilon_{kim}\mathrm{Tr}[\sigma_m\sigma_l] \\
\;=\;& \epsilon_{kim}F_1 p'_l 2m\mathrm{Tr}[\delta_{ml}+i\epsilon_{mlr}\sigma_r] + 2(E_{p'}+m)F_2\epsilon_{ijl}q_j \\
& - F_2(m-E_{p'})p'_l\epsilon_{kim}\mathrm{Tr}[\delta_{ml}+i\epsilon_{mlr}\sigma_r] \\
\;=\;& 4m\epsilon_{kil}F_1 p'_l + 2(E_{p'}+m)F_2\epsilon_{ijl}q_j - 4F_2(m-E_{p'})p'_m\epsilon_{kim} \\
\;=\;& -4\epsilon_{ikl}F_1 p'_l m + 2F_2\big((E_{p'}+m)\epsilon_{ijl}q_j - (m-E_{p'})\epsilon_{kim}p'_m\big) \\
\;=\;& 4mF_1\epsilon_{ijk}q_k + 2F_2\big((E_{p'}+m)\epsilon_{ijl}q_j + (m-E_{p'})\epsilon_{kim}q_m\big) \\
\;=\;& 4mF_1\epsilon_{ijk}q_k + 4mF_2\epsilon_{ijk}q_k \\
\;=\;& 4m(F_1+F_1)\epsilon_{ijk}q_k \\
\;\equiv\;& 4mG_M\epsilon_{ijk}q_k
\end{aligned}
\tag{4.56}
$$

where the magnetic Sachs form factor has been defined as

$$
G_M(-q^2) \equiv F_1(-q^2) + F_2(-q^2)
\tag{4.57}
$$

Therefore,

$$
\begin{aligned}
G_{N\mathcal{J}_i N}(t_2, t_1, \vec{p}, \vec{p}', \Gamma) &= a^6 \frac{\phi(p)\bar{\phi}(p')}{4E_p E_{p'}} e^{-E_{p'}(t_1-t_0)} e^{-E_p(t_2-t_1)} \\
&\quad 4m(E_{p'}+m)(F_1 + \frac{q^2}{4m^2}F_2) \\
&\equiv a^6 \frac{\phi(p)\bar{\phi}(p')}{4E_p E_{p'}} e^{-E_{p'}(t_1-t_0)} e^{-E_p(t_2-t_1)} 4m G_M \epsilon_{ijk} q_k
\end{aligned}
$$

(4.58)

One can derive similar expression for the special case, when the source momentum $\vec{p}' = 0$.

4.6   Extraction of Ground-State Matrix Element

One can extract the ground-state matrix elements by taking a ratio of three-point to two-point correlation functions. We look for a plateau in the asymptotic Euclidean time behavior of the ratio. The ratio can be written as [30]

$$
\begin{aligned}
R(t_2, t_1, \vec{p}, \vec{p}', \Gamma; \mu) &= \frac{\langle G_{N\mathcal{J}_\mu}N(t_2, t_1; \vec{p}', \vec{p}; \Gamma)\rangle}{\langle G_{NN}(t_2, \vec{p}'; \Gamma_4)\rangle} \\
&= \sqrt{\frac{\langle G_{NN}(t_2-t_1+t_0, \vec{p}; \Gamma_4)\rangle \langle G_{NN}(t_1, \vec{p}'; \Gamma_4)\rangle \langle G_{NN}(t_2, \vec{p}'; \Gamma_4)\rangle}{\langle G_{NN}(t_2-t_1+t_0, \vec{p}'; \Gamma_4)\rangle \langle G_{NN}(t_1, \vec{p}; \Gamma_4)\rangle \langle G_{NN}(t_2, \vec{p}; \Gamma_4)\rangle}}
\end{aligned}
$$

(4.59)

This ratio method exactly cancels the time dependence and weight factors (ϕ). Considering only time-dependent and normalization factors in Eq. (4.59), from the factor outside the square-root,

$$
\begin{aligned}
R &= e^{-E_p(t_1-t_0)} e^{-E_{p'}(t_0-t_1)} \sqrt{e^{2E_p(t_1-t_0)} e^{-2E_{p'}}(t_1-t_0)} \\
&= 1
\end{aligned}
$$

(4.60)

However, due to computational cost, we took the following three-point to two-point ratio in our numerical calculation. In our calculation, the nucleon grid-smeared source is at rest, ($\vec{p}' = 0$), and the source temporal position is $t_0 = 0$. We define the three-

point to two-point ratio as,

$$R_\mu(\vec{q}, t_2, t_1) = \frac{\text{Tr}[\Gamma_m G_{NJ_\mu N}(\vec{q}, t_2, t_1)]}{\text{Tr}[\Gamma_e G_{NN}(\vec{0}, t_2)]} e^{(E_q - m) \cdot (t_2 - t_1)} \frac{2E_q}{E_q + m}.$$

(4.61)

Then the magnetic form factor can be calculated as

$$
\begin{aligned}
R_i(\vec{q}, t_2, t_1) &= \frac{a^6 \frac{\phi(p)\bar{\phi}(0)}{4E_q m} e^{-E_q(t_2-t_1)} e^{-mt_1} \left(4m\epsilon_{ijk}q_k G_M\right)}{a^6 \phi(0)\bar{\phi}(0) 2e^{-mt_2}} e^{-(E_q-m)(t_2-t_1)} \frac{2E_q}{E_q+m} \\
&= \frac{\phi(p)}{\phi(0)} \frac{\epsilon_{ijk}q_k}{E_q+m} G_M \qquad (\text{for } \vec{p}' = 0, \ \vec{p} = \vec{q}), \\
R_i(\vec{q}, t_2, t_1) &= \frac{\phi(p)}{\phi(0)} G_E \qquad (\text{for } \vec{p}' = 0, \ \vec{p} = \vec{q})
\end{aligned}
$$

(4.62)

We will see that the effect of the ratio of these two wavefunction overlap factors will not have any significant effect in our calculation in comparison to the size of the statistical and systematic uncertainties. We will present more discussion on this in the subsequent sections.

Chapter 5 Strange Quark Electromagnetic Form Factors

5.1 Abstract

We present a lattice QCD calculation of the strange quark contribution to the nucleon's magnetic moment and charge radius. This analysis presents the first direct determination of strange electromagnetic form factors including at the physical pion mass. We perform a model-independent extraction of the strange magnetic moment and the strange charge radius from the electromagnetic form factors in the momentum transfer range of $0.051\,\text{GeV}^2 \lesssim Q^2 \lesssim 1.31\,\text{GeV}^2$. The finite lattice spacing and finite volume corrections are included in a global fit with 24 valence quark masses on four lattices with different lattice spacings, different volumes, and four sea quark masses including one at the physical pion mass. We obtain the strange magnetic moment $G_M^s(0) = -0.064(14)(09)\,\mu_N$. The four-sigma precision in statistics is achieved partly due to low-mode averaging of the quark loop and low-mode substitution to improve the statistics of the nucleon propagator. We also obtain the strange charge radius $\langle r_s^2 \rangle_E = -0.0043(16)(14)\ \text{fm}^2$. From the fit parameters of the model-independent z-expansion, we also present strange quark electric and magnetic form factors in the momentum transfer region of $0\,\text{GeV}^2 \leq Q^2 \leq 0.5\,\text{GeV}^2$.

5.2 Introduction

In the non-relativistic constituent quark model, a proton is composed of two up and one down quarks. Unlike in the real QCD dynamics, where the quarks interact strongly between themselves via gluon exchange, in the constituent quark model they do not interact strongly. Although this simple quark model has been very successful in describing various nucleon properties, such as predicting the proton magnetic moment

within 3% [31] of the experimental value, results from the deep-inelastic scattering experiments indicate that nucleon sea consists of $q\bar{q}$ pairs and gluons play a very important role in describing nucleon properties. For example, almost half of the nucleon momentum is carried by the gluons which is consistent with the nature of QCD that quarks interact strongly through exchange of gluons. It is clear from the deep-inelastic experimental data that gluons play a very important role describing the QCD dynamics at low x. For example, the sharp rise of $g(x)$ in the low x-region cannot be described by the simple quark model. Since strange (s)-quarks are only present in the sea, measuring various s-quark contributions to the nucleon properties gives direct information about the nucleon sea and its nonperturbative structure.

Flavor decomposition of the sea-quarks in the nucleon is of immense importance due to their complex natures. For example, from the recent analysis of Drell-Yan data one clearly sees an excess of $\bar{d}(x)$ over $\bar{u}(x)$ in the nucleon sea. To understand the flavor content of the nucleon-sea, such as the excess of $\bar{d}(x)/\bar{u}(x)$, a lattice QCD calculation in Ref. [32] was performed using the path integral formalism of the hadronic tensor. The authors in Ref. [32] illustrated existence of two topologically distinct sources of nucleon sea - called the connected and disconnected-sea and showed that the Gottfried sum rule violation comes from the connected insertion involving quarks propagating backwards in time. In a recent lattice QCD calculation [33], the authors have discussed that the excess of $\bar{d}(x)/\bar{u}(x)$ cannot originate from the disconnected-sea since the mass difference between u and d quarks are very small to account for this large excess of $\bar{d}(x)/\bar{u}(x)$ observed in the deep-inelastic experiment and Drell-Yan process.

The excess of $\bar{d}(x)/\bar{u}(x)$ cannot be explained by simple $g \rightarrow q\bar{q}$ fluctuation in the intermediate x-values and some other nonperturbative processes are required to explain this excess. An example of such a nonperturbative process can be the virtual conversion of proton to neutron $p \rightarrow \pi^{+}n$, so that excess of $\bar{d}$ is created

relative to the abundance of $\bar{u}$. In contrast, there is no such analogous procedure to create an excess of $\bar{u}$. In this way $\bar{d}$-excess could be produced at a $x \sim \frac{m_\pi}{2m_N}$ and this is consistent with experimental observation. This type of meson-baryon fluctuation is a nonperturbative phenomenon and needs to be understood. A similar possible meson-baryon fluctuation which can produce different spatial distribution of s and $\bar{s}$ quarks in the nucleon sea is $N \to K^+\Lambda$ fluctuation. From our lattice calculation, we shall show, in Chapter 6, that the difference of spatial distribution of light-sea quarks q and $\bar{q}$ is larger than the difference of spatial distribution of s and $\bar{s}$ quarks in the nucleon. This is natural, because $K^+\Lambda$ is expected to be produced with lower probability than the πN fluctuations due to their higher masses of $K^+(u\bar{s})$ and $\Lambda(uds)$ compared to π and N, respectively. A meson-baryon configuration such as a $K^+\Lambda$ meson-baryon state will create a different radially-separated distribution of s and $\bar{s}$ quarks from the center of mass of a $K^+\Lambda$ configuration. Therefore, this nonperturbative phenomenon would lead to a small non-zero value of the strange quark electric form factor G_E^s at non-zero values of Q^2 which is a consequence of the fact that the average distribution of $\bar{s}$ is slightly farther compared to the average s-quark distribution from the center of the nucleon. Keeping in mind that $K^+(u\bar{s})$ has a smaller mass than $\Lambda(uds)$, it is expected that K^+ and thus $\bar{s}$ will occupy a larger radial distance from the center of mass of the $K^+\Lambda$ meson-baryon configuration. Such a calculation with light-front wave function has been previously done by Brodsky and Ma [34, 35] using light-cone meson-baryon fluctuation model. In Ref. [35], the author obtained $G_M^s(0) = -0.066\,\mu_N$. These meson-baryon fluctuation models can serve as a motivation for the need of a first-principles nonperturbative calculation. Thus, it is essential to check these meson-baryon fluctuation models with ab-initio calculation in lattice QCD.

In summary, the difference in the spatial distribution of s and $\bar{s}$ can have the following consequences [36]:

- $s\bar{s}$ contribution to nucleon mass,

- $s\bar{s}$ contribution to nucleon axial charge which can affect the value of Σ associated with the helicity carried by the quarks,

- Nonzero value of strange quark electric form factor G_E^s at $Q^2 > 0$,

- $s\bar{s}$ contribution to nucleon magnetic form factor and neutral weak form factors,

- Difference between parton distribution functions (PDFs) of $s(x)$ and $\bar{s}(x)$.

While the first 4 consequences are low Q^2 phenomena, one can relate the difference of $s(x)$ and $\bar{s}(x)$ PDFs to a similar Drell-Yan process of the excess of $\bar{d}(x)/\bar{u}(x)$.

Therefore, a precise and accurate measurement of strange quark electromagnetic form factors is of immense importance. For example, the one of the backgrounds in the Q_{weak} experiment arises from the $G_M^s(Q^2)$. A precise estimate of $G_M^s(Q^2)$ can lead to more precision in the estimated value of proton weak charge $Q^p = (1 - 4\sin^2\theta_W)$ in the Q_{weak} experiment. It is very important to know the value of Q^p with great precision because this will constrain the possibility of Beyond Standard Model physics.

Since the extraction of the vector strange matrix elements $\langle N|\bar{s}\gamma_\mu s|N\rangle$ was proposed in Refs. [37–39] via parity-violating $e^- - N$ scattering, the determination of strange quark contribution to the nucleon electromagnetic form factors $(G_{E,M}^s)$ at low momentum transfer has been the main goal of various experiments of the SAMPLE, HAPPEX, G0, and A4 collaborations [40–51]. The world data constrains that the strange quark magnetic moment $G_M^s(0)$ contributes less than 6% and the strange quark mean square charge radius $\langle r_s^2 \rangle_E$ contributes less than 5% to the magnetic moment and the mean-square charge radius of the proton respectively [52]. However, all these experimental results are limited by rather sizable error bars. Three different global analyses give $G_M^s(Q^2 = 0.1\,(GeV/c)^2)$, which is consistent with zero within uncertainties, and differ in sign in their central values [53–55]. However, modern ex-

perimental results favor a negative value of $G_M^s(0)$ which is consistent with previous lattice QCD calculations.

Despite tremendous theoretical efforts, *e.g.* [56–59], a detailed convincing understanding about the sign and magnitude of strange quark electromagnetic form factors is still lacking. A detailed review of these theoretical efforts can be found in [60]. The first measurement of the proton neutral weak magnetic form factor $G_M^{Z,p}$ from parity-violating asymmetry in the polarized $\vec{e} - p$ scattering experiment was performed by the SAMPLE collaboration. Performed at a momentum transfer of $Q^2 = 0.1\,\text{GeV}^2$, the neutral weak magnetic form factor was found to be $G_M^{Z,p}(0.1\,\text{GeV}^2) = 0.34(11)$ nucleon magneton (n.m.) which corresponds to a value of $G_M^s(Q^2 = 0.1\,\text{GeV}^2) = 0.23(44)$ n.m. [61]. These results were updated to obtain a value of $G_M^s(Q^2 = 0.1\,\text{GeV}^2) = 0.37(33)$ n.m. in Ref. [40]. An analysis of the SAMPLE data estimated $G_M^{Z,p}(0.1\,\text{GeV}^2) = 0.29(16)$ n.m. which corresponds to $G_M^s(Q^2 = 0.1\,\text{GeV}^2) = 0.49(65)$ n.m. [62]. A large positive value of G_M^s corresponds to a $G_M^{Z,p} < 0.40$ n.m. at $Q^2 = 0.1\,\text{GeV}^2$. To date, no individual experiment provides high precision measurements of the nucleon neutral weak form factors in a wide range of Q^2. By considering the weak axial vector form factor G_A^Z as an input, it is possible to separate the Sachs electric and magnetic form factors by combining parity-violating asymmetry measurements from the experimental data. However, because of the complexity of the experiments, rather sizable uncertainties in the value of G_A^Z and the lack of knowledge of its Q^2 behavior, the extracted value of nucleon strange electromagnetic form factors from parity-violating asymmetry data vary widely in different experiments and global fits of the experimental data as mentioned above. The level of precision of the strange quark form factor measurements is not so high at present to differentiate $G_{E,M}^s$ from zero. It is also important to note that the parity-violating asymmetry measured by the modern experiments is very precise and plays an important role in measuring hadronic properties associated with parity violations.

However, a significantly precise knowledge of $G_A^Z(Q^2)$ is required to extract $G_{E,M}^s$ and $G_{E,M}^{z,p(n)}$ from the experimental measurements of parity-violating asymmetry. As we will discuss below, although the typical electroweak radiative corrections are expected to be $\mathcal{O}(\alpha)$, the tree-level suppression of the interaction in the parity-violating $\vec{e} - p$ scattering makes the radiative corrections to G_A^Z more significant. The uncertainties in the radiative correction of G_A^Z are large and radiative corrections involving the strong interaction are not clearly known, so the extraction of $G_{E,M}^{Z,p(n)}$ from the parity-violating scattering experiments is a tremendous challenge. One anticipates that with a reliable first-principles estimate of $G_{E,M}^s$, one can also give a prediction of the neutral weak form factors of the proton and the neutron.

5.3   Formalism

Electron-proton scattering can proceed through an exchange of a virtual Z-boson or photon (γ), represented in the lowest order by the Feynman diagrams shown in FIG. 5.1. This process gives rise to a new current for the proton, called the neutral weak current. Because the neutral weak charge of light quarks and electrons are different for the left-handed and right-handed particles, parity is violated in the scattering of polarized electrons off the nucleon. The invariant amplitudes of the scattering processes shown in FIG. 5.1 can be written in terms of leptonic vector (l^μ), axial ($l^{\mu 5}$), nucleon vector (J_γ^μ), nucleon weak vector (J_Z^μ) and weak axial ($J_Z^{\mu 5}$) currents:

$$\mathcal{M}_\gamma = \frac{4\pi\alpha}{Q^2} e_i l^\mu J_\mu^\gamma, \tag{5.1}$$

$$\mathcal{M}_Z = \frac{G_F}{2\sqrt{2}} (g_V^i l^\mu + g_A^i l^{\mu 5})(J_\mu^Z + J_{\mu 5}^Z), \tag{5.2}$$

(a) Photon exchange

(b) Neutral weak Z-boson exchange
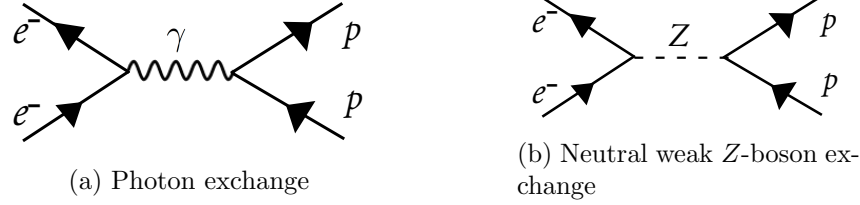
Figure 5.1: Tree level electromagnetic and weak Feynman diagrams in the $e^- - N$ scattering: (5.1a) photon (γ) exchange, (5.1b) neutral weak Z-boson exchange.

(a)

(b)
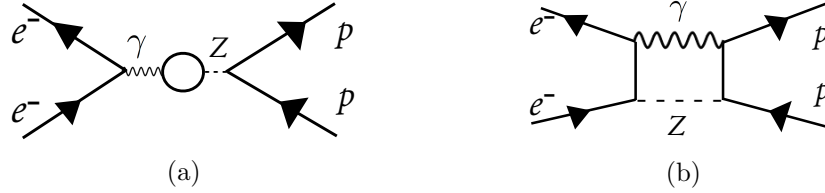
Figure 5.2: Feynman diagrams representing "one-quark" radiative corrections in the $e^- - N$ scattering: (5.2a) Vacuum polarization, (5.2b) $\gamma - Z$ box diagram.

(a)

(b)
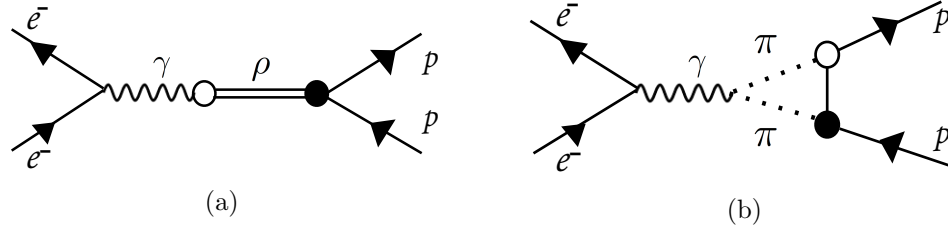
Figure 5.3: Feynman diagrams representing "many-quark" radiative corrections in the $e^- - N$ scattering. The unfilled and filled circles represent vector and axial couplings, respectively: (5.3a) Rho (ρ) meson pole, (5.3b) pion loop.

where α is the electromagnetic coupling constant, $G_F = 1.166 \times 10^{-5}$ GeV^{-2} is the Fermi constant, e_i is the electromagnetic charge of the incident electron, and $g_{V(A)}^l$ is the weak vector (axial) charge in Eqs. (5.2), (5.3) and (5.4). From Eq. (5.3), it is seen that the neutral weak boson can have both vector and axial vector interactions. Therefore the amplitude $\mathcal{M}_Z$ has both parity violating (PV) and parity conserving (PC) amplitudes:

$$\mathcal{M}_Z^{PV} = \frac{G_F}{2\sqrt{2}}(g_V^i l^\mu J_{\mu 5}^Z + g_A^i l^{\mu 5} J_\mu^Z),\tag{5.3}$$

$$\mathcal{M}_Z^{PC} = \frac{G_F}{2\sqrt{2}}(g_V^i l^\mu J_\mu^Z + g_A^i l^{\mu 5} J_{\mu 5}^Z). \tag{5.4}$$

Similar to the electromagnetic current in the nucleon, the vector component of the neutral weak current in the nucleon can be written as

$$J_\mu^Z = \bar{u}_N \left[\gamma_\mu F_1^Z(Q^2) + \frac{i\sigma_{\mu\nu}q^\nu}{2M_N} F_2^Z(Q^2) \right] u_N, \tag{5.5}$$

where u_N is the nucleon spinor, the neutral weak form factors F_1^Z and F_2^Z are analogous to the electromagnetic form factors F_1^γ and F_2^γ. The nucleon neutral weak axial current is defined as:

$$J_{\mu 5}^Z = \bar{u}_N \left[\gamma_\mu \gamma_5 G_A^Z \right] u_N \tag{5.6}$$

where G_A^Z is the neutral weak axial form factor.

Since the electroweak interaction of the gauge bosons with quarks is pointlike, the nucleon vector and axial currents and the corresponding form factors can be decomposed into a sum of quark currents, one current for each quark flavor [63]. The electromagnetic and neutral weak vector currents can be written as nucleon matrix elements of the quark current operators $\hat{J}_\mu^\gamma$ and $\hat{J}_{\mu 5}^\gamma$ as

$$\begin{aligned} J_\mu^\gamma &\equiv \langle N | \hat{J}_\mu^\gamma | N \rangle, \\ J_\mu^Z &\equiv \langle N | \hat{J}_\mu^Z | N \rangle, \\ J_{\mu 5}^Z &\equiv \langle N | \hat{J}_{\mu 5}^Z | N \rangle \end{aligned} \tag{5.7}$$

where $|N\rangle$ is a proton or neutron state and the quark current operators are given by

$$\begin{aligned} \hat{J}_\mu^\gamma &\equiv \sum_q Q_q \bar{q} \gamma_\mu q, \\ \hat{J}_\mu^Z &\equiv \sum_q g_q^V \bar{q} \gamma_\mu q, \\ \hat{J}_{\mu 5}^Z &\equiv \sum_q g_q^A \bar{q} \gamma_\mu \gamma_5 q. \end{aligned}$$

$$\tag{5.8}$$

Here the sum is over all quark flavors q and Q_q, $g_q^{V(A)}$ are the electromagnetic and neutral weak vector (axial vector) quark couplings in the Standard Model and are listed in Table (5.1) for the up, down and strange quarks.

Table 5.1: The electromagnetic, weak vector, and weak axial couplings for the up, down, and strange quarks and electron.

Quarks	Q_i	g_q^V	g_q^A
u	$\frac{2}{3}$	$\frac{1}{4} - \frac{2}{3}\sin^2\theta_W$	-1
d	$-\frac{1}{3}$	$-\frac{1}{4} + \frac{2}{3}\sin^2\theta_W$	1
s	$-\frac{1}{3}$	$-\frac{1}{4} + \frac{1}{3}\sin^2\theta_W$	1
e	-1	$-\frac{1}{4} + \sin^2\theta_W$	1

Using these couplings listed in Table (5.1), we can express the nucleon form factors as linear combinations of the quark components, $i.e.$

$$
\begin{aligned}
G_{E(M)}^{\gamma,N} &\equiv \sum_q Q_q G_{E(M)}^{q,N}, \\
G_{E(M)}^{Z,N} &\equiv \sum_q g_q^V G_{E(M)}^{q,N}, \\
G_A^{Z,N} &\equiv \sum_q g_q^A G_A^{q,N}
\end{aligned}
\tag{5.9}
$$

where $G_{E(M)}^{q,N}$ is the contribution form the quark flavor q to the nucleon electric (magnetic) form factor and $G_A^{q,N}$ is the contribution to the nucleon weak axial form factor. Now assuming that only u, d, s quarks contribute significantly to the nucleon electromagnetic and weak form factors, and using the couplings from Table (5.1) we can write the nucleon currents in terms of the quark-nucleon currents as

$$
\begin{aligned}
J_\mu^\gamma &= \langle N|\hat{J}_\mu^\gamma|N\rangle \\
&= \frac{2}{3}\langle N|\bar{u}\gamma_\mu u|N\rangle - \frac{1}{3}\langle N|\bar{d}\gamma_\mu d|N\rangle - \frac{1}{3}\langle N|\bar{s}\gamma_\mu s|N\rangle\,,
\end{aligned}
\tag{5.10}
$$

$$
\begin{aligned}
J_\mu^Z &= \langle N|\hat{J}_\mu^Z|N\rangle \\
&= \left(\frac{1}{4} - \frac{2}{3}\sin^2\theta_W\right)\langle N|\bar{u}\gamma_\mu u|N\rangle + \left(-\frac{1}{4} + \frac{1}{3}\sin^2\theta_W\right)\langle N|\bar{d}\gamma_\mu d|N\rangle \\
&\quad + \left(-\frac{1}{4} + \frac{1}{3}\sin^2\theta_W\right)\langle N|\bar{s}\gamma_\mu s|N\rangle\,.
\end{aligned}
\tag{5.11}
$$

It is important to note from Eqs. (5.10) and (5.11) that the same quark-nucleon currents $\langle N|\bar{q}\gamma_\mu q|N\rangle$ appear on the right hand side, *i.e.* the quark-nucleon currents depend only on the vector nature of the coupling and not whether the coupling is though the photon or neutral weak boson exchange in the $e^- - N$ scattering. This property along with the assumption of isospin symmetry will allow us to relate the nucleon neutral weak and strange quark form factors in the subsequent calculations. Similarly, using Eqs. (5.9), nucleon Sachs form factors can be written as

$$
G_{E,M}^{\gamma,p} = \frac{2}{3}G_{E,M}^{u,p} - \frac{1}{3}G_{E,M}^{d,p} - \frac{1}{3}G_{E,M}^{s,p},
\tag{5.12}
$$

$$
G_{E,M}^{\gamma,n} = \frac{2}{3}G_{E,M}^{u,n} - \frac{1}{3}G_{E,M}^{d,n} - \frac{1}{3}G_{E,M}^{s,n},
\tag{5.13}
$$

$$
\begin{aligned}
G_{E,M}^{Z,p} &= \left(\frac{1}{4} - \frac{2}{3}\sin^2\theta_W\right)G_{E,M}^{u,p} + \left(-\frac{1}{4} + \frac{1}{3}\sin^2\theta_W\right)G_{E,M}^{d,p} \\
&\quad + \left(-\frac{1}{4} + \frac{1}{3}\sin^2\theta_W\right)G_{E,M}^{s,p}
\end{aligned}
\tag{5.14}
$$

The charge symmetry is broken due to the mass difference of u and d quarks and electromagnetic interactions. However, this effect of symmetry breaking on the estimate of nucleon form factors is negligible compared to the uncertainties in the experimental measurements and the following lattice QCD analysis and thus can be safely ignored.

Assuming strong isospin symmetry, *i.e.* the $u(d)$-quarks in the proton have the same properties as $d(u)$ quarks in the neutron, one can write

$$G^{u,p} = G^{d,n}, \qquad G^{d,p} = G^{u,n}, \qquad \text{and} \qquad G^{s,p} = G^{s,n} = G^s, \tag{5.15}$$

and so Eq. (5.14) can be written as

$$G_{E,M}^{Z,p(n)} = \left(\frac{1}{4} - \sin^2 \theta_W\right) G_{E,M}^{\gamma,p(n)} - \frac{1}{4} G_{E,M}^{\gamma,n(p)} - \frac{1}{4} G_{E,M}^s \tag{5.16}$$

With radiative corrections, Eq. (5.16) can be written as

$$\begin{aligned} G_{E,M}^{Z,p(n)}(Q^2) &= \frac{1}{4}\bigg[(1 - 4\sin^2 \theta_W)(1 + R_V^{p(n)}) G_{E,M}^{\gamma,p(n)}(Q^2) - (1 + R_V^{n(p)}) G_{E,M}^{\gamma,n(p)}(Q^2) \\ &\quad - (1 + R_V^{(0)}) G_{E,M}^s(Q^2)\bigg], \end{aligned} \tag{5.17}$$

where the subscript $E(M)$ stands for the electric(magnetic) form factor and the superscript $p(n)$ stands for the proton(neutron). $R_V^{p(n)}$ and $R_V^{(0)}$ are radiative corrections to the vector form factors calculated in [64] and translated into the $\overline{\text{MS}}$-scheme in [63]. The updated analyses of these radiative corrections can be found in [65] and [66].

Experimentally the proton's neutral weak form factors can be measured directly through $e^- - N$ scattering. Electromagnetic scattering amplitude dominates over the neutral weak scattering amplitude. Since there is no direct way to determine whether photon exchange or neutral weak boson exchange is responsible for a given $e^- - N$ scattering event, one calculates the total scattering as

$$\sigma_{\text{total}} \propto |\mathcal{M}_\gamma + \mathcal{M}_Z|^2 \tag{5.18}$$

Since the weak force violates parity as mentioned earlier, the neutral weak scattering amplitude $\mathcal{M}_Z$ depends on the helicity of the incident electron. Therefore, the nucleon has different cross sections for the right and the left handed electrons. As a result, the cross section associated with the positive helicity electron is different from that

of the negative helicity electron. Because the spin of the electron is an axial vector and the momentum is a vector quantity, the helicity of the electrons

$$h \equiv \vec{s} \cdot \vec{k} \tag{5.19}$$

is a pseudo-scalar quantity and flips the helicity of electron beam between right and left helicity states in the elastic scattering of longitudinally polarized electron from an unpolarized proton target. Then the asymmetry of the $e^- - N$ scattering event can be written as

$$
\begin{aligned}
A_{\text{LR}} &= \frac{|\mathcal{M}_\gamma + \mathcal{M}_{Z,R}|^2 - |\mathcal{M}_\gamma + \mathcal{M}_{Z,L}|^2}{|\mathcal{M}_\gamma + \mathcal{M}_{Z,R}|^2 + |\mathcal{M}_\gamma + \mathcal{M}_{Z,L}|^2} \\
&\approx \frac{|\mathcal{M}_{Z,R}| - |\mathcal{M}_{Z,L}|}{\mathcal{M}_\gamma}
\end{aligned} \tag{5.20}
$$

where right (L) and left (L) described that there is a helicity dependence in the weak neutral amplitudes. In the last line of Eq. (5.20), we have used the fact that $|\mathcal{M}_\gamma| \gg |\mathcal{M}_Z|$, and approximately,

$$
\begin{aligned}
A_{\text{LR}} &\approx \frac{|\mathcal{M}_Z|}{|\mathcal{M}_\gamma|} \\
&\approx \frac{G_F}{e^2/q^2}
\end{aligned} \tag{5.21}
$$

which is $\sim 10^{-5}$ for $-q^2 \sim 0.5$ GeV^2. This small magnitude of $\mathcal{M}_Z$ compared to the electromagnetic amplitude makes the experimental measurements of strange quark and neutral weak form factors very challenging. However, this parity-violating amplitude is enhanced through the interference with the parity-conserving electromagnetic amplitude and enables the experimentalists to measure the weak interaction effects. It has been shown in Ref. [63] that the asymmetry can be measured in terms of the nucleon form factors as

$$A_{\text{LR}} = -\frac{G_F Q^2}{\sqrt{2}\pi\alpha} \left[\frac{\epsilon G_E^{\gamma,p} G_E^{Z,p} + \tau G_M^{\gamma,p} G_M^{Z,p} - \frac{1}{2}(1 - 4\sin^2\theta_W)\epsilon' G_M^{\gamma,p} G_A^{Z,p}}{\epsilon(G_E^{\gamma,p})^2 + \tau(G_M^{\gamma,p})^2} \right] \tag{5.22}$$

where the kinematic quantities in Eq. (5.21) are given by

$$
\begin{aligned}
\tau &\equiv \frac{Q^2}{4M_N^2} \\
\epsilon &\equiv \frac{1}{1 + 2(1+\tau)\tan^2\frac{\theta}{2}} \\
\epsilon' &\equiv \sqrt{\tau(1+\tau)(1-\epsilon^2)}
\end{aligned}
\tag{5.23}
$$

The uncertainties in the radiative correction of $G_A^{Z,p}$ are large and the radiative corrections involving the strong interaction are not clearly known and extraction of $G_{E,M}^{Z,p(n)}$ from the PV scattering experiments is a tremendous challenge. Higher-order corrections involve strong-interaction corrections when γ and Z interact with many quarks are depicted in FIG. (5.3). Many-quarks corrections are target specific and can modify hadronic matrix elements. Radiative corrections in the axial FF involving parity violating multi-quark interaction can be as large as 30% of the tree level axial form factor. In other words, when once considers the parity-violation associated with the nucleon axial form factor, the weak coupling to the electron must be a vector so that mixing of axial and vector components violates parity. Though this weak coupling to the electron $g_V^e = (1 - 4\sin^2\theta)$ is small, the higher-order diagrams may not necessarily contain a small vector weak coupling and a much larger value than that of the tree-level coupling. One anticipates that with a reliable first-principles estimate of $G_{E,M}^s$, one can also give a prediction of the neutral weak form factors of the proton and the neutron according to Eq. (5.17). Scattering of electron with ^{4}He does not require the knowledge of G_A^Z but it has the problem of iso-spin mixing correction. This introduces a nuclear-structure dependent correction into the asymmetry A_{LR}.

5.4 Previous Calculations

Despite tremendous theoretical efforts, *e.g.* [56–59], a detailed convincing understanding about the sign and magnitude of strange electromagnetic form factors is still

lacking. A detailed review of these theoretical efforts can be found in Ref. [60].

Since the direct calculation of the s-quark loop in the disconnected insertion (DI) is difficult and noisy in lattice QCD, there have been numerous indirect calculations to predict the strange form factors. Most of the calculations rely on different models (such as the heavy baryon chiral perturbation theory) or a combination of experimental and lattice QCD data of connected u- and d-quark contributions [67–69], etc.. The most recent result of such calculations has found $G_M^s(0) = -0.07(3)\mu_N$ and $G_E^s(0)$ consistent with zero [70]. While the authors performed a linear extrapolation of $G_M^s(Q^2)$ to obtain $G_M^s(0)$, this linear behavior is different from what we observe in this work and the most recent lattice QCD analysis in Ref. [71].

The first lattice QCD calculation of strange quark magnetic moment was performed in the quenched approximation [72] and the authors obtained $G_M^s(0) = -0.36(20)$. Another lattice QCD calculation in Ref. [73] with $2 + 1$ flavor dynamical clover fermion with relatively heavy pion masses ($m_\pi \sim 600 - 840$ MeV) followed from the same group who obtained $G_M^s(0) = -0.017(25)(07)\mu_N$ and $G_E^s(0)$ consistent with zero. A recent lattice QCD calculation [71] has been done with quark masses corresponding to $m_\pi = 317$ MeV and the authors obtained $G_M^s(0) = -0.022(8)\ \mu_N$ and, for the first time, a nonzero signal for $G_E^s(Q^2)$ which gave $\langle r_s^2 \rangle_E = -0.0067(25)$ fm^2. However, one still has to perform the calculation at the physical pion mass and on several lattices to consider volume and finite cutoff corrections and over all beat down the noise to obtain a convincing result which will substantially sharpen our picture of the strange quark contributions to the nucleon's EM structure.

Conventionally, we omit the unit nucleon magneton n.m. (μ_N) for G_M^s in the rest of this dissertation. To calculate $\langle N|\bar{s}\gamma_\mu s|N\rangle$, we compute the DI on the lattice where quark loops in the nucleon sea are connected to the valence quarks through the fluctuating gauge background as shown in FIG. 5.4.
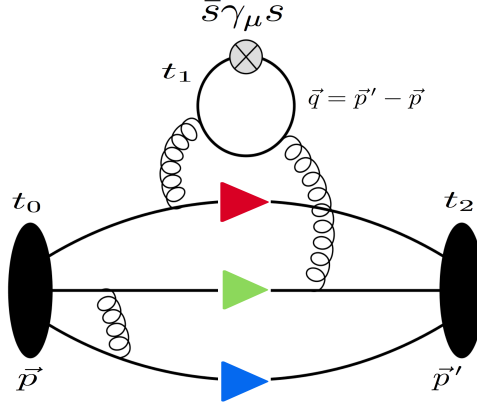
Figure 5.4: Disconnected three-point insertion (DI) to calculate the $\bar{s}\gamma_\mu s$ matrix element in the nucleon state

5.5 Lattice QCD Calculation with Overlap Fermions at The Physical Point

We present lattice calculations of the strange EM form factor using the overlap fermion on the $(2+1)$ flavor RBC/UKQCD domain wall fermion (DWF) gauge configurations. Details of these ensembles are listed in Table 5.2. We use 24 valence quark masses in total for the 24I, 32I, 48I, and 32ID ensembles representing pion masses in the range $m_\pi \in (135, 400)$ MeV to explore the quark-mass dependence of the s-quark form factor.

For the 24I and 48I lattices, we use 12-12-12-32 (16-16-16-32 for 32I and 32ID) random Z_3-noise grid sources with Gaussian smearing. Here, the first 3 numbers in the notations such as 12-12-12-32 denote the intervals of the grid in the 3 spatial directions and the last number is the interval between time slices. A more detailed explanation of the grid source and the smearing can be found in Ref. [74]. We also loop over all the time slices for the nucleon propagator to increase the statistics. We apply eigenmode deflation during the inversion of the quark matrix and utilize the low-mode substitution (LMS) technique developed in Refs. [77,78] during the contraction stage. The low-energy eigenmodes are used to construct many-to-all correlators to substitute

Table 5.2: The parameters for the DWF configurations: spatial or temporal size, lattice spacing [75, 76], the sea strange quark mass under the $\overline{\text{MS}}$ scheme at 2 GeV, the pion mass corresponding to the degenerate light sea quark mass and the numbers of configurations used in this work.

Ensemble	$L^3 \times T$	a (fm)	$m_s^{(s)}$(MeV)	m_π (MeV)	N_{config}
24I [75]	$24^3 \times 64$	0.1105(3)	120	330	203
32I [75]	$32^3 \times 64$	0.0828(3)	110	300	309
48I [76]	$48^3 \times 96$	0.1141(2)	94.9	139	81
32ID [76]	$32^3 \times 64$	0.1431(7)	89.4	171	200

the noise-estimated low-frequency part of the hadron correlators with the exact one and thus named as low-mode substitution. The low-frequency part of the hadron correlators constructed using low-mode substitution makes the use of grid source feasible, otherwise no extra statistics can be gained. As for the quark loops, the low-mode part is exactly calculated with the low eigenmodes of the overlap operator which is called low-mode average (LMA) and the high-mode part is noise estimated by 8 sets of 4-4-4-2 Z_4 noise grids with even-odd dilution as well as additional time dilution [78, 79]. The low-mode averaging for the low-mode contribution is performed by summing over the spatial volume on a time slice. With these techniques implemented, our statistics are from $\sim$ 100k to $\sim$ 500k measurements on the 24I to 48I ensembles. Nucleon two-point (2pt) and three-point (3pt) correlation functions are defined as

$$G_{NN}(\vec{p}\,',t_2;t_0) = \sum_{\vec{x}} e^{-i\vec{p}\,'\cdot\vec{x}} \langle 0|T[\chi(\vec{x},t_2)\sum_{x_i\in G}\bar\chi_S(x_i,t_0)]|0\rangle \,,$$

$$G_{N\mathcal{J}_\mu N}(\vec{p}\,',t_2;\vec{q},t_1;t_0) = \sum_{\vec{x}_2,\vec{x}_1} e^{-i\vec{p}\,'\cdot\vec{x}_2 + i\vec{q}\cdot\vec{x}_1} \langle 0|\, T[\chi(\vec{x}_2,t_2)$$

$$\mathcal{J}_\mu(\vec{x}_1,t_1)\sum_{x_i\in G}\bar\chi_S(x_i,t_0)]|0\rangle \,, \tag{5.24}$$

where t_0 and t_2 are the source and sink temporal positions, respectively, $\vec{p}$, $\vec{p}\,'$ are the

source and sink momenta, respectively, t_1 is the time at which the bilinear operator $\mathcal{J}_\mu(x) = \bar{s}(x)\gamma_\mu s(x)$ is inserted, x_i are points on the spatial grid G, χ is the usual nucleon point interpolation field and $\bar{\chi}_S$ is the nucleon interpolation field with grid-smeared Z_3-noise source, and the three-momentum transfer is $\vec{q} = \vec{p}' - \vec{p}$ as shown in FIG. 5.4. For the point sink and smeared source with $t_0 = 0$ and $\vec{p} = \vec{0}$ and $\vec{q} = \vec{p}'$ the Sachs form factors can be obtained by the ratio of a combination of 3pt and 2pt correlations with appropriate kinematic factors,

$$R_\mu(\vec{q}, t_2, t_1) = \frac{\text{Tr}[\Gamma_m G_{N\mathcal{J}_\mu N}(\vec{q}, t_2, t_1)]}{\text{Tr}[\Gamma_e G_{NN}(\vec{0}, t_2)]} e^{(E_q - m)\cdot(t_2 - t_1)} \frac{2E_q}{E_q + m}.$$

(5.25)

Here, $E_q = \sqrt{m_N^2 + \vec{q}^2}$ and m_N is the nucleon mass. The choice of the projection operator for the magnetic form factor is $\Gamma_m = \Gamma_k = -i(1+\gamma_4)\gamma_k\gamma_5/2$ with $k = 1, 2, 3$ and that for the electric form factor is $\Gamma_e = (1+\gamma_4)/2$. Then in the limit $(t_2 - t_1) \gg 1/\Delta m$ and $t_1 \gg 1/\Delta m$, we can obtain two Sachs form factors by an appropriate choice of projection operators and current directions μ as derived in Chapter 3 in Eq. (4.62):

$$R_{\mu=i}(\Gamma_k) \xrightarrow{(t_2-t_1)\gg 1/\Delta m, t_1 \gg 1/\Delta m} \frac{\epsilon_{ijk}q_j}{E_q + m_N} G_M^s(Q^2),$$

$$R_{\mu=4}(\Gamma_e) \xrightarrow{(t_2-t_1)\gg 1/\Delta m, t_1 \gg 1/\Delta m} G_E^s(Q^2),$$

(5.26)

with $i, j, k \neq 4$ and Δm the mass gap between the ground state and the first excited state. The Sachs magnetic and electric form factors in the spacelike region are related to the nucleon Dirac (F_1) and Pauli form factor (F_2) through the relations:

$$G_M(Q^2) = F_1(Q^2) + F_2(Q^2)$$
$$G_E(Q^2) = F_1(Q^2) - \frac{Q^2}{4m_N^2} F_2(Q^2).$$

(5.27)

Notice that we use smeared grid source and point sink so that, without much additional computational cost, we cannot implement the standard square-root technique to calculate the nucleon 3pt/2pt ratio. We use the smeared source for the three-point

function which would invoke a smeared-smeared two-point function in the square-root formula. This would be quite a bit noisier than that of the smeared-point two-point function. Since we use the smeared-source-point-sink three-point function, the ratio we take contains an extra factor of $Z_p(q)/Z_p(0)$ where $Z_p(q)$ is the wavefunction overlap for a point source with the nucleon momentum q. In the continuum limit, this extra factor is unity and, on the lattice, it will have a $q^2 a^2$ error which can be absorbed in the zero-momentum extrapolation of G_M and charge radius and the subsequent continuum extrapolations. We have numerically checked on about 100 configurations on the 32I (smallest lattice spacing) and 32ID (largest lattice spacing) ensembles that the wavefunction overlap factors indeed do not cancel for nonzero momentum but have a small effect on the matrix element (typically 5-6% for the largest momentum and the lightest pion mass). Upon performing the z-expansion [80, 81] to obtain the magnetic moment at $Q^2 = 0$, the effect on the final result is even smaller, about $1 - 2\%$. The charge radius calculated with such correction has a change of about 2% on the 32I ensemble and 1% on the 32ID ensemble lattice results. Since our statistical uncertainty is about 25% in the global fit for the magnetic moment and the charge radius and an additional 10% (for magnetic moment) and 20% (for charge radius) systematic uncertainties from the z-expansion results will be included in the final result of the global fits, this small effect of overlap factors does not affect our calculation in a significant way. For the 32ID and 48I ensembles, the Q^2 are much smaller than those of 24I and 32I ensembles and the overlap ratio itself is at the $1 - 2\%$ level. We thus ignore it in order to reduce additional computational costs.

We incorporate a global-fit technique described in Ref. [82] to determine the s-quark mass by matching to the renormalized s-quark mass at the $2\,\mathrm{GeV}$ scale in the $\overline{\mathrm{MS}}$ scheme and use normalized vector currents [83]. To control the excited-state contamination and obtain better signal-to-noise ratios we perform a joint two-state correlated fit by simultaneously fitting the standard 3pt/2pt ratio $R(t_2, t_1)$ and the

widely used summed ratio $SR(t_2)$ [84] to calculate DI matrix elements. We call this hybrid method the combined fit (CF) throughout the rest of this work. For more details, see Ref. [85]. The standard 3pt/2pt ratio in the forward matrix element case can be written as

$$
\begin{aligned}
R(t_2, t_1) &= C_3(t_2, t_1)/C(t_2) \\
&= \frac{\sum_{i,j} Z_{\mathbf{f}}^{(i)} Z_{\mathbf{i}}^{(j)} e^{-E^{(i)}(t_2-t_1) - E^{(j)} t_1} \langle \chi_{\mathbf{f}}^{(i)} | J | \chi_{\mathbf{i}}^{(j)} \rangle}{\sum_k Z_{\mathbf{f}}^{(k)} Z_{\mathbf{i}}^{(k)} e^{-E^{(k)} t_2}} \\
&\xrightarrow[t_2 \gg 0]{} \langle \chi_{\mathbf{f}}^{(0)} | J | \chi_{\mathbf{i}}^{(0)} \rangle \\
&\quad + \frac{Z_f^{(1)}}{Z_f^{(0)}} \langle \chi_{\mathbf{f}}^{(1)} | J | \chi_{\mathbf{i}}^{(0)} \rangle e^{-\Delta E (t_2 - t_1)} \\
&\quad + \frac{Z_i^{(1)}}{Z_i^{(0)}} \langle \chi_{\mathbf{f}}^{(0)} | J | \chi_{\mathbf{i}}^{(1)} \rangle e^{-\Delta E t_1} \\
&\quad + \frac{Z_f^{(1)} Z_i^{(1)}}{Z_f^{(0)} Z_i^{(0)}} (\langle \chi_{\mathbf{f}}^{(1)} | J | \chi_{\mathbf{i}}^{(1)} \rangle - \langle \chi_{\mathbf{f}}^{(0)} | J | \chi_{\mathbf{i}}^{(0)} \rangle) e^{-\Delta E t_2} \\
&\quad + ...,
\end{aligned}
\tag{5.28}
$$

where $E^{(i)}$ and $Z^{(i)}$ are the energy and the overlap of the interpolation field of the ith state and $\Delta m = E^{(1)} - E^{(0)}$. For $t_2 \gg t_1 \gg 0$, the contributions from all the terms in the right hand of Eq. (5.28) except the first term vanish, and then we can use Eq. (5.28) to obtain the ground-state matrix element when excited-states contamination is sufficiently suppressed. When t_2 is fixed, one may fit the first term and the combined second and third terms around $t_1 = t_2/2$ to include the effect of the ground state to first excited state transition in the right hand side of Eq. (5.28) which is t_1 dependent. But since the fourth term in the right hand side of Eq. (5.28), which is the difference of the matrix element in the ground state and the first excited state, is independent of t_1 just like the first term, one might not be able to disentangle them and, as a result, a systematic error may be induced by its contribution which is suppressed by $e^{-(E^{(1)} - E^{(0)}) t_2}$ which is shown to be only about 1%-3% in Ref. [85]. Although we include this term in our fits, in most of the cases it does not have any

effect on the fits.

From Eq. (5.28) we can write the $R(t_2, t_1)$ and $SR(t_2)$ fitting formulas for a given direction of current and momentum transfer can be written, respectively, as

$$R(t_2, t_1) = C_0 + C_1 e^{-\Delta m(t_2 - t_1)} + C_2 e^{-\Delta m t_1} + C_3 e^{-\Delta m t_2}, \qquad (5.29)$$

$$
\begin{aligned}
SR(t_2) &= \sum_{t_1 \geq t'}^{t_1 \leq (t_2 - t'')} R(t_2, t_1) \\
&= (t_2 - t' - t'' + 1)C_0 + C_1 \frac{e^{-\Delta m t''} - e^{-\Delta m(t_2 - t' + 1)}}{1 - e^{-\Delta m}} \\
&+ C_2 \frac{e^{-\Delta m t'} - e^{-\Delta m(t_2 - t'' + 1)}}{1 - e^{-\Delta m}} + C_3(t_2 - t' - t'' + 1)e^{-\Delta m t_2}. \qquad (5.30)
\end{aligned}
$$

Here, t' and t'' are the number of time slices we drop at the source and sink sides, respectively, and we choose $t' = t'' = 1$. C_i are the spectral weights involving the excited-states and Δm is, in principle, the energy difference between the first excited state and the ground state. Basically, the two-states fit in Eq. (5.29) dominates in our combined fit method and, for heavier pion masses, the final result of the combined fit is almost identical to the standard 3pt/2pt ratio two-states fit. However, the combined fit becomes useful for getting a stable fit near the physical pion mass and we gain a slight increase in the signal-to-noise ratio. We choose t' and $t'' = 1$ by following the strategy of keeping as many points possible for which χ^2 is acceptable. Δm is effectively an average of the mass difference between the proton and the the lowest few excited states and needs to be determined by the fit. The present scheme with the combined fit (CF) technique as mentioned before allows us to obtain a stable fit and control the excited-state contamination. We find, for the lighter quark masses on the 24I and 32I ensembles, the enhancement in the signal-to-noise ratio is approximately $5\% - 10\%$ and near $m_\pi = 140$ MeV for the 48I and 32ID ensembles the CF fit is more stable compared to the SR and R methods separately.
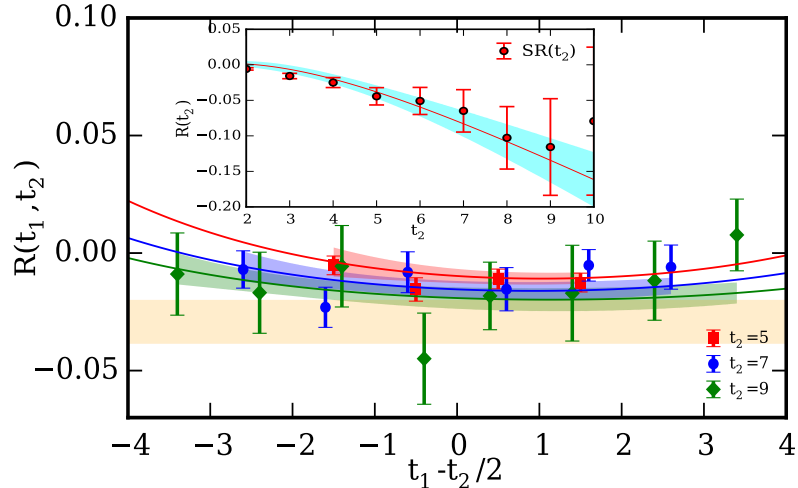
Figure 5.5: Combined fit result for disconnected contribution $G^s_M(Q^2 = 0.0515\,\mathrm{GeV}^2)$ with $m_\pi = 207\,\mathrm{MeV}$. The bands show fits to the 3pt/2pt ratios. The current insertion time t_1 is shifted by half the sink-source separation for clarity.

In FIG. 5.5, we present the result of CF for a particular case, the 48I ensemble with quark masses for the nucleon corresponding to $m_\pi = 207\,\mathrm{MeV}$, $Q^2 = 0.0515\,\mathrm{GeV}^2$, and several source to sink separations $t_2 \in [5-9]$. We show the $SR(t_2)$ plot as an inset in the $R(t_2, t_1)$ plot. One can clearly see from the SR plot that the slope is negative and from the R plot that the 3pt/2pt ratio saturates near $t_2 = 9$. The orange and cyan bands in the R- and SR-plots show the error bound obtained from the CF, which is $G^s_M(Q^2 = 0.0515\,\mathrm{GeV}^2) = -0.029(9)$. We present this plot, in particular, to show how one can obtain a reliable and stable fit near the physical m_π.

The unprecedented precision we obtain in statistics is partly due to the fact that we calculate the low-mode contribution to the loop exactly and the stochastic noise is only used for the estimate of the high-mode contribution. We find that about $15\% - 25\%$ of the signal is saturated by the low modes while determining the s-quark matrix elements in this calculation. FIG. 5.6 shows the summed ratio of the 3pt/2pt corresponding to the low-mode and the total (low-mode + high-mode) contribution to the strange quark magnetic form factor at $Q^2 = 0.051\ \mathrm{GeV}^2$ for a quark mass corresponding to the pion mass $m_\pi = 139\,\mathrm{MeV}$ on the 48I ensemble. It is seen that
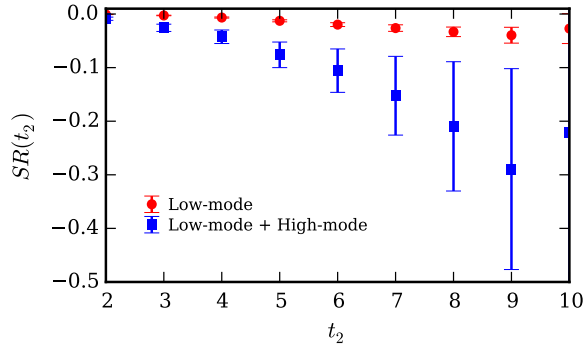
Figure 5.6: Low-mode and high-mode contribution to the strange quark magnetic form factor at $Q^2 = 0.051 \text{ GeV}^2$ for a quark mass corresponding to the pion mass $m_\pi = 139 \text{ MeV}$ on the 48I ensemble.

the low-mode contribution is significant to the total contribution and the low-mode contribution is about 20% of the total contribution. It is also clear from FIG. 5.6 that the signal-to-noise ratio of the low-mode contribution is higher than that of the total contribution.

5.6 Extraction of the strange quark magnetic moment and charge radius

Next, we explore the Q^2 dependence of $G^s_M(Q^2)$ to obtain the strange magnetic moment at $Q^2 = 0$.

It has been a topic of long discussion about what type of form one should use to describe the Q^2-behavior of different form factors. A choice based on the phenomenological interpretation of various data is the dipole form [18] which has been widely used. But a simple polynomial fit does not converge when there exist cuts in the timelike domain. For example, in the case of a photon to two pion transition, there exists a cut at $q^2 = -Q^2 = 4m_\pi^2$ in the timelike domain as shown in FIG. 5.7. Because of the existence of this pole $1/(q^2 - 4m_\pi^2)$, a polynomial expansion of the form factor should not converge for any $Q^2 > 4m_\pi^2$. The weight of this pole may be small but one should not ignore its effect when fitting the form factor data. To overcome this prob-

lem, a conformal mapping of variable Q^2 to another variable z has been proposed in Refs. [80, 81]. The conformal mapping is performed in such a way that one is allowed to perform a polynomial expansion in z, such that the timelike momentum transfers (*i.e.* all poles of the form factors) map onto the unit circle $z = 1$ and the spacelike momentum transfers map onto the real line $|z| < 1$. For more details, see [80, 81].
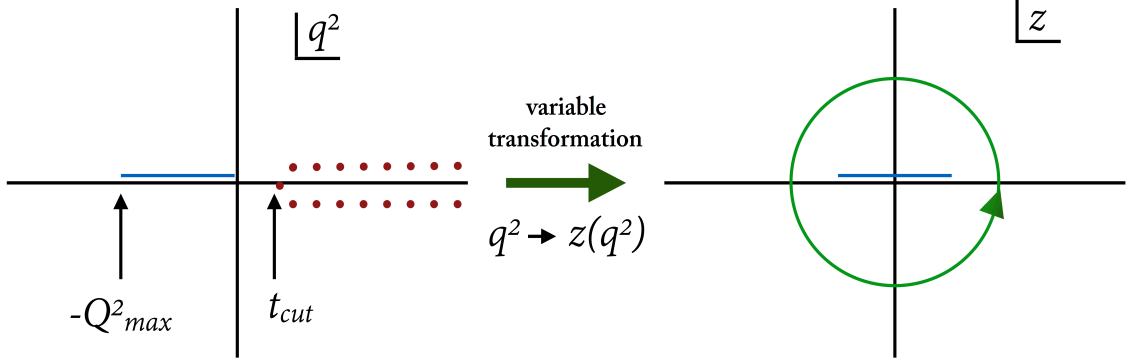
Figure 5.7: Model-independent z-expansion: Conformal mapping of the cut plane to the unit circle.

Another reason we do not use the dipole fit in the calculation is because the Q^2 behaviors of the disconnected light and strange form factors are unknown and one would prefer not to be biased with a specific form of the extrapolation. (There exist also other phenomenological models for the Q^2-dependence of strange form factors, for example in Ref. [86].) Therefore we adopt the model-independent z-expansion fit. We take $t_{\text{cut}} = 4m_\pi^2$ for fitting the disconnected light quarks form factor and $t_{\text{cut}} = 4m_K^2$ for the strange quark form factor. We have verified that a different choice of t_{cut} such as $9m_\pi^2$ has less than a few percent effect on our extrapolations.

In FIG. 5.8, we show an example of the extraction of strange quark magnetic moment at $Q^2 = 0$ from the form factor data at different Q^2 using the z-expansion fit. We compare both the dipole form [18]

$$G_M^{s,dipole}(Q^2) = \frac{G_M^s(0)}{(1 + \frac{Q^2}{\Lambda^2})^2} \tag{5.31}$$

61

and the model independent z-expansion fit [80, 81] given by

$$G_M^{s,z-exp}(Q^2) = \sum_{k=0}^{k_{\max}} a_k z^k \quad , \quad z = \frac{\sqrt{t_{\rm cut} + Q^2} - \sqrt{t_{\rm cut}}}{\sqrt{t_{\rm cut} + Q^2} + \sqrt{t_{\rm cut}}}. \tag{5.32}$$

We present the extrapolation of $G_M^s(0)$ using both the dipole and z-expansion methods in FIG. 5.8 with the smallest lattice spacing $a = 0.0828(3)$ fm used in our simulation and lattice data at the unitary point for the 32I ensemble with a pion mass $m_\pi \sim 300$ MeV. More examples of strange magnetic quark magnetic moment and charge radius from z-expansion near and at the physical pion mass will be presented in Chapter 6.

We set $t_{\rm cut} = (2m_K)^2$. We keep the first three coefficients multiplying z^k in the z-expansion formula and perform fits versus Q^2. We calculate the jackknife ensemble average $a_{2,avg}$ of the coefficient a_2 and then perform another fit by setting a_2 centered at $a_{2,\rm avg}$ with a prior width equal to $2 \times |a_{2,\rm avg}|$. We find the effect of setting this prior is almost insignificant for the 24I and 32I ensemble data, especially at heavier quark masses. However, the prior stabilizes the extrapolation of $G_M^s(Q^2)$ for pion masses around the physical point for the 48I ensemble. Since the z-expansion method guarantees that a_k coefficients are bounded in size and that higher order a_k's are suppressed by powers of z^k, we carefully check the effect of the a_3 coefficient in our fit formula and estimate this effect to calculate the systematic uncertainties in the z-expansion fit. The present calculation does not provide any conclusive evidence of any statistically significant difference between these two methods, as seen in the figure. However, because of model independence and goodness of the fit, we use z-expansion fit results in the rest of our calculations.
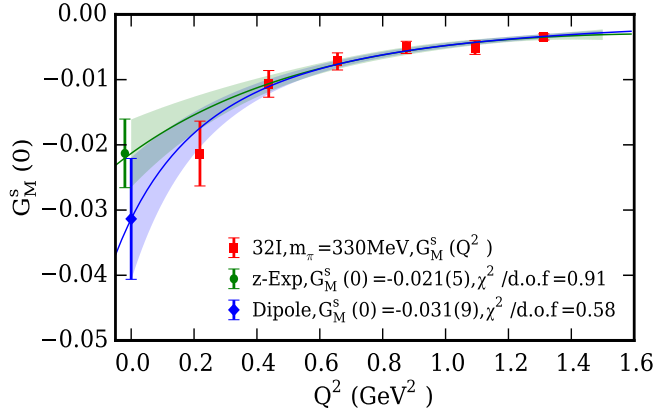
Figure 5.8: Comparison between the classical dipole form and the model-independent z-expansion fit to study the Q^2 dependence of G^s_M and extract $G^s_M(0)$. The $G^s_M(Q^2)$ data points correspond to the 32I ensemble with quark masses corresponding to $m_\pi = 300\,\text{MeV}$.

5.7 Global Fits and Continuum Extrapolations

From the z-expansion extrapolations, we obtain 24 different estimates of $G^s_M(0)$ from four different lattice ensembles with varying quark masses. As the nucleon 2pt correlation function depends on the valence quark masses and the strange quark matrix elements depend on m_{loop}, we use a chiral extrapolation linear in m_π and $m_{\text{loop}} = m_K$ [59, 87–89]. Undertaking a global fit which combines the chiral extrapolation, the physical quark mass interpolation, and the continuum extrapolation for the charmonium, D_s and D^*_s on the several lattice ensembles, we have been able to obtain the charm and strange quark masses in the $\overline{\text{MS}}$ scheme at $\mu = 2\,\text{GeV}$ consistent within one sigma of the PDG values in Ref. [82]. For a given valence quark mass, we first calculate the matrix element with 2 different s-quark masses (for example, $m_s = 0.98$ GeV and 0.102 GeV) close to the physical value of s-quark mass obtained in Ref. [82]. We then perform a linear interpolation of the strange quark matrix elements associated with these two s-quark masses to the physical s-quark mass and obtain the strange quark matrix elements at the physical s-quark mass. We estimate

this uncertainty to be less than 5%. We have also verified this by performing 2 different correlated combined fits of the 3pt/2pt ratio for a given valence quark mass and two different s-quark masses separately and calculated the differences in the fit results. In both cases the differences are almost the same and the largest difference we estimate is about 5% in the extrapolated value of of $G_M^s(0)$. Therefore we anticipated an error of 5% as a systematic in the final result. To account for the partial quenching effect with the valence-sea pion mass $(m_{\pi,vs})$, and the $\mathcal{O}(a^2)$ correction and volume dependence [90], the global fit formula we use for the extrapolation of $G_M^s(0)$ to the physical point is

$$G_M^s(0; m_\pi, m_{\pi,vs}, m_K, a, L) = A_0 + A_1 m_\pi + A_2 m_K$$
$$+ A_3 m_{\pi,vs}^2 + A_4 a^2 + A_5 m_\pi \left(1 - \frac{2}{m_\pi L}\right) e^{-m_\pi L}, \tag{5.33}$$

where m_π (m_K) is the valence pion (kaon) mass and $m_{\pi,vs}$ is the partially quenched pion mass defined as

$$m_{\pi,vs}^2 = 1/2(m_\pi^2 + m_{\pi,ss}^2) \tag{5.34}$$

with $m_{\pi,ss}$ the pion mass corresponding to the sea quark mass. A_4 includes the mixed action parameter Δ_{mix} [91]. This is a special case since we adopt $m_{\pi,vs}^2$ which includes Δ_{mix}. It would not be true if one use linear or cubic terms. The extrapolation of the strange magnetic moment is shown in FIG. 5.9 and at the physical point in the limit $a \to 0$ and $L \to \infty$ we obtain

$$G_M^s(0)|_{\text{physical}} = -0.064(14)(04)(06)(06) \, \mu_N. \tag{5.35}$$

Here, the uncertainties in the parentheses are from the statistics, interpolation to the physical s-quark mass [82], introducing a_3 coefficients in the z-expansion fit, and the global fit formula for the continuum extrapolation of $G_M^s(0)$, respectively. To calculate the uncertainty associated with the global fit formula, we consider the higher order volume correction terms $(m_\pi^{3/2}/\sqrt{L})e^{-m_\pi L}$ [90], $m_N m_K$ [89], $\log m_\pi^2$, and
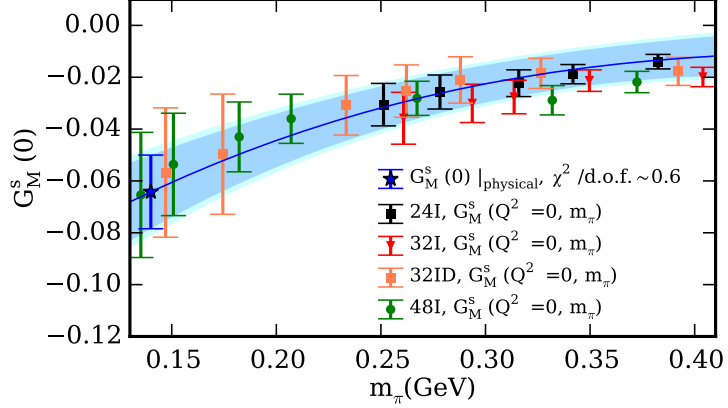
Figure 5.9: Strange magnetic moment at 24 quark masses on 24I, 32I, 48I, and 32ID ensembles as a function of the pion mass. The curved blue line in the figure shows the behavior in the infinite volume and continuum limit. The cyan band shows the combined statistical and systematic uncertainties added in quadrature.

$m_{\pi,vs}$. We obtain the fit coefficients: $A_1 = 0.61(16)$, $A_2 = -2.26(49)$, $A_3 = 0.31(12)$, $A_4 = 0.015(16)$, and $A_5 = -4.0(2.4)$ with the sign of A_5 consistent with that in Ref. [90]. We note that the $\mathcal{O}(a^2)$ effect is small, whereas the partial quenching effect and the volume correction along with the quark mass dependence play roles in our global fit. While the $G_M^s(0)$ values for different ensembles are consistent within uncertainty near $m_\pi = 250\,\mathrm{MeV}$, from the fit coefficients it can be seen that, near $m_\pi = 400\,\mathrm{MeV}$, $G_M^s(0)$ calculated from the 48I ensemble is more negative due to the partial quenching effect.

In order to better understand the consistency between 24I, 32I, 32ID and 48I ensembles data at various quark masses and lattice spacings and volumes, we refer to the following table:

One important point to notice is that the coefficient A_4 has opposite sign to that of A_5 which is consistent with the sign of the volume correction term in Ref. [90]. From the fit results of the global analysis and from Table 5.3, we can see that near $m_\pi = 0.38\,\mathrm{GeV}$, the difference between the 24I result at 382 MeV and the 32I result

Table 5.3: Effect of various fit parameters in the global fit of strange quark magnetic moment. $G_M^{s,\mathrm{fit}}|_{\mathrm{phys}}$ is the magnetic moment in the limit $a \to 0$, $L \to \infty$, and $m_{\pi,vs} = m_{\pi,vv}$ at given pion masses in the first column of the table. $V.C.$ is the volume correction term. $G_M^{s,\mathrm{fit}}$ values in the seventh column are estimated using the global fit results. All G_M^s values in table 1 is at $Q^2 = 0$. The pion masses m_π are in GeVs.

m_π	Ensemble	$G_M^{s,\mathrm{fit}}\|_{\mathrm{phys}}$	$A_3(m_{\pi,vs}^2 - m_\pi^2)$	$A_4 a^2$	$A_5 \times V.C.$	$G_M^{s,\mathrm{fit}}$	Lattice G_M^s
0.251	24I	-0.032(8)	0.007(3)	0.005(5)	-0.014(8)	-0.031(6)	-0.031(08)
0.260	32I	-0.030(8)	0.004(2)	0.003(3)	-0.014(8)	-0.036(7)	-0.036(10)
0.267	48I	-0.028(8)	-0.008(3)	0.005(5)	-0.0005(3)	-0.030(6)	-0.028(07)
0.262	32ID	-0.036(9)	-0.004(2)	0.008(8)	-0.003(2)	-0.034(7)	-0.025(10)
0.382	24I	-0.013(7)	-0.006(2)	0.005(5)	-0.006(4)	-0.019(4)	-0.014(03)
0.403	32I	-0.012(8)	-0.012(5)	0.003(3)	-0.005(3)	-0.024(5)	-0.019(04)
0.372	48I	-0.014(7)	-0.019(7)	0.005(5)	-0.00004(2)	-0.027(5)	-0.022(04)
0.392	32ID	-0.013(7)	-0.020(8)	0.008(8)	-0.00014(8)	-0.025(4)	-0.018(05)

at 403 MeV is mainly due to the partial quenching effect (A_3) and the lattice spacing (A_4). On the other hand, the partial quenching effect on the 48I ensemble data is large and negative which makes the $G_M^s(0)$ more negative compared to the 24I ensemble data. One can check this effect by adding the partial quenching, lattice spacing and finite volume corrections in the table and obtaining approximately the same difference between the 24I and 48I ensemble data listed in the table. Near $m_\pi = 0.25\,\mathrm{GeV}$, the partial quenching effect between the 48I and 24I lattices is largely offset by their volume corrections and result is approximately the same value of $G_M^s(0)$ as can be seen in FIG. 5.9 above. In all cases the volume correction to the 48I ensemble is almost negligible compared to those of 24I and 32I ensembles. However, at lower pion mass, all four lattice ensemble data have larger uncertainty and they are consistent with each other within error bars. From the fit results, it is also clear that the finite lattice spacing correction is very small in our analysis.

For a given valence quark mass we fit $G_E^s(Q^2)$ using the z-expansion method described above and calculate the charge radius from the fitted slope of the data using the definition $\langle r_s^2 \rangle_E \equiv -6\frac{dG_E^s}{dQ^2}|_{Q^2=0}$. The net strangeness in the nucleon is

66

zero, and thus $G_E^s(0) = 0$, which we confirm in our simulation. Chiral extrapolation to the $\langle r_s^2 \rangle_E$ data is obtained from Ref. [89]. Because the method of finite volume correction of nucleon charge radius is less clear and hard to obtain [92,93], we employ an empirical formula for the volume correction to describe our lattice data. The empirical fit formula we use to obtain $\langle r_s^2 \rangle_E$ at the physical point is

$$\langle r_s^2 \rangle_E(m_\pi, m_{\pi,vs}, m_K, a, L) = A_0 + A_1 \log (m_K)$$

$$+ A_2 m_\pi^2 + A_3 m_{\pi,vs}^2 + A_4 a^2 + A_5 \sqrt{L} e^{-m_\pi L}. \tag{5.36}$$

We find that the volume correction term similar to the pion charge radius term derived in Ref. [93] describes our lattice data well. From the fitted values of the coefficients in Eq. (5.36), namely, $A_1 = 0.03(2)$, $A_2 = -0.04(8)$, $A_3 = 0.03(2)$, $A_4 = -0.0004(27)$, and $A_5 = 0.001(7)$, it is seen that among different contributions the quark mass dependence and partial quenching effect are more important in determining $\langle r_s^2 \rangle_E$ from our lattice data. We also consider $e^{-m_\pi L}$, m_K instead of $\log m_K$, $1/m_N^2$ [89], $m_{\pi,vs}$ and calculate a systematic error derived from different terms in the global fit formula. We present the value of $\langle r_s^2 \rangle_E$ at the physical point in FIG. 5.10 which gives

$$\langle r_s^2 \rangle_E|_{\text{physical}} = -0.0043(16)(02)(08)(07) \, \text{fm}^2. \tag{5.37}$$

The uncertainties in the second and third parentheses of Eq. (6.8) are obtained using similar methods described in the case of $G_M^s(0)$. The lowest Q^2 values for 48I and 32ID ensembles are 0.051 and 0.073 GeV^2 respectively, which are almost $3 - 4$ times smaller than the lowest $Q^2 = 0.22 \, \text{GeV}^2$ of the 24I and 32I ensemble. As extracting the charge radius from the form factor data can be sensitive to the lowest available Q^2, this can affect our determination of $\langle r_s^2 \rangle_E$. A 20% uncertainty in introducing the a_3 term in the z-expansion has been included as a systematic in the final result of $\langle r_s^2 \rangle_E$.
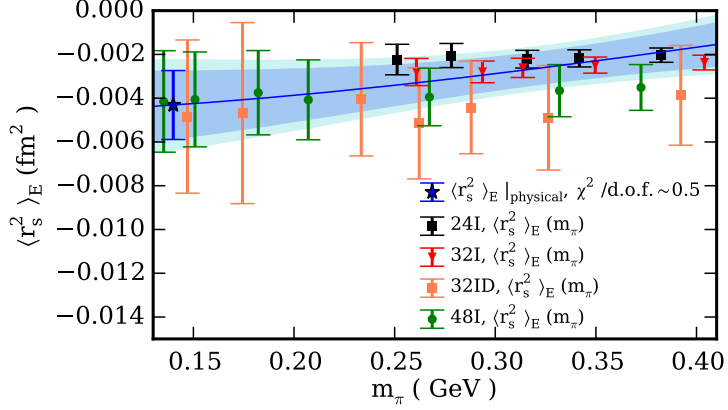
Figure 5.10: Strange charge radius at 24 quark masses on 24I, 32I, 48I, and 32ID ensembles as a function of the pion mass. The curved blue line in the figure shows the behavior in the infinite volume and continuum limit. The cyan band shows the combined statistical and systematic uncertainties added in quadrature.

We present FIG. 5.11 to compare our result of $G_M^s(0)$ and $G_M^s(Q^2 = 0.1\,\mathrm{GeV}^2) = -0.037(10)(05)$ with some other measurements of $G_M^s(0)$ and global analyses of G_M^s at $Q^2 = 0.1\,\mathrm{GeV}^2$. We strongly believe that controlling excited-state contamination, performing the simulation near the physical pion mass, and considering the finite size effect altogether play an important role in determining the strange magnetic moment as observed in our lattice simulation.

One can obtain $G_{E,M}^s(Q^2)$ at the physical point from the fit parameters of the model-independent z-expansion fits. We use the fit parameters a_k to interpolate $G_{E,M}^s$ values at various Q^2 for a given valence quark mass on the lattice. The available Q^2 on the 24I and 32I ensembles are $Q^2 \in (0.22, 1.31)\,\mathrm{GeV}^2$, on the 32ID ensemble are $Q^2 \in (0.07, 0.43)\,\mathrm{GeV}^2$ and on the 48I ensemble are $Q^2 \in (0.05, 0.31)\,\mathrm{GeV}^2$. It is a common problem for lattice QCD calculations that the signal-to-noise-ratio decreases as one reaches the physical pion mass. From our study, we also find that the lattice results of $G_{E,M}^s(Q^2)$ near the physical pion mass $m_\pi = 140\,\mathrm{MeV}$ for the 48I ensemble [76] are noisier compared to the $G_{E,M}^s(Q^2)$ obtained from the lattice

68
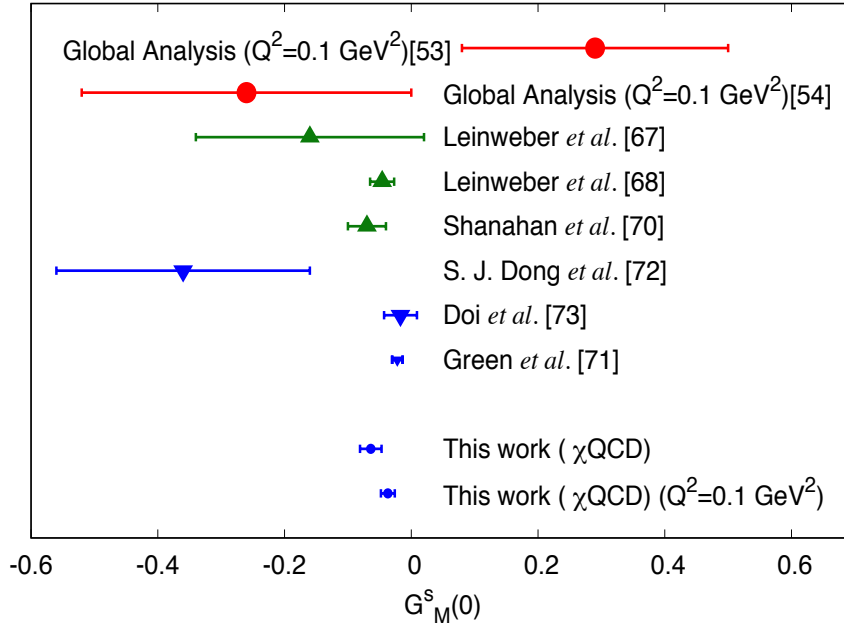
Figure 5.11: Comparison of some of the many determinations of the strange magnetic moment. Results in red are from the global analysis of world data, results in green are from indirect calculations, and results in blue are from lattice QCD calculations.

ensembles with heavier pion mass. Although the largest available momentum transfer we have on the 24I and 32I ensemble is $Q^2 \sim 1.3\,\mathrm{GeV}^2$, the largest momentum transfer available on the 48I ensemble is $Q^2 \sim 0.31\,\mathrm{GeV}^2$. We note that the extrapolation of the nucleon strange electromagnetic form factor leads to uncontrolled error bars after $Q^2 \sim 0.5\,\mathrm{GeV}^2$ for the 48I ensemble and we therefore constrain the extrapolations of the 48I ensemble electromagnetic form factor up to $Q^2 = 0.5\,\mathrm{GeV}^2$. It is important to note that the lattice QCD estimate of $G^s_{E,M}(Q^2)$ we present here is the most precise and accurate first-principles calculation of s-quark electromagnetic form factors to date. This is the only calculation at the physical pion mass where one has considered the quark mass dependence, with finite lattice spacing (a), volume corrections, and partial quenching effect to determine the s-quark electromagnetic form factors. The χ^2/d.o.f. for different Q^2 global fit ranges between 0.7-1.13. For example, in the continuum limit, the global fit for $Q^2 = 0.25\,\mathrm{GeV}^2$ results in the physical value

69

of $G_E^s|_{\text{phys}} = 0.0024(8)$, $A_1 = 0.58(30)$, $A_2 = -0.29(15)$, $A_3 = -0.003(9)$, $A_4 = 0.001(2)$, and $A_5 = -0.001(3)$ with $\chi^2/\text{d.o.f.} = 1.1$. One can consider the $\log(m_K)$-term in the chiral extrapolation of G_E^s as shown in [89]; however, our analysis shows that this term does not have any effect on the global fit for our lattice data. A similar vanishing difference has been observed if one considers a $e^{-m_\pi L}$ instead of a $\sqrt{L}e^{-m_\pi L}$ term in the volume correction. For example, including the factor $\log(m_K)$ and $e^{-m_\pi L}$ instead of $\sqrt{L}e^{-m_\pi L}$ one obtains, $G_E^s|_{\text{phys}} = 0.0026$ in comparison with $G_E^s|_{\text{phys}} = 0.0024$. We include these small effects in the systematics of the global fit results. We also consider a 20% systematic uncertainty from the model-independent z-expansion interpolation coming from adding a higher order term a_3 while fitting the $G_E^s(Q^2)$ data. These uncertainties from the empirical fit formula and z-expansion are added to the systematics. FIG. 5.12 shows the Q^2-dependence of the s-quark Sachs electric form factor G_E^s in the continuum limit, $i.e.$ $m_\pi = m_{\pi,vs} \to 140\,\text{MeV}$, $a \to 0$, and $L \to \infty$ with the statistical and systematic uncertainties. The nonzero value of the strange Sachs electric form factor G_E^s at any $Q \neq 0$ means that the spatial distribution of the s and $\bar{s}$ quarks are not the same in the nucleon. If the distributions of the s and $\bar{s}$ quarks were the same, their contribution to the nucleon electric FF would have the same magnitude with opposite signs. Since the net strangeness in the nucleon is zero, we have $G_E^s = 0$ at $Q^2 = 0$.

Similarly, we calculate the strange Sachs magnetic form factor G_M^s at a particular Q^2 using the same global fit formula used for the calculation of the magnetic moment. From the global fit formula, for example, in the continuum limit at $Q^2 = 0.25\,\text{GeV}^2$, we obtain $G_M^s|_{\text{phys}} = -0.018(4)$, $A_1 = 0.04(3)$, $A_2 = -0.18(12)$, $A_3 = -1.27(84)$, $A_4 = 0.008(6)$, and $A_5 = 0.04(5)$ with $\chi^2/\text{d.o.f.} = 1.13$. From the fitted values of the parameters in the global fit formula, it is seen that the quark mass dependencies play an important role in calculating $G_M^s(Q^2)$ at the physical point. A 9% systematic uncertainty from the model-independent z-expansion and an uncertainty from the
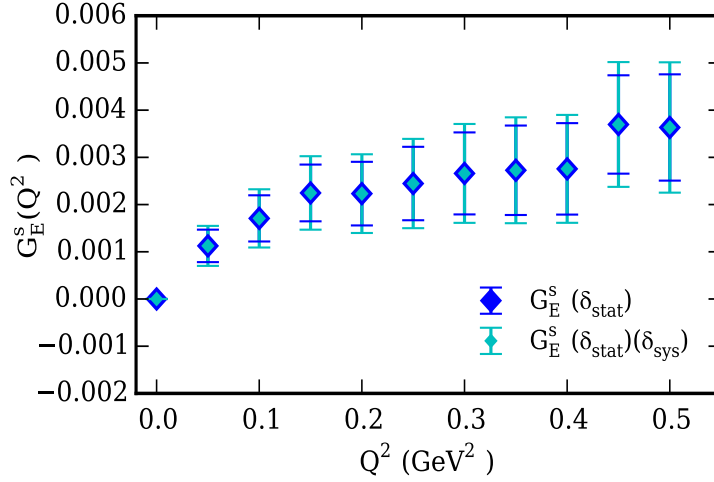
Figure 5.12: Q^2-dependence of the strange Sachs electric form factor. The blue error bars indicate the statistical uncertainties and the cyan error bars indicate the statistical and systematic uncertainties added in quadrature.

empirical fit formula have been included. We obtain systematics from the global fit formula by replacing the volume correction by $e^{-m_\pi L}$ only and also by adding a $m_{\pi,vs}$ term in the fit and include the difference in the systematics of the global fit results. The results of $G_M^s(Q^2)$ in the continuum limit are presented in FIG. 5.13.
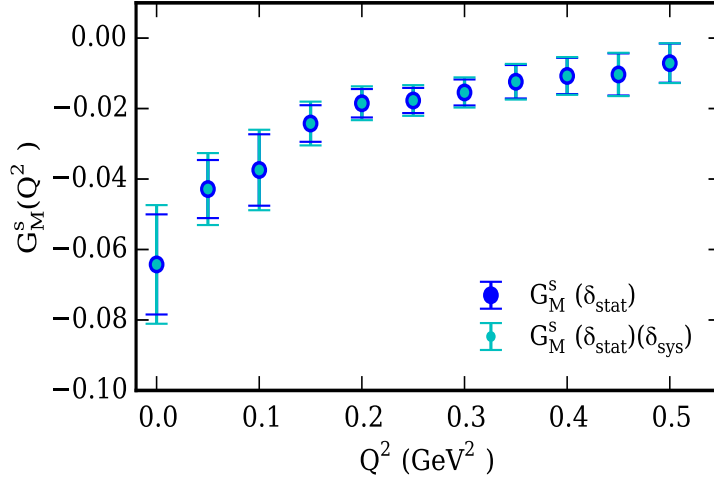
Figure 5.13: Q^2-dependence of the strange Sachs magnetic form factor. The blue error bars indicate the statistical uncertainties and the cyan error bars indicate the statistical and systematic uncertainties added in quadrature.

5.8 Conclusion

In conclusion, we have performed a robust first-principles lattice QCD calculation using four different $2 + 1$ flavor dynamical fermion lattice ensembles including, for the first time, the physical pion mass to explore the quark mass dependence and with finite lattice spacing and volume corrections to determine the strange quark matrix elements in the vector channel. We have performed a two-state fit where we combined both the ratio method and the summed-ratio method to control the excited-state contamination. The statistical error is greatly reduced by improving the nucleon propagator with low-mode substitution and quark loop with low-mode averaging. To explore the strange vector form factors at different momentum transfers, we implemented model-independent z-expansion fits. We also have obtained precise estimates of the strange quark electric and magnetic form factors in the momentum transfer range of $0\,\mathrm{GeV}^2 \leq Q^2 \leq 0.5\,\mathrm{GeV}^2$. Given our precise lattice prediction for the strange quark magnetic moment of $G_M^s(0) = -0.064(17)\mu_N$ and strange charge radius $\langle r_s^2 \rangle_E = -0.0043(21)\,\mathrm{fm}^2$ at the physical point with systematic errors included,

72

we anticipate these results to be verified by experiments in the future and, together with experimental inputs, to lead to a more precise determination of various weak form factors.

Chapter 6 Light-Sea Quarks Contribution to the Nucleon Magnetic Moment and Charge Radius and Electromagnetic Form Factors

6.1 Abstract

We have performed a comprehensive analysis of the light and strange disconnected-sea quarks contribution to the nucleon magnetic moment, charge radius, and the electric and magnetic form factors. The lattice QCD calculation includes ensembles across several lattice volumes and lattice spacings with one of the ensembles at the physical pion mass. We adopt a model-independent extrapolation of the nucleon magnetic moment and the charge radius. We have performed a simultaneous chiral, infinite volume, and continuum extrapolation in a global fit to calculate results in the continuum limit. We find that the combined light-sea and strange quarks contribution to the nucleon magnetic moment is $-0.022(11)(09)\,\mu_N$ and to the nucleon mean square charge radius is $-0.019(05)(05)\,\mathrm{fm}^2$. The most important outcome of this lattice QCD calculation is that while the combined light-sea and strange quarks contribution to the nucleon magnetic moment is small at about 1%, a negative 2.5(9)% contribution to the proton charge radius and a relatively larger positive 16.3(6.1)% contribution to the neutron charge radius come from the sea quarks in the nucleon. For the first time, by performing global fits, we also give predictions of the light-sea and strange quarks contributions to the nucleon electric and magnetic form factors at the physical point and in the continuum and infinite volume limits in the momentum transfer range of $0 \leq Q^2 \leq 0.5\,\mathrm{GeV}^2$.

6.2 Introduction

Nucleon electromagnetic form factors of a hadron are of substantial interest because they are related to the dynamical content of the electric and magnetic currents distribution inside the hadron and characterize the internal structure of a non-point-like particle. The quest for a detailed quantitative understanding of the nucleon electromagnetic form factors is an active field of the experimental nuclear physics, lattice QCD simulations, and other model calculations. However, some unsolved questions still remain regarding the nucleon electromagnetic form factors and their properties at low momentum transfer (Q^2).

A complete first-principles lattice QCD calculation of the nucleon magnetic moment and charge radius including both the valence and connected-sea quarks, called connected insertion (CI), and the disconnected-sea quarks contribution, called disconnected insertion (DI), is of immense importance and is not present in the literature. By disconnected insertions, we mean the nucleon matrix elements involving self-contracted quark graphs (loops), which are correlated with the valence quarks in the nucleon propagator by the fluctuating gauge background. It has also been found in various experiments that non-valence components in the nucleon hold surprisingly large effects in describing its properties. One desires to perform a simulation at the physical pion mass and consider large volumes and small lattice spacings and overall obtain a very good signal-to-noise ratio to compare the lattice results with the experimental value – which is a highly ambitious goal to the lattice community with current numerical resources. In two previous lattice QCD calculations [94, 95] the authors have calculated the disconnected light-quarks contribution to the nucleon electromagnetic form factors. In Ref. [94], the simulation has been done with quark mass equivalent to pion mass 370 MeV and the authors obtained disconnected light-quark contribution to the nucleon electromagnetic form factor (EMFF) consistent with zero within uncertainties. In Ref. [95], the disconnected light-quarks contribu-

tion to the nucleon EMFF was obtained to be non-zero and small in the momentum transfer range of $0 \leq Q^2 \lesssim 1.2 \text{ GeV}^2$ with the simulation performed at a quark mass corresponding to pion mass 317 MeV.

The disconnected light-quarks contribution to the nucleon EMFF has not been considered in most of the lattice calculations because of the following reasons: 1) the current status of the lattice QCD simulations with disconnected quark loops are numerically intensive and in general very noisy, especially near the physical pion mass, and 2) most of the previous lattice QCD calculations were performed under the assumption that DI light-quarks contribute a negligible amount to the nucleon magnetic moment and charge radius. Therefore, most of the earlier simulations aimed to calculate only the isovector nucleon quantities and simulations were performed at relatively heavier pion masses [96–103]. Since simulations directly at the physical pion mass are now becoming available, some collaborations are pursuing lattice QCD calculations near or at the physical pion mass. Nonetheless, simulations near the physical pion mass exhibit increased sensitivity to the statistical fluctuations and one requires a large number of measurements to obtain good signal-to-noise ratio and to control the undesired excited-states contaminations. Thus a majority of the recent calculations near the physical pion mass still concentrate on the CI calculations only [104–107].

By performing a first-principles calculation, we find that the total contribution of the light (up and down) sea and strange quarks to the nucleon charge radius is negative and significant. Combining the result of the strange quark magnetic moment and charge radius calculated in our previous work [29] with the DI light-quarks contribution, we obtain the total contribution to the nucleon magnetic moment and charge radius from the disconnected-sea quarks. Our estimate of strange quark magnetic moment and charge radius is almost ten times better than those of the most precise experimental values. However, Our overall DI calculation uncertainty is large com-

pared to the precision of the experimental uncertainty of the proton charge radius and one also needs to perform a CI calculation at the physical point with high precision to draw any conclusion as to whether the DI contribution can have a significant impact on the understanding of the 4% discrepancy of the proton charge radius puzzle from the lattice QCD viewpoint. Nonetheless, the present work gives the first calculation of the disconnected light and strange quarks contribution to the nucleon EMFF at the physical point and provides important information about the sign of the sea-quarks contribution to the nucleon EMFF. While almost all lattice QCD connected-insertion calculations concentrate on extractions of the proton charge radius, the neutron Sachs electric form factor $G_E^n(Q^2)$ calculation is challenging due to the poor signal-to-noise ratio, as shown in Ref. [108]. A recent lattice QCD calculation [109] performed at the physical pion mass also shows that obtaining a precise prediction of $G_E^n(Q^2)$ and neutron charge radius close to the experimental value is indeed a challenging problem. In this work, we have investigated the importance of the DI contribution to the neutron electric form factor calculation and a clear message is to be taken that one must include the DI contribution to the neutron charge radius to shift the lattice estimates toward the experimental value. It also gives a non-negligible contribution to the proton charge radius.

In Sec. 6.3, we provide examples of a hybrid two-states fit to compute matrix elements from the ratio of nucleon three-point to two-point correlation functions. We implement a model-independent extrapolation of nucleon magnetic moment and charge radius from the EMFFs in the momentum transfer range of $0.051 \lesssim Q^2 \lesssim 1.31$ GeV^2 and show examples in Sec. 6.4. In Sec. 6.5, finite lattice spacing and finite volume corrections are included in a global fit with 24 valence quark masses on four different lattice ensembles with different lattice spacings, different volumes, and four sea quark masses including one at the physical point. From the fit coefficients of the model-independent z-expansion, we perform global fits to get estimates of the

disconnected-sea light and strange quarks contributions to the nucleon electromagnetic form factors at the physical point. Finally, we present a conclusion to our lattice QCD analysis in Sec. 6.6.

6.3   Combined two-states fit

In lattice QCD simulations, nucleon correlation functions suffer from an exponentially increasing noise-to-signal ratio which imposes a serious limitation on the source-sink separation t_2, especially when DI calculations are performed. In general, DI calculations are notoriously noisier compared to the CI calculations. It is also hard to extract the ground-state properties of the nucleon since the lowest excited-state, the Roper resonance, N(1440), lies close to the nucleon mass. There can also be an additional excited-states contamination, for example from the πN-states. Therefore, ideally one requires a substantially large source-sink separation, approximately $t_2 = 1.5$ fm, to extract nucleon ground-state matrix elements without being much affected by the excited-state contaminations. Though it is possible to go up to about 1.4 fm source-sink separation in some of the CI calculations [101, 106] only, at the present stage of numerical simulation it is quite challenging to go much beyond $t_2 \approx 1$ fm and obtain a reasonable signal-to-noise ratio for the DI calculations. Therefore, to have an estimate of the nucleon ground-state matrix elements, we employ a hybrid joint two-state correlated fit by simultaneously fitting the standard 3pt/2pt ratio $R(t_2, t_1)$ and the widely used summed ratio $SR(t_2)$ [84] to calculate DI matrix elements. We do not obtain any signal for the fit parameter C_3 defined in Eq. (5.30) based on the analysis of our lattice data points for light-sea quarks. Therefore, excluding this factor from the combined fit does not affect the final outcome of the fit and we write the $R(t_2, t_1)$ and $SR(t_2)$ fitting formulas for a given direction of current and momentum transnfer as

$$R(t_2, t_1) \quad = \quad C_0 + C_1 e^{-\Delta m(t_2 - t_1)} + C_2 e^{-\Delta m t_1}, \tag{6.1}$$

$$SR(t_2) = \sum_{t_1 \geq t'}^{t_1 \leq (t_2 - t'')} R(t_2, t_1)$$

$$= (t_2 - t' - t'' + 1)C_0 + C_1 \frac{e^{-\Delta m t''} - e^{-\Delta m(t_2 - t' + 1)}}{1 - e^{-\Delta m}}$$

$$+ C_2 \frac{e^{-\Delta m t'} - e^{-\Delta m(t_2 - t'' + 1)}}{1 - e^{-\Delta m}}. \tag{6.2}$$

We illustrate two examples in FIGS. 6.1 and 6.2 to obtain magnetic form factors at given Q^2-values from the lattice data and present the fitting details in Table 6.1. The source-sink separation we use for the fitting of 32I ensemble data is $t_2 \in (6, 13)$ and $t_2 \in (5, 10)$ for the 48I ensemble data. As discussed earlier, as with almost all of the DI calculations, we are forced to constrain the t_2-window around 1.1 fm due to the limitations of good signal-to-noise ratio. However, in principle, the two-states fit should compensate for this limitation to a certain degree. We perform a correlated combined fit of the ratio and summed ratio data because one could obtain a smaller uncertainty with an uncorrelated fit and underestimate the errors. Likewise, all of the subsequent fits in the article are also correlated fits.

Table 6.1: The parameters of correlated combined two-states fits in Eqs. (6.1) and (6.2) to obtain disconnected light-quarks magnetic form factor at given momentum transfers.

Ensemble	m_π (GeV)	Q^2 (GeV^2)	C_0	C_1	C_2	Δm (GeV)	χ^2/d.o.f.
32I	0.330	0.218	$-0.036(09)$	0.018(06)	0.025(06)	0.350(121)	1.26(5)
48I	0.207	0.051	$-0.088(29)$	0.062(18)	0.072(23)	0.637(250)	1.04(7)

From the combined fit Eqs. (6.1) and (6.2), it is seen that when Δm is large, C_0 should be constant and the data points for different source-sink separation should
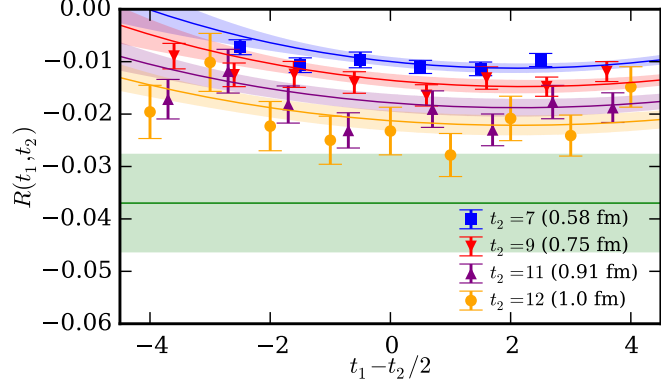
(a) Two-states 3pt/2pt ratio fit
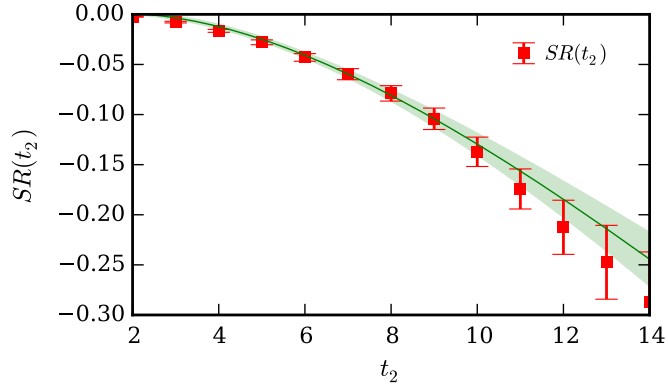
(b) Summed ratio fit

Figure 6.1: Combined correlated two-states fit of the 32I ensemble 3pt/2pt-ratio and summed ratio data. The transparent bands show the fit results based on the fit parameters in Eqs. (6.1) and (6.2) listed in Table 6.1. The green bands in the above figures show the final fit result of the disconnected light-quarks magnetic form factor $G_M^{\text{light-sea}}(Q^2)$ at $Q^2 = 0.218 \text{ GeV}^2$.

have overlap amongst themselves or the separation between them should be very small. A comparison between the fit values of Δm in Table 6.1 and FIGS. 6.1, 6.2 shows the agreement with this. It is seen from FIG. 6.1 that a smaller value of Δm is consistent with the well separated data points with different sink-source separations on the 32I ensemble. One can see from FIG. 6.2 and $\Delta m = 0.637(250) \text{ GeV}$ from Table 6.1 that a larger value of the energy gap is consistent with the overlapping data points at different t_2 and therefore, the final fit result is closer to the plateau region of the data points at source-sink separation $t_2 = 9$ of the 48I ensemble lattice data.
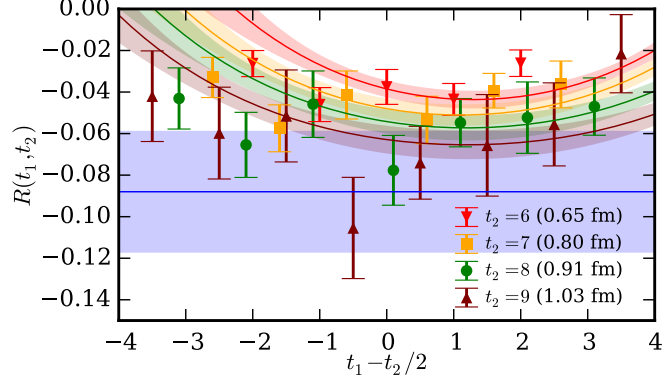
(a) Two-states 3pt/2pt ratio fit
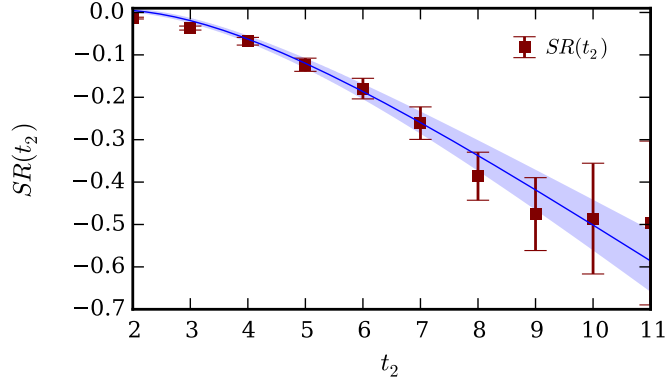
(b) Summed ratio fit

Figure 6.2: Combined correlated two-states fit of the 48I ensemble 3pt/2pt-ratio and summed ratio data. The transparent bands show the fit results based on the fit parameters in Eqs. (6.1) and (6.2) listed in Table 6.1. The blue bands in the above figures show the final fit result of the disconnected light-quarks magnetic form factor $G_M^{\text{light-sea}}(Q^2)$ at $Q^2 = 0.051$ GeV^2.

We perform similar combined correlated two-states fits to obtain the DI Sachs electric form factor and ensure that the fit window is as large as possible; in most cases the $\chi^2/$d.o.f is in the vicinity of $0.9-1.1$. We choose the largest possible fit window as long as goodness of the fit is ensured and one can obtain a reasonable signal-to-noise ratio in the fits.

6.4 Extraction of the DI magnetic moment and charge radius

We have discussed in Section 6.4 why we use model-independent z-expansion fit instead of dipole fit to extrapolate strange quark magnetic moment and charge radius. Another reason we do not use the dipole fit in the calculation is because the Q^2 behaviors of the disconnected light and strange form factors are unknown and one would prefer not to be biased with a specific form of the extrapolation. (There exist also other phenomenological models for the Q^2-dependence of strange form factors, for example in Ref. [86].) Therefore we adopt the model-independent z-expansion fit as described below. We take $t_{\text{cut}} = 4m_\pi^2$ for fitting the disconnected light quarks FF and $t_{\text{cut}} = 4m_K^2$ for the strange quark FF. We have verified that a different choice of t_{cut} such as $9m_\pi^2$ has less than a few percent effect on our extrapolations.

In FIG. 6.3, we show three examples of the extractions of light-sea-quarks magnetic moment at $Q^2 = 0$ from the FF data at different Q^2 using the z-expansion fit:

$$G_{E,M}^{q,z-exp}(Q^2) \;\; = \;\; \sum_{k=0}^{k_{\text{max}}} a_k z^k, \tag{6.3}$$

where

$$z \;\; = \;\; \frac{\sqrt{t_{\text{cut}} + Q^2} - \sqrt{t_{\text{cut}}}}{\sqrt{t_{\text{cut}} + Q^2} + \sqrt{t_{\text{cut}}}}.$$

We see from FIG. 6.3 and also from our previous work [29] that the lattice data of 48I ensemble is quite a bit noisier than the 24I and 32I ensemble data. Therefore we show in FIGS. 6.3b and 6.3c two examples of how we extract the light-sea and strange quarks contributions to the nucleon magnetic moment by performing simulation around the physical pion mass $m_\pi \in (0.135, 0.150)$ GeV.

As discussed in our previous work [29], we keep the first 3-terms $i.e.$ $k = 0, 1, 2, 3$ in the z-expansion formula (6.3) and perform the Q^2-extrapolation. Unlike for the strange quark magnetic moment extraction in [29], for the light-sea-quarks magnetic moment, constraining a_2 with a prior width of $2 \times |a_{2,\text{avg}}|$ does not have any effect

since the uncertainties in the fit values of a_2 are already smaller than $2 \times |a_{2,\mathrm{avg}}|$ for most all of the pion masses. Therefore we do not set any prior on a_2 for the extraction of the magnetic moments. However, for the extraction of the charge radii, we calculate the jackknife ensemble average $a_{2,\mathrm{avg}}$ of the coefficient a_2 in formula (6.3) and then perform another fit by setting a_2 centered at $a_{2,\mathrm{avg}}$ with a prior width equal to $2 \times |a_{2,\mathrm{avg}}|$. We find that the effect of setting this prior is almost insignificant for the 24I and 32I ensemble data, especially at heavier quark masses. However, the prior stabilizes the extrapolation of $G_E^q(Q^2)$ for pion masses around the physical point for the 48I ensemble. Since the z-expansion method guarantees that a_k coefficients are bounded in size and that higher order a_k's are suppressed by powers of z^k, we carefully check the effect of the a_3 coefficient in our fit formula and estimate this effect to calculate the systematic uncertainties in the z-expansion fits. We calculate the difference in the central values of $G_M^q(0)$ with and without the addition of the a_3 term in the z-expansion formula (6.3) for the lightest quark masses at the unitary point for each lattice ensemble. We find the addition of the a_3-term in the z-expansion after we constrain a_2 has the largest effect, as expected, for the quark mass equivalent to $m_\pi \sim 140$ MeV of the 48I ensemble and obtain the difference in the central value of $G_M^{\mathrm{light\text{-}sea}}(0)$ to be about 11%. Therefore, we take a conservative approach and estimate a systematic error of 11% of the final continuum value of $G_M^q(0)$ obtained from the global fit.

Similarly, one can extract light-sea and strange quarks contributions to the nucleon charge radius by calculating the slope of $G_E^q(Q^2)$ near $Q^2 = 0$. We find that adding the a_3 term in the z-expansion has a larger effect on calculating the charge radius than in extracting the magnetic moment and such an effect of adding the a_3 term for the charge radius calculation is $12 - 20\%$. Therefore a 20% uncertainty has been added to the systematics in the global fit of charge radius as a part of our conservative assessment. One important observation from FIG. 6.4 is that although the data of
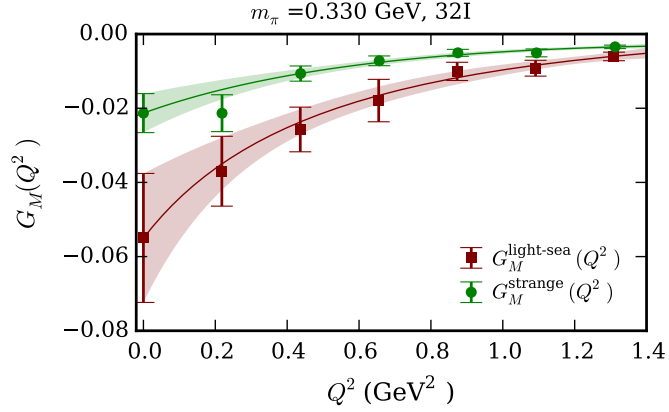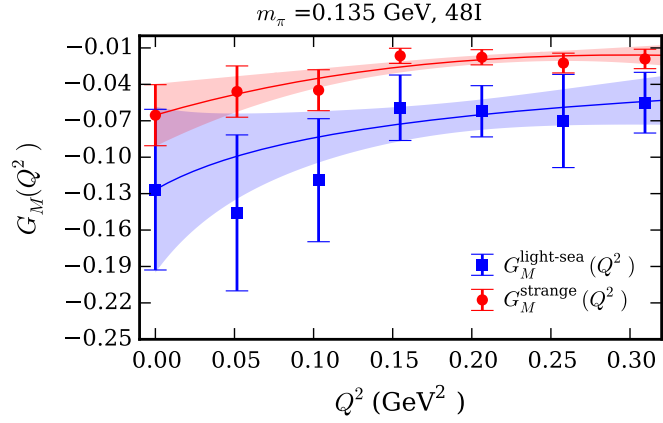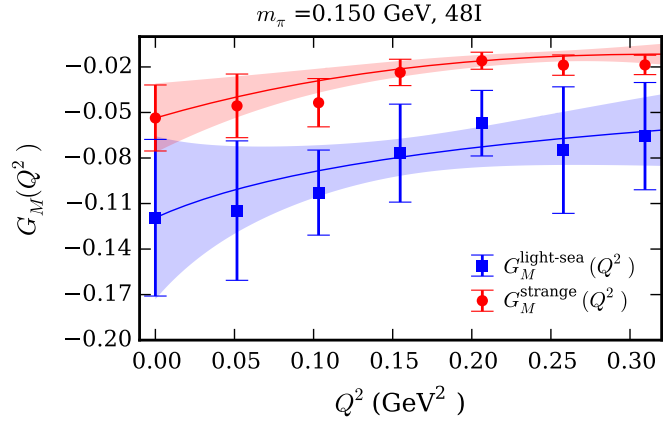
Figure 6.3: Light-sea and strange-quark magnetic moment $G_M^{\text{light-sea, strange}}(0)$ extrapolation for three different quark masses of the 32I (FIG. 6.3a) and 48I (FIGS. 6.3b, 6.3c) ensembles using z-expansion from the lattice $G_M^{\text{light-sea, strange}}(Q^2)$. The χ^2/d.o.f. for the extrapolations are in the range of $0.52 - 0.88$. Charge factors are not included in the form factors.
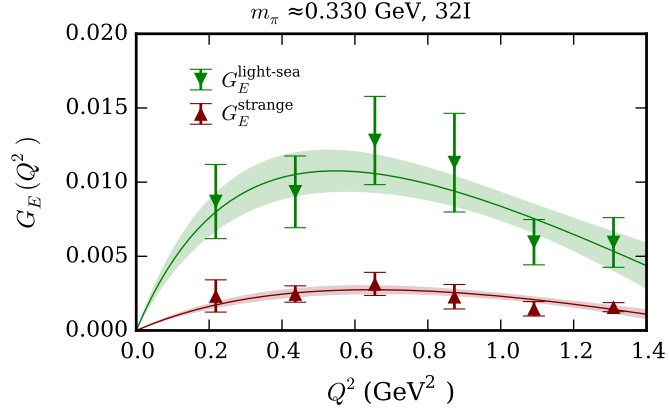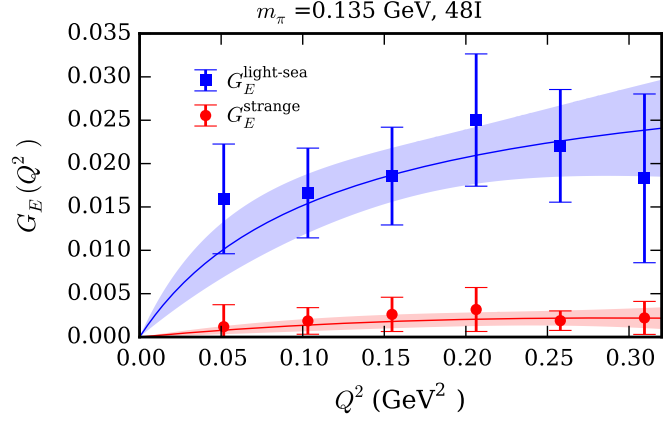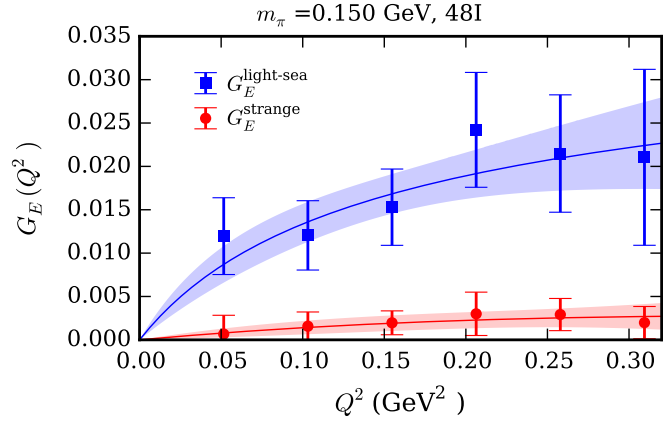
Figure 6.4: Light-sea and strange quarks contributions to the nucleon electric FF $G_E^{\text{light-sea/strange}}(Q^2)$ for two different quark masses of the 32I (FIG. 6.4a) and 48I (FIGS. 6.4b, 6.4c) ensembles. The $\chi^2/\text{d.o.f.}$ for the two fits are in the range of $0.49 - 0.81$. Charge factors are not included in the form factors.

light quark electric FF are not very precise, nevertheless the uncertainty band of the z-expansion is narrower compared to the magnetic FF extrapolation. The reason is due to charge conservation as the disconnected $G_E^q(Q^2)$ is constrained to be 0 at $Q^2 = 0$. Another important observation from FIG. 6.4 is that the disconnected-sea light quarks contribution to the $G_E^{\text{light-sea}}(Q^2)$ is almost $6-10$ times larger than the strange quark contribution $G_E^s(Q^2)$.

6.5 Global fits of the disconnected insertions of nucleon properties

With the extrapolated results from the z-expansion in hand, we now have 24 data points for the magnetic moments and charge radii calculated from the slopes near $Q^2 = 0$ of the electric FFs. For the empirical global fit formula of the light-sea-quarks magnetic moment, we employ chiral extrapolation similar to the form we have used in Ref. [29] to obtain strange quark magnetic moment and volume extrapolation from Ref. [90]. Since overlap fermion action is already $\mathcal{O}(a)$ improved, therefore, we apply an $\mathcal{O}(a^2)$ correction to the global fit formula:

$$G_M^{\text{light-sea}}(Q^2 = 0, m_\pi, m_K, m_{\pi,vs}, a, L) = A_0 + A_1 \, m_\pi + A_2 \, m_K$$
$$+ A_3 \, a^2 + A_4 \, m_\pi (1 - \frac{2}{m_\pi \, L}) \, e^{-m_\pi L} \tag{6.4}$$

where $m_\pi \, (m_K)$ is the valence pion (kaon) mass, and m_N is the nucleon mass. We show the extrapolation of the nucleon disconnected-sea light quarks magnetic moment in FIG. 6.5. At the physical point and in the limit, $i.e.$ $a \to 0$ and $L \to \infty$, we obtain

$$G_M^{\text{light-sea}}(0)\Big|_{\text{physical}} = -0.129(30)(13)(18) \, \mu_N \,, \tag{6.5}$$

where the magnetic moment is measured in the unit of nucleon magneton (μ_N). The first uncertainty in the value of the the magnetic moment in Eq. (6.5) comes from the statistics, the second uncertainty comes from adding the higher order a_3-term in the z-expansion and the third uncertainty comes from the variation of the central

value in the global fit formula with the introduction of additional terms. The parameter values we obtain according the global fit are: $A_1 = 0.38(12)$, $A_2 = -0.40(16)$, $A_3 = 0.30(39)$, $A_4 = -1.26(2.75)$. An attempt to add a partial quenching term $m_{\pi,vs}^2 = 1/2(m_\pi^2 + m_{\pi,ss}^2) + a^2\Delta_{\mathrm{mix}}$ with $m_{\pi,ss}$ the pion mass corresponding to the sea quark mass in the global fit formula does not describe our lattice data well and the fit parameters A_1, A_2 do not have any signal in this case. Therefore we did not include the partial quenching term to obtain $G_M^{\mathrm{light\text{-}sea}}(0)\big|_{\mathrm{physical}} = -0.129(30)(13)(18)\,\mu_N$ in Eq. (6.5). With the partial-quenching term included, one obtains $G_M^{\mathrm{light\text{-}sea}}(0)\big|_{\mathrm{physical}} = -0.147(33)\,\mu_N$. However, we include the second systematic error in our final result due to the possible inclusion of this partial quenching term in the global fit (6.4).

Figure 6.5: Light-sea-quark magnetic moment at 24 quark masses on 24I, 32I, 48I, and 32ID ensembles as a function of the pion mass. The curved blue line in the figure shows the behavior in the infinite volume and continuum limit. The cyan band shows the combined statistical (blue band) and systematic uncertainties added in quadrature. The $\chi^2/\mathrm{d.o.f.}$ of the fit is 0.67.

In Sec. 6.4, we have obtained light-sea-quarks contribution to the charge radii using the z-expansion method by calculating the slope of $G_E^{\mathrm{light\text{-}sea}}(Q^2)$ using the following definition:

$$\langle r_{\mathrm{light\text{-}sea}}^2 \rangle_E \equiv -6 \left.\frac{dG_E^{\mathrm{light\text{-}sea}}}{dQ^2}\right|_{Q^2=0} \tag{6.6}$$

Using the charge radius values at 3 different volumes and lattice spacings and 24 valence-quark masses from four ensembles, we perform a simultaneous continuum and chiral extrapolation to obtain the final value of the charge radius using the following global fit formula:

$$\langle r^2_{\text{light-sea}}\rangle_E (m_\pi, m_{\pi,vs}, m_K, a, L) = A_0 + A_1 \log(m_\pi) + A_2\, m_\pi^2 + A_3\, m_{\pi,vs}^2$$
$$+ A_4\, a^2 + A_5\, \sqrt{L}\, e^{-m_\pi L}. \tag{6.7}$$

The chiral extrapolation in the empirical formula (6.7) has been adopted from [89] by replacing m_K with m_π and the volume correction similar to the pion charge radius correction has been obtained from [93]. In the continuum limit, we obtain

$$\langle r^2_{\text{light-sea}}\rangle_E \big|_{\text{physical}} = -0.061(16)(11)(10)\,\text{fm}^2, \tag{6.8}$$

and the fit parameters are: $A_1 = 0.077(24)$, $A_2 = -0.280(99)$, $A_3 = 0.151(100)$, $A_4 = -0.015(13)$, and $A_5 = -0.054(58)$. The extraction of the charge radius from the FFs is sensitive to the lowest value of Q^2 and momentum transfer range of the data used, and also on the form of the fit. However, one wants to go to very low Q^2-values to extract the charge radii and the 48I ensemble has the lowest momentum transfer which is almost 4 times smaller than those of the 24I and 32I lattice data. Though the uncertainty in the charge radii obtained from 48I ensemble are large compared to the 24I and 32I ensemble results, an addition of the coarse lattice with larger volume and the lowest $Q^2 \sim 0.07\,\text{GeV}^2$ indeed shows that the slope of the electric FF calculated near $Q^2 = 0$ is consistent with the charge radii obtained from the 48I lattice data. Our results clearly demonstrate the necessity of performing lattice simulations at or near the physical pion masses while of course keeping in mind that one requires significant improvements in the statistical precision and a better control on the determination of the excited-states effect.
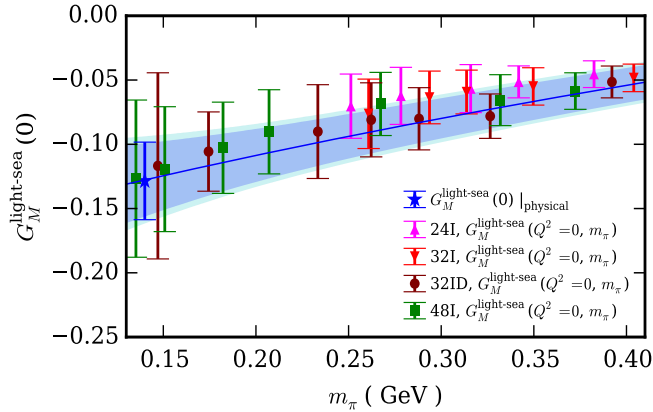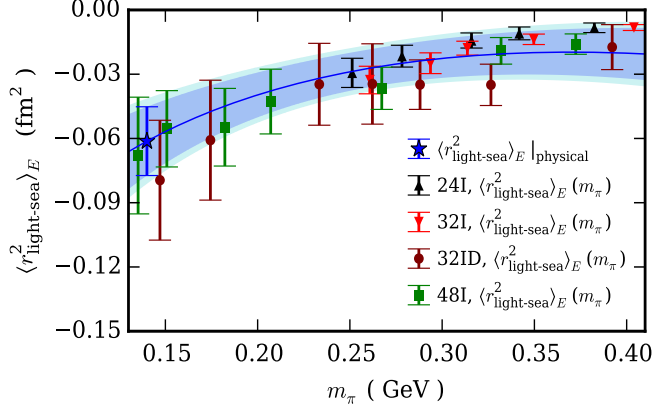
Figure 6.6: Light-sea-quark charge radius at 24 quark masses on 24I, 32I, 48I, and 32ID ensembles as a function of the pion mass. The curved blue line in the figure shows the behavior in the infinite volume and continuum limit. The cyan band shows the combined statistical (blue band) and systematic uncertainties added in quadrature. The χ^2/d.o.f. of the fit is 0.46.

It is important to note that the magnetic moment and charge radius results in Eqs. (6.5) and (6.8) do not include charge factors. We define the magnetic moment in the unit of nucleon magneton as μ_M and the charge radius as $\langle \rho^2 \rangle_E$ with the proper charge factors included. After including the charge factors and using the results from [29] and Eqs. (6.5), (6.8) we obtain

$$
\begin{aligned}
\mu_M^{\text{s}} &= -\frac{1}{3}G_M^s(0) \\
&= 0.021(5)(3)\,\mu_N, & (6.9) \\
\mu_M^{\text{light-sea}} &= \left(\frac{2}{3} - \frac{1}{3}\right)G_M^{\text{light-sea}}(0) \\
&= -0.043(10)(08)\,\mu_N, & (6.10) \\
\langle \rho_{\text{s}}^2 \rangle_E &= = -\frac{1}{3}\langle r_{\text{s}}^2 \rangle_E \\
&= 0.0014(05)(05)\,\text{fm}^2, & (6.11) \\
\langle \rho_{\text{light-sea}}^2 \rangle_E &= \left(\frac{2}{3} - \frac{1}{3}\right)\langle r_{\text{light-sea}}^2 \rangle_E \\
&= -0.0203(53)(49)\,\text{fm}^2. & (6.12)
\end{aligned}
$$

Combining results with the strange quark magnetic moment and charge radius, we

obtain the total contribution from the disconnected-sea light and strange quarks to the nucleon magnetic moment and charge radius:

$$\mu_M^{\text{sea}} = -0.022(11)(09)\,\mu_N, \tag{6.13}$$

$$\langle \rho_{\text{sea}}^2 \rangle_E = -0.019(05)(05)\,\text{fm}^2. \tag{6.14}$$

Comparing with the PDG values of nucleon magnetic moments [23], our results indicate that disconnected-sea quarks contribute $\sim 1\%$ to the nucleon magnetic moments, namely, a negative $0.8(5)\%$ and a $1.2(7)\%$ to the proton and neutron magnetic moments, respectively. Keeping in mind that there is a 4% discrepancy between the measurement of proton charge radius from the muonic Lamb shift experiment and the electron-proton scattering experiments, our finding in the present work reveals that the lattice calculation of the DI gives a negative $2.5(9)\%$ contribution to the proton charge radius. This is about half of the discrepancy between those measured in the electron-proton scattering and the muonic atom. Thus, it is important to have the DI included when the lattice calculation of the proton charge radius is carried out. Although a complete lattice QCD calculation including the connected and disconnected insertions at the physical point is required to draw any profound conclusion about the accurate percentage of the disconnected-sea quarks contribution to proton charge radius, this calculation clearly indicates that there will be a shift towards a smaller value of the proton charge radius when the disconnected-sea light quarks contribution is included. However, the disconnected-sea quarks contribution to the neutron charge radius can have a significant effect, namely $16.3(6.1)\%$ compared to the experimental neutron charge radius, in obtaining the value closer to the experimental value.

From the z-expansion fit parameters in Sec. 6.4, we can now interpolate the light-sea and strange quarks contributions to the nucleon electromagnetic form factors. Although the largest available momentum transfer we have on the 24I and 32I ensemble is $Q^2 \sim 1.3$ GeV^2, the largest momentum transfer available on the 48I en-

semble is $Q^2 \sim 0.5$ GeV^2. Therefore, we note that the extrapolation of the nucleon EMFF leads to uncontrolled error bars after $Q^2 \sim 0.5$ GeV^2 for the 48I ensemble and we constrain the extrapolations of the 48I ensemble EMFF up to $Q^2 = 0.5$ GeV^2. The global fit results of the strange quark EMFFs have been obtained from [110] and we use similar empirical formulas as Eqs. (6.4), (6.7) to estimate the light-sea quarks contribution to the nucleon EMFF in the continuum limit and at the physical point. We present the results in FIG. 6.7 with systematics included and also include charge factors in the form factor calculations so that the sign and magnitude of the disconnected-quarks contributions to the nucleon EMFFs can directly be compared to the nucleon total EMFFs. These results will be combined with the connected insertion calculation of the nucleon EMFFs in our future work to obtain a complete description of the nucleon EMFF from first-principles calculation.
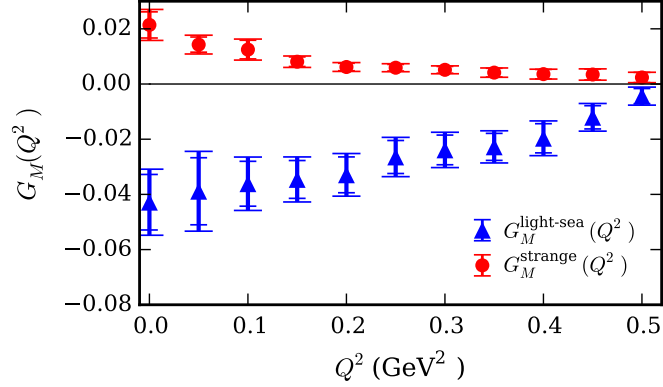
(a) Two-states 3pt/2pt ratio fit
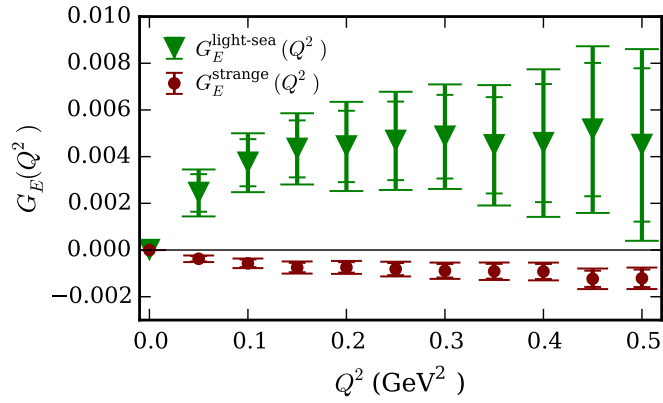
(b) Summed ratio fit

Figure 6.7: Disconnected-sea light and strange quarks contributions to the nucleon electromagnetic form factors at the physical point and in the continuum limit. Charge factors are included in the form factor calculations. The outer error bars in the data points include the systematic uncertainties in the calculations.

6.6 Conclusion

In this calculation, we have uncovered the practical importance of including the disconnected quark loops contribution to the nucleon magnetic moment and charge radius. In particular, in accord with the analysis, we find that the disconnected-sea light and strange quarks contribution to the nucleon charge radius can have an important impact to reconcile the lattice QCD estimates with the experimental measurements. A negative 2.5(9)% contribution to the proton charge radius from the disconnected-sea quarks should have an impact on the 'proton charge radius puz-

zle' where the discrepancy at 4% is of the same order. It is seen for the first time that the disconnected quarks can shift the neutron charge radius calculation towards the experimental value by about 16%. Especially, because the neutron electric form factor calculation on the lattice is noisy and the valence-only quark contribution is smaller than the experimental Q^2 behavior, the disconnected quark loops cannot be ignored for a better estimation of the neutron form factors at low Q^2 on the lattice. Our main focus of this calculation was to show that 1) the disconnected-sea quarks contribution to the nucleon properties at low Q^2 is of significant importance and 2) numerical simulation with controlled systematics and near the physical pion mass can generate a better theoretical understanding of various nucleon properties.

Chapter 7 Summary and Outlook

We have calculated light and strange disconnected-sea quark contribution to the nucleon electromagnetic form factors at the physical point and in the continuum limit. The calculated form factors in the momentum transfer range of $0 \leq Q^2 \leq 0.5$ GeV^2 are the most precise and accurate calculations of the disconnected-sea quarks contribution to the nucleon electromagnetic form factors.

To give a complete description of the nucleon electromagnetic form factors, a calculation of the valence quark contribution to the nucleon electromagnetic form factors is required. This calculation is in progress and technical state of arts and computational resources limit this calculation at present. While we have obtained some results of the connected insertion calculation at heavier pion masses, a future connected insertion calculation on the 48I ensemble at the physical pion mass will allow us to perform a simultaneous chiral interpolation, infinite volume and continuum extrapolation in a global fit.

Chapter 8 Appendix

8.1 Appendix A: Chapter 3 Supplement

8.1.1 Pauli matrix convention

Pauli matrices in Pauli-Sakurai convention are:

$$\gamma_i = \begin{pmatrix} 0 & -i\sigma_i \\ i\sigma_i & 0 \end{pmatrix} \tag{8.1}$$

$$\gamma_4 = \begin{pmatrix} \mathbb{1} & 0 \\ 0 & -\mathbb{1} \end{pmatrix} \tag{8.2}$$

$$\gamma_5 = \begin{pmatrix} 0 & -\mathbb{1} \\ -\mathbb{1} & 0 \end{pmatrix} \tag{8.3}$$

The polarized and unpolarized projection operators are written in terms of these Pauli matrices are as follows

$$\begin{aligned} \Gamma_i &= (-i)\frac{1 \pm \gamma_4}{2}\gamma_i\gamma_5 \\ \Gamma_4 &= \frac{1 \pm \gamma_4}{2} \end{aligned} \tag{8.4}$$

8.1.2 Pauli-Sakurai convention for gamma matrices

$$\{\gamma_\mu, \gamma_\nu\} = 2\delta_{\mu\nu} \tag{8.5}$$

$$\gamma_\mu^\dagger = \gamma_\mu \tag{8.6}$$

which implies that

$$\gamma_\mu^* = \gamma_\mu^T$$

where $\mu, \nu = 1,2,3,4$

$$\{\gamma_5, \gamma_\mu\} = 0 \tag{8.7}$$

$$\gamma_5 = \gamma_1 \gamma_2 \gamma_3 \gamma_4 = \frac{1}{4!} \epsilon_{\mu\nu\lambda\sigma} \gamma_\mu \gamma_\nu \gamma_\lambda \gamma_\sigma \tag{8.8}$$

$$\gamma_5^\dagger = \gamma_5$$

$$\gamma_5^2 = 1 \tag{8.9}$$

8.1.3 Charge conjugation

$$C\psi(x)C^{-1} = C\overline{\psi}^T(x)$$

$$C\overline{\psi}(x)C^{-1} = \psi^T(x)C^{-1} \tag{8.10}$$

$$CU_\mu(x)C^{-1} = U_\mu^*(x)$$

where

$$C = \gamma_2 \gamma_4 \tag{8.11}$$

C has the following properties

$$C = -C^{-1} \tag{8.12}$$

$$C = -C^T$$

$$(C^{-1})^T = -C^{-1}$$

$$C\gamma_\mu C^{-1} = -\gamma_\mu^* \tag{8.13}$$

$$C\gamma_5 \gamma_\mu \gamma_5 C^{-1} = \gamma_\mu^*$$

$$\gamma_5 C^{-1} \gamma_\mu C \gamma_5 = \gamma_\mu^*$$

Now define

$$(C\gamma_5)(\alpha\beta) \equiv \tilde{C}(\alpha\beta) \tag{8.14}$$

$$
\begin{aligned}
\tilde{C}^\dagger(\alpha\beta) &= \left(\gamma_5^\dagger \gamma_4^\dagger \gamma_2^\dagger\right)(\alpha\beta) \\
&= (\gamma_5\gamma_4\gamma_2)(\alpha\beta) \\
&= (\gamma_4\gamma_2\gamma_5)(\alpha\beta) \\
&= -(\gamma_2\gamma_4\gamma_5)(\alpha\beta) \\
&= -\tilde{C}(\alpha\beta) \tag{8.15}
\end{aligned}
$$

8.1.4 Nucleon interpolation fields

A hadron interpolator is a functional of the lattice fields with the quantum numbers of the state one is interested in. Once the interpolators are identified we consider the Euclidean correlator of the hadron interpolators. These are by construction, gauge-invariant color singlets. The interpolation fields are chosen in such a way that they have a good overlap with the ground-state of the nucleon.

Consider interpolators of spin 1/2 nucleon:

$$
\begin{aligned}
\chi_1(\gamma x) &= \epsilon_{abc}\left(u^T(a\alpha x)(C\gamma_5)(\alpha\beta)d(b\beta x)\right)u(c\gamma x) \\
&= -\epsilon_{abc}u^T(c\alpha x)(C\gamma_5)(\alpha\beta)d(b\beta x)u(a\gamma x) \\
&= \epsilon_{abc}u^T(b\alpha x)(C\gamma_5)(\alpha\beta)d(c\beta x)u(a\gamma x) \\
&= \epsilon_{abc}u(a\gamma x)u^T(b\alpha x)(C\gamma_5)(\alpha\beta)d(c\beta x) \\
&= \epsilon_{abc}u_\gamma^a(\vec{x},t)\left(u^b(\vec{x},t)^T(C\gamma_5)d^c(\vec{x},t)\right) \tag{8.16}
\end{aligned}
$$

Where a, b, c are color indices and α, β, γ are Dirac indices. The wave functions for up and down quarks are denoted by u and d respectively. Note that, the baryon interpolator χ has an open Dirac index (here γ)- because it describes fermion after

all. Using Eq. (8.12),

$$
\begin{aligned}
\bar{\chi}_1(\gamma x) &= -\epsilon_{abc}\bar{u}(a\gamma x)\bar{d}(b\beta x)(C\gamma_5)(\beta\alpha)\bar{u}(c\alpha x) \\
&= \epsilon_{abc}\bar{u}(a\gamma x)\bar{d}(b\beta x)(\gamma_5 C^{-1})(\beta\alpha)\bar{u}(c\alpha x) \\
&= \epsilon_{abc}\bar{u}_\gamma^a(\vec{x},t)\left(\bar{d}^b(\vec{x},t)(\gamma_5 C^{-1})\bar{u}^c(\vec{x},t)^T\right) \quad (8.17)
\end{aligned}
$$

For example, The creation interpolating field defined $\bar{\chi}_\gamma(x_0)$ in Eq. (8.17) created a state with the quantum number of a proton out of the vacuum at a Euclidean space-time point x_0. This state then evolves to another spacetime point x and annihilates by the operator $\chi_\gamma(x)$ at spacetime point x.

The second choice of the nucleon interpolation field can be written as'

$$
\chi_2(\delta x) = \epsilon_{abc}[u^T(a\alpha x)C(\alpha\beta)d(b\beta x)]\gamma_5(\delta\gamma)u(c\gamma x) \quad (8.18)
$$

Therefore,

$$
\begin{aligned}
\chi_2^\dagger(\delta x) &= \epsilon_{abc}u^\dagger(c\gamma x)\gamma_5^\dagger(\delta\gamma)[d^\dagger(b\beta x)C^\dagger(\alpha\beta)u^{T\dagger}(a\alpha x)] \\
&= -\epsilon_{abc}u^\dagger(c\gamma x)\gamma_5(\delta\gamma)[d^\dagger(b\beta x)C^\dagger(\alpha\beta)u^{T\dagger}(a\alpha x)] \\
&= -\epsilon_{abc}u^\dagger(c\gamma x)\gamma_5(\delta\gamma)[d^\dagger(b\beta x)\gamma_4\gamma_4 C^\dagger(\alpha\beta)u^{T\dagger}(a\alpha x)] \\
&= -\epsilon_{abc}u^\dagger(c\gamma x)\gamma_5(\delta\gamma)[d^\dagger(b\beta x)\gamma_4 C^\dagger(\alpha\beta)\gamma_4 u^{T\dagger}(a\alpha x)] \quad (8.19)
\end{aligned}
$$

Therefore,

$$
\begin{aligned}
\bar{\chi}_2(\delta x) &= \chi_2^\dagger(\delta x)\gamma_4 \\
&= -\epsilon_{abc}u^\dagger(c\gamma x)\gamma_5(\delta\gamma)[d^\dagger(b\beta x)\gamma_4 C(\alpha\beta)\gamma_4 u^{T\dagger}(a\alpha x)]\gamma_4 \\
&= -\epsilon_{abc}u^\dagger(c\gamma x)\gamma_4\gamma_5(\delta\gamma)[d^\dagger(b\beta x)\gamma_4 C(\alpha\beta)\gamma_4 u^{T\dagger}(a\alpha x)] \\
&= -\epsilon_{abc}\bar{u}(c\gamma x)\gamma_5(\delta\gamma)[\bar{d}(b\beta x)C(\alpha\beta)\bar{u}^T(a\alpha x)], \quad (8.20)
\end{aligned}
$$

where in the third line we have used

$$
\begin{aligned}
\gamma_5 C \gamma_4 &= \gamma_5 \gamma_2 \gamma_4 \gamma_4 \\
&= -\gamma_5 \gamma_4 \gamma_2 \gamma_4 \gamma_4 \\
&= \gamma_4 \gamma_5 \gamma_2 \gamma_4 \gamma_4 \\
&= \gamma_4 \gamma_2 C
\end{aligned}
\tag{8.21}
$$

The third choice of nucleon interpolation field can be written as

$$
\chi_3(\gamma x) = \epsilon_{abc}[u^T(a\alpha x)(C\gamma_5\gamma_4)(\alpha\beta)d(b\beta x)]u(c\gamma x)
\tag{8.22}
$$

Again,

$$
\begin{aligned}
\bar{\chi}_3(\gamma x) &= \chi_3^\dagger(\gamma x)\gamma_4 \\
&= -\epsilon_{abc}u^\dagger(c\gamma x)[\bar{d}(b\beta x)(C\gamma_5\gamma_4)(\alpha\beta)\bar{u}^T(a\alpha x)]\gamma_4 \\
&= -\epsilon_{abc}u^\dagger(c\gamma x)\gamma_4[\bar{d}(b\beta x)(C\gamma_5\gamma_4)(\alpha\beta)\bar{u}^T(a\alpha x)] \\
&= -\epsilon_{abc}\bar{u}(c\gamma x)[\bar{d}(b\beta x)(C\gamma_5\gamma_4)(\alpha\beta)\bar{u}^T(a\alpha x)]
\end{aligned}
\tag{8.23}
$$

Therefore, in general, we can write the nucleon interpolation fields as the following

$$
\chi_i(\delta x) = \epsilon_{abc}[u^T(a\alpha x)\Gamma_1(\alpha\beta)d(b\beta x)]\Gamma_2(\delta\gamma)u(c\gamma x),
\tag{8.24}
$$

$$
bar\chi_i(\delta x) = -\epsilon_{abc}\bar{u}(c\gamma x)\Gamma_2(\delta\gamma)[\bar{d}(b\beta x)\Gamma_1(\alpha\beta)\bar{u}^T(a\alpha x)],
\tag{8.25}
$$

where, $i, j = 1, 2, 3$ and δ is the free Dirac index for the fermion.

$$
\begin{aligned}
\chi_1, \quad \bar{\chi}_1 \quad &: \quad \Gamma_1 = C\gamma_5 \quad \text{and} \quad \Gamma_2 = 1 \\
\chi_2, \quad \bar{\chi}_2 \quad &: \quad \Gamma_1 = C \quad \text{and} \quad \Gamma_2 = \gamma_5 \\
\chi_3, \quad \bar{\chi}_3 \quad &: \quad \Gamma_1 = C\gamma_5\gamma_4 \quad \text{and} \quad \Gamma_2 = 1
\end{aligned}
\tag{8.26}
$$

8.1.5 Normalization

The normalization condition in the continuum is defined as

$$\langle 0| \, |0\rangle + \sum_n \int \frac{d^3\vec{p}}{(2\pi)^3 \, (2E_p)} \, |n,\vec{p}\rangle \, \langle n,\vec{p}| = 1. \tag{8.27}$$

where

$$\langle n,\vec{p}\,|\, m,\vec{p}'\rangle = (2\pi)^3 (2E_p^n)\delta_{n,m}\delta^3(\vec{p}-\vec{p}') \tag{8.28}$$

On the lattice, the discrete version of this normalization condition is

$$\langle 0| \, |0\rangle + \sum_{n,\vec{p}} \frac{1}{(La)^3(2E_p)} \, |n,\vec{p}\rangle \, \langle n,\vec{p}| = 1. \tag{8.29}$$

where

$$\langle n,\vec{p}\,|\, m,\vec{p}'\rangle = (La)^3 (2E_p^n)\delta_{n,m}\delta_{\vec{p},\vec{p}'} \tag{8.30}$$

8.1.6 Dirac Equation

$$
\begin{aligned}
(\slashed{p} - m)u(p,s) = 0 \quad &\rightarrow \quad (-i\slashed{p}_E - m)u_E(p,s) = 0 \\
&\Rightarrow \quad (i\slashed{p}_E + m)u_E(p,s) = 0 \\
&\text{or,} \quad (-i)(i\slashed{p}_E + m)u_E(p,s) = 0 \\
&\Rightarrow \quad (\slashed{p}_E - im)u_E(p,s) = 0
\end{aligned}
\tag{8.31}
$$

and

$$
\begin{aligned}
\bar{u}(p,s)(\slashed{p} - m) = 0 \quad &\rightarrow \quad \bar{u}_E(p,s)(i\slashed{p}_E + m) = 0 \\
&\Rightarrow \quad \bar{u}_E(p,s)(\slashed{p}_E - im) = 0.
\end{aligned}
\tag{8.32}
$$

$$u_M(p,s) = \sqrt{\frac{E+m}{2m}}\begin{pmatrix} I \\ \frac{\vec{\sigma}\cdot\vec{p}}{E+m} \end{pmatrix}\chi(s) \rightarrow u_E(p,s) = \sqrt{\frac{-ip_4+m}{2m}}\begin{pmatrix} I \\ \frac{\vec{\sigma}\cdot\vec{p}_E}{-ip_4+m} \end{pmatrix}\chi(s) \tag{8.33}$$

$$\bar{u}_E(p,s) = u^\dagger \gamma_4 = \sqrt{\frac{-ip_4 + m}{2m}} \chi^\dagger(s) \left(I \qquad (-1)\frac{\vec{\sigma} \cdot \vec{p}_E}{-ip_4 + m} \right) \tag{8.34}$$

$$
\begin{aligned}
\bar{u}_E(p,s) u_E(p,s') &= \delta_{s,s'} \\
\bar{u}_E(p,s) \gamma_\mu u_E(p,s') &= \frac{-ip_\mu^E}{m} \delta_{s,s'} \\
\sum_s u_E(p,s) \bar{u}_E(p,s) &= \frac{-i\slashed{p}_E + m}{2m}.
\end{aligned} \tag{8.35}
$$

8.1.7 Matrix Elements

One replaces $\int \frac{d^3\vec{p}}{(2\pi)^3}$ by $\frac{1}{V}\sum_{\vec{p}}$ to go from continuum to discrete lattice,

$$\frac{d^3 p}{(2\pi)^3} \to \frac{1}{V}\sum_p, \qquad V = Na^3 \tag{8.36}$$

where N is the number of lattice sites and a is the lattice spacing. In the continuum, the overlaps between the interpolating fields are defined as

$$\text{Continuum: } \langle 0| \chi_\alpha(0) |\vec{p}, s, n, +\rangle = \phi_n^\dagger(p) \left(\frac{m_n^+}{NE_{p,n}^+} \right)^{\frac{1}{2}} u_\alpha(\vec{p}, s, n, +) \tag{8.37}$$

On the lattice,

$$
\begin{aligned}
|n, \vec{p}, s\rangle &= \sqrt{\frac{m}{VE_p}} |n, \vec{p}, s\rangle = \sqrt{\frac{m}{Na^3 E_p}} |n, \vec{p}, s\rangle \\
\psi_{\text{lattice}} &= a^{\frac{3}{2}} \psi_{\text{cont.}}, \\
j_{\text{lattice}} &= a^3 j_{\text{cont.}}
\end{aligned} \tag{8.38}
$$

Therefore, Eq. (8.37) can be written on the lattice as

$$\text{Euclidean: } \langle 0| \chi_\alpha(0) |\vec{p}, s, n, +\rangle = a^3 \phi_n^\dagger(p) \left(\frac{m_n^+}{NE_{p,n}^+} \right)^{\frac{1}{2}} u_\alpha^E(\vec{p}, s, n, +) \tag{8.39}$$

One can similarly write:

$$\text{Continuum: } \langle \vec{p}, s, n, +| \bar{\chi}_\alpha(0) |0\rangle = \bar{\phi}_n^\dagger(p) \left(\frac{m_n^+}{NE_{p,n}^+} \right)^{\frac{1}{2}} \bar{u}_\alpha(\vec{p}, s, n, +)$$

$$\text{Euclidean: } \langle \vec{p}, s, n, +| \bar{\chi}_\alpha(0) |0\rangle = a^3 \bar{\phi}_n^\dagger(p) \left(\frac{m_n^+}{NE_{p,n}^+} \right)^{\frac{1}{2}} \bar{u}_\alpha^E(\vec{p}, s, n, +)$$

$$\tag{8.40}$$

$$\text{Continuum: } \langle 0| \chi_\alpha(0) |\vec{p}, s, n, -\rangle = \phi_n^-(p) \left(\frac{m_n^-}{NE_{p,n}^-} \right)^{\frac{1}{2}} \gamma_5 u_\alpha(\vec{p}, s, n, -)$$

$$\text{Euclidean: } \langle 0| \chi_\alpha(0) |\vec{p}, s, n, -\rangle = \phi_n^-(p) a^3 \left(\frac{m_n^-}{NE_{p,n}^-} \right)^{\frac{1}{2}} (\gamma_5^E) u_\alpha^E(\vec{p}, s, n, -)$$

$$(8.41)$$

$$\text{Continuum: } \langle \vec{p}, s, n, -| \bar{\chi}_\alpha(0) |0\rangle = \phi_n^-(p) \left(\frac{m_n^-}{NE_{p,n}^-} \right)^{\frac{1}{2}} \bar{u}_\alpha(\vec{p}, s, n, -)(\gamma_5)$$

$$\text{Euclidean: } \langle \vec{p}, s, n, -| \bar{\chi}_\alpha(0) |0\rangle = a^3 \phi_n^-(p) \left(\frac{m_n^-}{NE_{p,n}^-} \right)^{\frac{1}{2}} \bar{u}_\alpha^E(\vec{p}, s, n, -) \gamma_5^E$$

$$(8.42)$$

Nucleon electromagnetic matrix elements for real and virtual photon can be written as

$$\langle \vec{p}', s', n', \pm| \mathcal{J}_\mu(x_0) |\vec{p}, s, n, \pm\rangle = \left(\frac{m_{n'}^\pm}{E_{p',n'}^\pm} \right)^{1/2} \left(\frac{m_n^\pm}{E_{p,n}^\pm} \right)^{1/2}$$
$$\bar{u}(\vec{p}', s', n', \pm) \mathcal{O}_{\mu,n',n}^{\pm,\pm} u(\vec{p}, s, n, \pm) \quad (8.43)$$

8.1.8 Techniques to Eliminate Negative Parity States at Source Side

$$\left(\frac{1 + \gamma_4}{2} \right) \left(\frac{-i\slashed{p}_- + m^-}{2m^-} \right) u(p, s, n, +) = \left(\frac{1}{2m^-} \right) (m^- + m_n^+ E_p^- - E_{p,n}^+)$$
$$\left(\frac{1 + \gamma_4}{2} \right) u(p, s, n, +)$$

$$\left(\frac{-i\slashed{p}_- + m^-}{2m^-} \right) \gamma_5 u(p, s, -) = 0$$

$$\bar{u}(p, s, n, +) \left(\frac{1 + \gamma_4}{2} \right) \left(\frac{-i\slashed{p}_- + m^-}{2m^-} \right) = \frac{1}{2m^-} (m^- + m_n^+ E_p^- - E_{p,n}^+)$$
$$\bar{u}(p, s, n, +) \left(\frac{1 + \gamma_4}{2} \right)$$

$$\bar{u}(p, s, -) \gamma_5 \left(\frac{-i\slashed{p}_- + m^-}{2m^-} \right) = 0$$

$$(8.44)$$

8.1.9 Miscellaneous Proofs and Relations

$$
\begin{aligned}
\sigma_{i4} &= \frac{1}{2i}[\gamma_i, \gamma_4] \\
&= \frac{1}{2i}(\gamma_i\gamma_4 - \gamma_4\gamma_i) \\
&= \frac{1}{2i}\left[\begin{pmatrix} 0 & -i\sigma_i \\ i\sigma_i & 0 \end{pmatrix}\begin{pmatrix} I & 0 \\ 0 & -I \end{pmatrix} - \begin{pmatrix} I & 0 \\ 0 & -I \end{pmatrix}\begin{pmatrix} 0 & -i\sigma_i \\ i\sigma_i & 0 \end{pmatrix}\right] \\
&= \frac{1}{2i}\left[\begin{pmatrix} 0 & i\sigma_i \\ i\sigma_i & 0 \end{pmatrix} - \begin{pmatrix} 0 & -i\sigma_i \\ -i\sigma_i & 0 \end{pmatrix}\right] \\
&= \begin{pmatrix} 0 & \sigma_i \\ \sigma_i & 0 \end{pmatrix}
\end{aligned}
\tag{8.45}
$$

$$
\begin{aligned}
\sigma_{i4} &= \frac{1}{2i}(\gamma_4\gamma_i - \gamma_i\gamma_4) \\
&= \frac{1}{2i}\left[\begin{pmatrix} 0 & -i\sigma_i \\ -i\sigma_i & 0 \end{pmatrix} - \begin{pmatrix} 0 & i\sigma_i \\ i\sigma_i & 0 \end{pmatrix}\right] \\
&= \begin{pmatrix} 0 & -\sigma_i \\ -\sigma_i & 0 \end{pmatrix}
\end{aligned}
\tag{8.46}
$$

Therefore,

$$
\sigma_{ij} = \begin{pmatrix} \epsilon_{ijk}\sigma_k & 0 \\ 0 & \epsilon_{ijk}\sigma_k \end{pmatrix}
\tag{8.47}
$$

$$
\begin{aligned}
q^2 &= (p - p')^2 \\
&= (\vec{p} - \vec{p}')^2 + (p_4 - p_4')^2 \\
&= \vec{p}'^{\,2} + p_4'^{2} - 2p_4' p_4 + p_4^2 \ \ (\text{for } \vec{p} = 0) \\
&= \vec{p}'^{\,2} + (iE_{p'})^2 - 2(iE_p')(iE_p) + (iE_p)^2 \\
&= \vec{p}'^{\,2} - E_{p'}^2 + 2E_p E_{p'} - E_P^2 \\
&= E_{p'}^2 - m^2 - E_{p'}^2 + 2E_{p'} m - m^2 \\
&= -m^2 + 2E_{p'} m - m^2
\end{aligned}
\tag{8.48}
$$

References

[1] S. Pacetti, R. Baldini Ferroli and E. Tomasi-Gustafsson, "Proton electromagnetic form factors: Basic notions, present achievements and future perspectives," Phys. Rept. **550-551**, 1 (2015).

[2] V. Punjabi, C. F. Perdrisat, M. K. Jones, E. J. Brash and C. E. Carlson, "The structure of the nucleon: Elastic electromagnetic form factors," Eur. Phys. J. A **51**, 79 (2015) [`arXiv:1503.01452 [nucl-ex]`].

[3] J. Gao *et al.* [Jefferson Lab Hall A Collaboration], "Dynamical relativistic effects in quasielastic 1p-shell knockout from ^{16}O," Phys. Rev. Lett. **84**, 3265 (2000).

[4] V. Punjabi *et al.*, "Proton elastic form factor ratios to $Q^2 = 3.5\,\mathrm{GeV}^2$ by polarization transfer," Phys. Rev. C **71**, 055202 (2005), Erratum: [Phys. Rev. C **71**, 069902 (2005)] [`arXiv:nucl-ex/0501018`].

[5] O. Gayou *et al.* [Jefferson Lab Hall A Collaboration], "Measurement of G_{Ep}/G_{Mp} in $\vec{e}p \to e\vec{p}$ to $Q^2 = 5.6\,\mathrm{GeV}^2$," Phys. Rev. Lett. **88**, 092301 (2002) [`arXiv:nucl-ex/0111010`].

[6] A. J. R. Puckett *et al.*, "Final analysis of proton form factor ratio data at $Q^2 = 4.0$, 4.8 and 5.6 GeV^2," Phys. Rev. C **85**, 045203 (2012) [`arXiv:1102.5737 [nucl-ex]`].

[7] T. Janssens, R. Hofstadter, E. B. Hughes and M. R. Yearian, "Proton form factors from elastic electron-proton scattering," Phys. Rev. **142**, 922 (1966).

[8] L. E. Price, J. R. Dunning, M. Goitein, K. Hanson, T. Kirk and R. Wilson, "Backward-angle electron-proton elastic scattering and proton electromagnetic form-factors," Phys. Rev. D **4**, 45 (1971).

[9] J. Litt *et al.*, "Measurement of the ratio of the proton form factors, G_E/G_M, at high momentum transfers and the question of scaling," Phys. Lett. B **31**, 40 (1970).

[10] C. Berger, V. Burkert, G. Knop, B. Langenbeck and K. Rith, "Electromagnetic form factors of the proton at squared four-momentum transfers between 10 and $50\,\mathrm{fm}^{-2}$," Phys. Lett. B **35**, 87 (1971).

[11] W. Bartel *et al.*, "Measurement of proton and neutron electromagnetic form factors at squared four-momentum transfers up to 3 (GeV/c)^2," Nucl. Phys. B **58**, 429 (1973).

[12] F. Borkowski, P. Peuser, G. G. Simon, V. H. Walther and R. D. Wendling, "Electromagnetic form factors of the proton at low four-momentum transfer (II)," Nucl. Phys. B **93**, 461 (1975).

[13] G. G. Simon, C. Schmitt, F. Borkowski and V. H. Walther, "Absolute electron-proton cross sections at low momentum transfer measured with a high pressure gas target system," Nucl. Phys. A **333**, 381 (1980).

[14] R. C. Walker *et al.*, "Measurements of the proton elastic form factors for $1 \leq Q^2 \leq 3$ (GeV/c)^2 at SLAC," Phys. Rev. D **49**, 5671 (1994).

[15] L. Andivahis *et al.*, "Measurements of the electric and magnetic form factors of the proton from $Q^2 = 1.75$ to 8.83 (GeV/c)^2," Phys. Rev. D **50**, 5491 (1994).

[16] M. E. Christy *et al.* [E94110 Collaboration], "Measurements of electron-proton elastic cross sections for $0.4 < Q^2 < 5.5$ (GeV/c)^2," Phys. Rev. C **70**, 015206 (2004) [`arXiv:nucl-ex/0401030`].

[17] I. A. Qattan *et al.*, "Precision Rosenbluth measurement of the proton elastic form factors," Phys. Rev. Lett. **94**, 142301 (2005) [`arXiv:nucl-ex/0410010`].

[18] L. N. Hand, D. G. Miller and R. Wilson, "Electric and magnetic form factor of the nucleon," Rev. Mod. Phys. **35**, 335 (1963).

[19] G. Bardin *et al.*, "Determination of the electric and magnetic form factors of the proton in the time-like region," Nucl. Phys. B **411**, 3 (1994).

[20] J. P. Lees *et al.* [BaBar Collaboration], "Study of $e^+e^- \rightarrow p\bar{p}$ via initial-state radiation at BABAR," Phys. Rev. D **87**, 092005 (2013) [`arXiv:1302.0055 [hep-ex]`].

[21] R. Pohl *et al.*, "The size of the proton, " Nature 466, 213 (2010).

[22] A. Antognini *et al.*, "Proton Structure from the Measurement of 2S-2P Transition Frequencies of Muonic Hydrogen", Science 339, 417 (2013).

[23] C. Patringnani *et al.* (Particle Data Group), "Review of Particle Physics," Chin. Phys. C, **40**, 100001 (2016).

[24] R. Pohl *et al.* [CREMA Collaboration], "Laser spectroscopy of muonic deuterium," Science **353**, 669 (2016).

[25] C. E. Carlson, "The Proton Radius Puzzle," Prog. Part. Nucl. Phys. **82**, 59 (2015) [`arXiv:1502.05314 [hep-ph]`].

[26] R. J. Hill, "Review of experimental and theoretical status of the proton radius puzzle," `arXiv:1702.01189 [hep-ph]`.

[27] G. Lee, J. R. Arrington and R. J. Hill, "Extraction of the proton radius from electron-proton scattering data," Phys. Rev. D **92**, no. 1, 013013 (2015) [`arXiv:1505.01489 [hep-ph]`].

[28] R. S. Sufian, Y. B. Yang, J. Liang, T. Draper and K. F. Liu, "Sea Quarks Contribution to the Nucleon Magnetic Moment and Charge Radius at the Physical Point," PRD 2017[`arXiv:1705.05849 [hep-lat]`].

[29] R. S. Sufian, Y. B. Yang, A. Alexandru, T. Draper, K. F. Liu and J. Liang, "Strange Quark Magnetic Moment of the Nucleon at Physical Point," Phys. Rev. Lett. **118**, no. 4, 042001 (2017) [`arXiv:1606.07075 [hep-ph]`].

[30] P. Hagler *et al.* [LHPC Collaboration], "Nucleon Generalized Parton Distributions from Full Lattice QCD," Phys. Rev. D **77**, 094502 (2008) [`arXiv:0705.4295 [hep-lat]`].

[31] Perkins, Donald H. (1982), Introduction to High Energy Physics, Addison Wesley, Reading, Massachusetts, ISBN 0-201-05757-3.

[32] K. F. Liu and S. J. Dong, "Origin of difference between $\bar{d}$ and $\bar{u}$ partons in the nucleon," Phys. Rev. Lett. **72**, 1790 (1994) [`arXiv:hep-ph/9306299`].

[33] K. F. Liu, W. C. Chang, H. Y. Cheng and J. C. Peng, "Connected-Sea Partons," Phys. Rev. Lett. **109**, 252002 (2012) [`arXiv:1206.4339 [hep-ph]`].

[34] S. J. Brodsky and B. Q. Ma, "Asymmetric quark / anti-quark hadronization in e+ e- annihilation," Phys. Lett. B **392**, 452 (1997) [`arXiv:hep-ph/9610304`].

[35] B. Q. Ma, "Strange magnetic moment and isospin symmetry breaking," Phys. Lett. B **408**, 387 (1997) [`arXiv:hep-ph/9707226`].

[36] D. S. Armstrong and R. D. McKeown, "Parity-Violating Electron Scattering and the Electric and Magnetic Strange Form Factors of the Nucleon," Ann. Rev. Nucl. Part. Sci. **62**, 337 (2012) [`arXiv:1207.5238 [nucl-ex]`].

[37] D. B. Kaplan and A. Manohar, "Strange Matrix Elements in the Proton from Neutral Current Experiments," Nucl. Phys. **B310** (1988) 527.

[38] R. McKeown, "Sensitivity of Polarized Elastic Electron Proton Scattering to the Anomalous Baryon Number Magnetic Moment," Phys. Lett. **B219** (1989) 140–142.

[39] D. H. Beck, "Strange Quark Vector Currents and Parity Violating Electron Scattering From the Nucleon and From Nuclei," Phys.Rev. **D39** (1989) 3248–3256.

[40] **SAMPLE** Collaboration, D. Spayde *et al.*, "The strange quark contribution to the proton's magnetic moment," Phys. Lett. **B583** (2004) 79–86, `arXiv:nucl-ex/0312016 [nucl-ex]`.

[41] E. Beise, M. Pitt, and D. Spayde, "The SAMPLE experiment and weak nucleon structure," Prog. Part. Nucl. Phys. **54** (2005) 289–350, `arXiv:nucl-ex/0412054 [nucl-ex]`.

[42] **HAPPEX** Collaboration, K. Aniol *et al.*, "Parity violating electroweak asymmetry in polarized $\vec{e}p$ scattering," Phys. Rev. **C69** (2004) 065501, `arXiv:nucl-ex/0402004 [nucl-ex]`.

[43] **A4** Collaboration, F. Maas *et al.*, "Measurement of strange quark contributions to the nucleon's form-factors at $Q^2 = 0.230\,(GeV/c)^2$," Phys. Rev. Lett. **93** (2004) 022002, `arXiv:nucl-ex/0401019 [nucl-ex]`.

[44] F. Maas, K. Aulenbacher, S. Baunack, L. Capozza, J. Diefenbach, *et al.*, "Evidence for strange quark contributions to the nucleon's form-factors at $Q^2 = 0.108\,(GeV/c)^2$," Phys. Rev. Lett. **94** (2005) 152001, `arXiv:nucl-ex/0412030 [nucl-ex]`.

[45] **HAPPEX** Collaboration, K. Aniol *et al.*, "Parity-violating electron scattering from He-4 and the strange electric form-factor of the nucleon," Phys. Rev. Lett. **96** (2006) 022003, `arXiv:nucl-ex/0506010 [nucl-ex]`.

[46] **HAPPEX** Collaboration, K. Aniol *et al.*, "Constraints on the nucleon strange form-factors at $Q^2 \sim 0.1\,GeV^2$," Phys. Lett. **B635** (2006) 275–279, `arXiv:nucl-ex/0506011 [nucl-ex]`.

[47] **G0** Collaboration, D. Armstrong *et al.*, "Strange quark contributions to parity-violating asymmetries in the forward G0 electron-proton scattering experiment," Phys. Rev. Lett. **95** (2005) 092001, `arXiv:nucl-ex/0506021 [nucl-ex]`.

[48] **HAPPEX** Collaboration, A. Acha *et al.*, "Precision Measurements of the Nucleon Strange Form Factors at $Q^2 \sim 0.1\,GeV^2$," Phys. Rev. Lett. **98** (2007) 032301, `arXiv:nucl-ex/0609002 [nucl-ex]`.

[49] **G0** Collaboration, D. Androic *et al.*, "Strange Quark Contributions to Parity-Violating Asymmetries in the Backward Angle G0 Electron Scattering Experiment," Phys. Rev. Lett. **104** (2010) 012001, `arXiv:0909.5107 [nucl-ex]`.

[50] S. Baunack, K. Aulenbacher, D. Balaguer Rios, L. Capozza, J. Diefenbach, *et al.*, "Measurement of Strange Quark Contributions to the Vector Form Factors of the Proton at $Q^2 = 0.22\,(GeV/c)^2$," Phys. Rev. Lett. **102** (2009) 151803, `arXiv:0903.2733 [nucl-ex]`.

[51] **HAPPEX** Collaboration, Z. Ahmed *et al.*, "New Precision Limit on the Strange Vector Form Factors of the Proton," Phys. Rev. Lett. **108** (2012) 102001, `arXiv:1107.0913 [nucl-ex]`.

[52] D. S. Armstrong, R. D. McKeown, "Parity-Violating Electron Scattering and the Electric and Magnetic Strange Form Factors of the Nucleon," Ann.Rev.Nucl.Part.Sci. **62** (2012) 337-359.

[53] Jianglai Liu, Robert D. McKeown, M. Musolf, "Global Analysis of Nucleon Strange Form Factors at Low Q^2," Phys.Rev. **C76** (2007) 025202.

[54] R. Gonzlez-Jimnez, J. Caballero, and T.W. Donnelly, "Global analysis of parity-violating asymmetry data for elastic electron scattering," Phys.Rev. **D90** (2014) 033002, `arXiv:1403.5119 [nucl-th]`.

[55] R. D. Young, J. Roche, R. D. Carlini, A. W. Thomas, "Extracting nucleon strange and anapole form factors from world data," Phys.Rev.Lett. **97** (2006) 102002.

[56] R.L. Jaffe, "Stranger than Fiction: The Strangeness Radius and Magnetic Moment of the Nucleon," Phys.Lett. **B229** (1989) 275.

[57] W. Koepf, E.M. Henley, "Electromagnetic gauge invariance of chiral hybrid quark models," Phys.Lett. **C49** (1994) 2219–2225.

[58] N.W. Park, J. Schechter, H. Weigel, "Electromagnetic, axial and strange currents in the Skyrme model: Effects of symmetry breaking," Phys.Rev. **D43** (1991) 869–884.

[59] M. Musolf and H. Ito, "Chiral symmetry and the nucleon's vector strangeness form-factors," Phys.Rev. **C55** (1997) 3066–3082.

[60] Douglas H. Beck, Barry R. Holstein, "Nucleon structure and parity violating electron scattering," Int.J.Mod.Phys. **E10** (2001) 1–41.

[61] B. Mueller *et al.* [SAMPLE Collaboration], "Measurement of the proton's neutral weak magnetic form-factor," Phys. Rev. Lett. **78**, 3824 (1997) [`arXiv:nucl-ex/9702004`].

[62] T. A. Forest, "A Measurement of the Proton Weak Magnetic Form Factor (G_M^Z) at $Q^2 = 0.1\,\mathrm{GeV}^2$," For SAMPLE Collaboration.

[63] M. J. Musolf, T. W. Donnelly, J. Dubach, S. J. Pollock, S. Kowalski and E. J. Beise, "Intermediate-energy semileptonic probes of the hadronic neutral current," Phys. Rept. **239** (1994) 1.

[64] W. J. Marciano and J. L. Rosner, "Atomic parity violation as a probe of new physics," Phys. Rev. Lett. **65**, 2963 (1990).

[65] J. Erler and M. J. Ramsey-Musolf, "The Weak mixing angle at low energies," Phys. Rev. D **72**, 073003 (2005) [`arXiv:hep-ph/0409169`].

[66] J. Liu, R. D. McKeown and M. J. Ramsey-Musolf, "Global Analysis of Nucleon Strange Form Factors at Low Q^2," Phys. Rev. C **76**, 025202 (2007) [`arXiv:0706.0226 [nucl-ex]`].

[67] Derek B. Leinweber, Anthony W. Thomas, "A Lattice QCD Analysis of the Strangeness Magnetic Moment of the Nucleon," Phys.Rev. **D62** (2000) 074505.

[68] D. B. Leinweber, S. Boinepalli, I. C. Cloet, A. W. Thomas, A. G. Williams, R. D. Young, J. M. Zanotti, J. B. Zhang, "Precise determination of the strangeness magnetic moment of the nucleon," Phys.Rev. Lett **94** (2005) 212001.

[69] Bastian Kubis, Randy Lewis, "Isospin violation in the vector form factors of the nucleon," Phys.Rev. **C74** (2006) 015204.

[70] P. Shanahan, R. Horsley, Y. Nakamura, D. Pleiter, P. Rakow, *et al.*, "Determination of the strange nucleon form factors," Phys.Rev.Lett. **114** (2015) 091802, `arXiv:1403.6537 [hep-lat]`.

[71] J. Green *et al.*, "High-precision calculation of the strange nucleon electromagnetic form factors," Phys.Rev. **D92** (2015) no.3, 031501.

[72] S. J. Dong, K. F. Liu, A. G. Williams, "Lattice calculation of the strangeness magnetic moment of the nucleon," Phys.Rev. **D58** (1998) 074504.

[73] T. Doi, M. Deka, S.-J. Dong, T. Draper, K.-F. Liu, *et al.*, "Nucleon strangeness form factors from $N_f = 2 + 1$ clover fermion lattice QCD," Phys.Rev. **D80** (2009) 094503, `arXiv:0903.3232 [hep-ph]`.

[74] J. Liang, Y. B. Yang, K. F. Liu, A. Alexandru, T. Draper and R. S. Sufian, "Lattice Calculation of Nucleon Isovector Axial Charge with Improved Currents," `arXiv:1612.04388 [hep-lat]`.

[75] Y. Aoki, *et al.* [RBC and UKQCD Collaborations],"Continuum Limit Physics from 2+1 Flavor Domain Wall QCD," Phys. Rev. D **D93**, (2011) 074508.

[76] T. Blum, *et al.* [RBC and UKQCD Collaborations], "Domain wall QCD with physical quark masses," Phys.Rev. **D93** (2016) 074505.

[77] A. Li *et al.* [xQCD Collaboration], "Overlap Valence on 2+1 Flavor Domain Wall Fermion Configurations with Deflation and Low-mode Substitution," Phys. Rev. D **82**, 114501 (2010) [`arXiv:1005.5424 [hep-lat]`].

[78] M. Gong *et al.* [χQCD Collaboration], "Strangeness and charmness content of the nucleon from overlap fermions on 2+1-flavor domain-wall fermion configurations," Phys. Rev. D **88**, 014503 (2013) [`arXiv:1304.1194 [hep-ph]`].
  [79]

[79] Y. B. Yang *et al.* [xQCD Collaboration], "πN and strangeness sigma terms at the physical point with chiral fermions," Phys. Rev. D **94**, no. 5, 054503 (2016) [`arXiv:1511.09089 [hep-lat]`].

[80] R. J. Hill and G. Paz, "Model independent extraction of the proton charge radius from electron scattering," Phys. Rev. D **82**, 113005 (2010) [`arXiv:1008.4619 [hep-ph]`].

[81] Z. Epstein, G. Paz and J. Roy, "Model independent extraction of the proton magnetic radius from electron scattering," Phys. Rev. D **90**, no. 7, 074027 (2014) [`arXiv:1407.5683 [hep-ph]`].

[82] Yi-Bo Yang, *et al.*, "Charm and strange quark masses and f_{D_s} from overlap fermions," Phys. Rev. D **D92**, (2015) 034517.

[83] Zhaofeng Liu, *et al.* [χQCD Collaboration], "Non-perturbative renormalization of overlap quark bilinears on 2+1-flavor domain wall fermion configurations," Phys. Rev. D **D90**, (2014) 034505.

[84] L. Maiani, G. Martinelli, M. L. Paciello and B. Taglienti, "Scalar Densities and Baryon Mass Differences in Lattice QCD With Wilson Fermions," Nucl. Phys. B **293**, 420 (1987).

[85] Yi-Bo Yang, Andrei Alexandru, Terrence Draper, Ming Gong, Keh-Fei Liu [χQCD Collaboration], "Stochastic method with low mode substitution for nucleon isovector matrix elements," Phys. Rev. D **D93**, (2016) 034503.

[86] T. R. Hemmert, U. G. Meissner and S. Steininger, "Strange magnetism in the nucleon," Phys. Lett. B **437**, 184 (1998) [`arXiv:hep-ph/9806226`].

[87] J.-W. Chen and M. J. Savage, "Baryons in partially quenched chiral perturbation theory," Phys.Rev. **D65** (2002) 094001, `arXiv:hep-lat/0111050 [hep-lat]`.

[88] T. R. Hemmert, U.-G. Meissner, and S. Steininger, "Strange magnetism in the nucleon," Phys.Lett. **B437** (1998) 184–190, `arXiv:hep-ph/9806226 [hep-ph]`.

[89] T. R. Hemmert, B. Kubis and U. G. Meissner, "Strange chiral nucleon form-factors," Phys. Rev. C **60**, 045501 (1999) [`arXiv: nucl-th/9904076`].

[90] S. R. Beane, "Nucleon masses and magnetic moments in a finite volume," Phys. Rev. D **70**, 034507 (2004) [`arXiv:hep-lat/0403015`].

[91] M. Lujan *et al.*, "The Δ_{mix} parameter in the overlap on domain-wall mixed action," Phys. Rev. D **86**, 014501 (2012), `arXiv:1204.6256 [hep-lat]`.

[92] J. M. M. Hall, D. B. Leinweber, B. J. Owen, R. D. Young, "Finite-volume corrections to charge radii," Phys. Rev.**B725**, (2013) 101-105.

[93] B. C. Tiburzi, "Finite Volume Effects on the Extraction of Form Factors at Zero Momentum," Phys. Rev. D **90**, no. 5, 054508 (2014) [`arXiv:1407.4059 [hep-lat]`].

[94] A. Abdel-Rehim, C. Alexandrou, M. Constantinou, V. Drach, K. Hadjiyiannakou, K. Jansen, G. Koutsou and A. Vaquero, "Disconnected quark loop contributions to nucleon observables in lattice QCD," Phys. Rev. D **89**, no. 3, 034501 (2014) [`arXiv:1310.6339 [hep-lat]`].

[95] J. Green *et al.*, "High-precision calculation of the strange nucleon electromagnetic form factors," Phys. Rev. D **92**, no. 3, 031501 (2015) [arXiv:1505.01803 [hep-lat]].

[96] S. Capitani *et al.*, "Nucleon electromagnetic form factors in two-flavor QCD," Phys. Rev. D **92**, no. 5, 054511 (2015) [arXiv:1504.04628 [hep-lat]].

[97] H. W. Lin, S. D. Cohen, R. G. Edwards, K. Orginos and D. G. Richards, "Lattice Calculations of Nucleon Electromagnetic Form Factors at Large Momentum Transfer," arXiv:1005.0799 [hep-lat].

[98] C. Alexandrou *et al.*, "Nucleon electromagnetic form factors in twisted mass lattice QCD," Phys. Rev. D **83**, 094502 (2011) [arXiv:1102.2208 [hep-lat]].

[99] C. Alexandrou *et al.* [ETM Collaboration], "Position space method for the nucleon magnetic moment in lattice QCD," Phys. Rev. D **94**, no. 7, 074508 (2016) [arXiv:1605.07327 [hep-lat]].

[100] T. Bhattacharya, S. D. Cohen, R. Gupta, A. Joseph, H. W. Lin and B. Yoon, "Nucleon Charges and Electromagnetic Form Factors from 2+1+1-Flavor Lattice QCD," Phys. Rev. D **89**, no. 9, 094502 (2014) [arXiv:1306.5435 [hep-lat]].

[101] T. Yamazaki, Y. Aoki, T. Blum, H. W. Lin, S. Ohta, S. Sasaki, R. Tweedie and J. Zanotti, "Nucleon form factors with 2+1 flavor dynamical domain-wall fermions," Phys. Rev. D **79**, 114505 (2009) [arXiv:0904.2039 [hep-lat]].

[102] S. N. Syritsyn *et al.*, "Nucleon Electromagnetic Form Factors from Lattice QCD using 2+1 Flavor Domain Wall Fermions on Fine Lattices and Chiral Perturbation Theory," Phys. Rev. D **81**, 034507 (2010) [arXiv:0907.4194 [hep-lat]].

[103] D. Djukanovic, T. Harris, G. von Hippel, P. Junnarkar, H. B. Meyer and H. Wittig, "Nucleon electromagnetic form factors and axial charge from CLS $N_\mathrm{f} = 2 + 1$ ensembles," PoS LATTICE **2015**, 137 (2016) [arXiv:1511.07481 [hep-lat]].

[104] A. Abdel-Rehim, C. Alexandrou, M. Constantinou, K. Hadjiyiannakou, K. Jansen and G. Koutsou, "Nucleon electromagnetic form factors from twisted mass lattice QCD," PoS LATTICE **2014**, 148 (2015) [arXiv:1501.01480 [hep-lat]].

[105] C. Alexandrou, M. Constantinou, K. Hadjiyiannakou, K. Jansen, C. Kallidonis, G. Koutsou, K. Ottnad and A. Vaquero, "Nucleon electromagnetic and axial form factors with N_f=2 twisted mass fermions at the physical point," arXiv:1702.00984 [hep-lat].

[106] J. R. Green, J. W. Negele, A. V. Pochinsky, S. N. Syritsyn, M. Engelhardt and S. Krieg, "Nucleon electromagnetic form factors from lattice QCD using a nearly physical pion mass," Phys. Rev. D **90**, 074507 (2014) [`arXiv:1404.4029 [hep-lat]`].

[107] S. Syritsyn, "Nucleon Structure on a Lattice at the Physical Point," J. Phys. Conf. Ser. **640**, no. 1, 012054 (2015).

[108] A. Tang, W. Wilcox and R. Lewis, "Lattice results on the connected neutron charge radius," Phys. Rev. D **68**, 094503 (2003) [`arXiv: hep-lat/0307006`].

[109] C. Alexandrou, "Novel applications of Lattice QCD: Parton distribution functions, proton charge radius and neutron electric dipole moment," EPJ Web of Conferences **137**, 01004 (2017) `arXiv:1612.04644 [hep-lat]`.

[110] R. S. Sufian, "Neutral Weak Form Factors of Proton and Neutron," `arXiv:1611.07031 [hep-ph]`.

[111] John Towns, Timothy Cockerill, Maytal Dahan, Ian Foster, Kelly Gaither, Andrew Grimshaw, Victor Hazlewood, Scott Lathrop, Dave Lifka, Gregory D. Peterson, Ralph Roskies, J. Ray Scott, Nancy Wilkins-Diehr, "XSEDE: Accelerating Scientific Discovery", Computing in Science & Engineering, vol.16, no. 5, pp. 62-74, Sept.-Oct. 2014, doi:10.1109/MCSE.2014.80.

Curriculum Vitae

<div align="center">

Raza Sabbir Sufian

</div>

EDUCATION

University of Kentucky, Lexington, Kentucky
Thesis advisor: Professor Keh-Fei Liu
Research Focus: Nucleon Electromagnetic Form Factors From Lattice QCD
M.S. in Physics (2014)

University of Dhaka, Dhaka, Bangladesh
B.S. in Physics (Minor in Mathematics) (2010)

PROFESSIONAL EXPERIENCE

- **Graduate Research Assistant,** University of Kentucky (2012 – 2017)

PUBLICATIONS

1. "Neutral Weak Form Factors of Proton and Neutron," (**Under review for Phys. Rev. D publication**) **Raza Sabbir Sufian**, `arXiv:1611.07031 [hep-ph]`.

2. "Strange Quark Magnetic Moment of the Nucleon at Physical Point," **Raza Sabbir Sufian**, Y. B. Yang, A. Alexandru, T. Draper, K. F. Liu and J. Liang, Phys. Rev. Lett. **118**, no. 4, 042001 (2017) [`arXiv:1606.07075 [hep-ph]`].

3. "Sea Quarks Contribution to the Nucleon Magnetic Moment and Charge Radius at the Physical Point," **Raza Sabbir Sufian**, Y. B. Yang, J. Liang, T. Draper, and K. F. Liu, (**Phys. Rev. D 2017**) [`arXiv:1705.05849 [hep-lat]`].

4. "Glue spin and helicity in proton from lattice QCD," Y. B. Yang, **Raza Sabbir Sufian**, A. Alexandru, T. Draper, M. J. Glatzmaier, K. F. Liu and Y. Zhao, Phys. Rev. Lett. **118**, no. 10, 102001 (2017) [`arXiv:1609.05937 [hep-ph]`].

5. "Analysis of Nucleon Electromagnetic Form Factors from Light-Front Holographic QCD : The Space-Like Region,"**Raza Sabbir Sufian**, G. F. de Téramond, S. J. Brodsky, A. Deur and H. G. Dosch, Phys. Rev. D **95**, no. 1, 014011 (2017) `arXiv:1609.06688 [hep-ph]`.

6. J. Liang, Y. B. Yang, K. F. Liu, A. Alexandru, T. Draper and **R. S. Sufian**, "Lattice Calculation of Nucleon Isovector Axial Charge with Improved Currents," (**Accepted for Phys. Rev. D publication**) `arXiv:1612.04388 [hep-lat]`.

7. "Superconformal Algebraic Approach to Hadron Structure," G. F. de Téramond, S. J. Brodsky, A. Deur, H. G. Dosch and **Raza Sabbir Sufian**, EPJ Web Conf. **137**, 03023 (2017) [`arXiv:1611.03763 [hep-ph]`].

8. "Glue Spin of the Proton," Y. B. Yang, **Raza Sabbir Sufian**, *et al.* [χQCD Collaboration], Published in PoS LATTICE **2015**, 129 (2016), [`arXiv:1603.05256 [hep-ph]`].

9. "Unphysical Poles of Domain Wall Fermions at finite L_s," **Raza Sabbir Sufian**, M. J. Glatzmaier and Y. B. Yang, `arXiv:1603.01591 [hep-lat]`.

10. "Glue Spin S_G in The Longitudinally Polarized Nucleon," **Raza Sabbir Sufian**, *et al.* [χQCD Collaboration], Published in PoS LATTICE **2014**, 166 (2015), [`arXiv:1412.7168 [hep-lat]`].

11. "The Roper Puzzle," K. F. Liu, Y. Chen, M. Gong, **Raza Sabbir Sufian**, M. Sun and A. Li [χQCD Collaboration], Published in PoS LATTICE **2013**, 507 (2014), [`arXiv:1403.6847 [hep-ph]`].